Using Wavelet Analysis to Study AGN X-ray Variability

by

Akshay Ghosh

A Thesis Submitted to Saint Mary's University, Halifax, Nova Scotia in Partial Fulfillment
of the Requirements for the Degree of MSc in Astronomy
(Department of Astronomy and Physics)

2023, Halifax, Nova Scotia

Approved: _____

Dr. Luigi Gallo

Approved: _____

Dr. Robert Thacker

Approved: _____

Dr. Philip Bennett

Date: August 1st 2023

Acknowledgements

Firstly I would like to thank my Mom and Dad for all of their support and encouragement throughout my life. I would like to thank my supervisor Dr. Luigi Gallo for believing in me and giving me the opportunity to pursue science further, and providing direction, guidance, and patience during my research. I would like to thank Dr. Adam Gonzalez for providing help with so many specific details during my research. I would like to thank Margaret for assisting me with details in the science, especially helping me to prepare for my defence, and being the first friend that I met in Halifax. And finally, I would like to thank my Halifax family of George, Meghan, Gurmukh, Pargat, and Stella for all of the amazing times that we had here.

Contents

List of Figures

Abstract

Using Wavelet Analysis to Study AGN X-ray Variability

by Akshay Ghosh

In this work, we examine the application of the wavelet transform to the X-ray timing analyses of active galactic nuclei (AGN) and quasi-periodic eruption sources (QPEs). We find that the power spectral density (PSD) slope and the nature of the periodic signal can influence the ability to identify important features in the wavelet power spectrum. Several scenarios are simulated to test the effectiveness of the wavelet analysis to stationary and non-stationary data. We carried out a wavelet analysis to five unique objects: Ark 120, IRAS 13224-3809, RE J1034+396, the QPE GSN 069, and the eclipsing NGC 6814. The well-known quasi-periodic oscillation (QPO) in RE J1034+396 is significantly detected in the wavelet power spectrum. In IRAS 13224-3809, significant transient features appear during a flare at frequencies coincident with previously detected reverberation signals. The wavelet power spectrum of the QPE GSN 069 significantly reveals four persistent signals.

August 1, 2023

Chapter 1

Introduction

1.1 What Is An Active Galaxy?

Active Galactic Nuclei (most commonly referred to as AGNs) are some of the most luminous objects in space. A typical AGN is many orders of magnitude more luminous than our own Sun, by a factor of approximately 10^{10}, and they can outshine all the stars in their host galaxy. Fortunately for us, our own galaxy The Milky Way is not an active galaxy, but rather a "dormant" or normal galaxy.

Starting in the 1900's, there were observations of galaxies exhibiting what were later determined to be AGN like characteristics. For example, emission lines were seen in NGC 1068 and Messier 81 (Fath 1909). In 1943, Carl Seyfert published a study on the observations of nearby galaxies with unexpected broad emission lines (Seyfert 1943). These galaxies, which were later deemed to be "active galaxies" were also later named "Seyfert galaxies", in reference to Carl Seyfert's work that set the building blocks for the field of AGN astronomy.

1.1.1 Structure of an AGN

An AGN consists of two main components. These are a supermassive black hole (SMBH) at its center and an accretion disk of matter surrounding the SMBH. The accretion disk is the main source of the radiation emitted from the AGN region. In some cases, emerging from the central region is a relativistic jet, normal to the plane of the accretion disk. The nature of of the launching mechanisms of these jets are still largely unknown. Surrounding much of the accretion disk and sometimes obscuring our view of the central engine is the optically thick torus. The AGN unification model (e.g. Urry 1995) in Figure 1.1 states that different AGN manifestations can be attributed to our viewing angle relative to the torus.

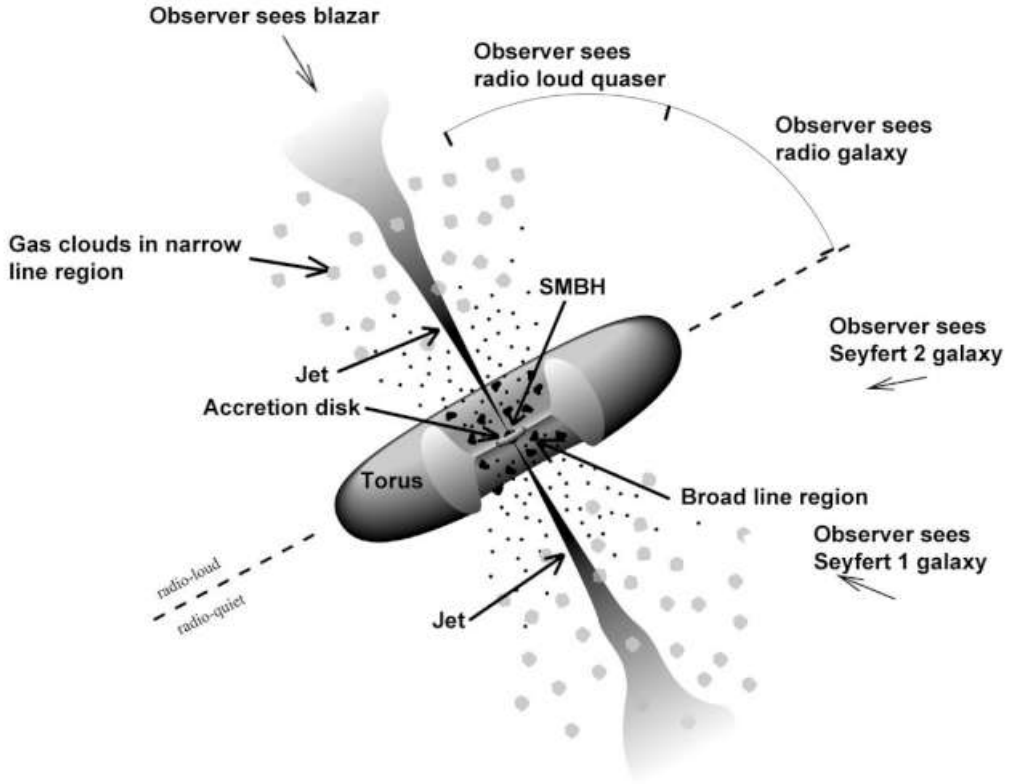

Figure 1.1: Illustration of an AGN and its components. The AGN classification based on viewing angle is also shown. (Fermi Gamma-Ray Space Telescope 2016)

While some of the different observed characteristics of AGNs can be attributed to the external viewing angle, there are also some differences that are intrinsic to the different AGNs

themselves. For example, not all AGNs produce jets and we distinguish these groups as radio-quiet (non-jetted) and radio-loud (jetted).

Different types of radio-quiet AGNs include Seyfert galaxies as mentioned earlier, low-ionization nuclear emission-line regions (LINERs), and radio-quiet quasars. Seyfert galaxies, the first discovered AGNs, are split into Seyfert 1 and 2, depending on the level of obscuration by the torus. Shown in Figure 1.1, we have a direct line of sight to the central region of Seyfert 1. Seyfert 1s tend to emit strongly in the soft X-ray band. Seyfert 1s typically show broad emission lines in the optical band, unlike Seyfert 2 which do not show these broad emission lines. A comparison of a Seyfert 1 and Seyfert 2 optical spectra is shown in Figure 1.2.

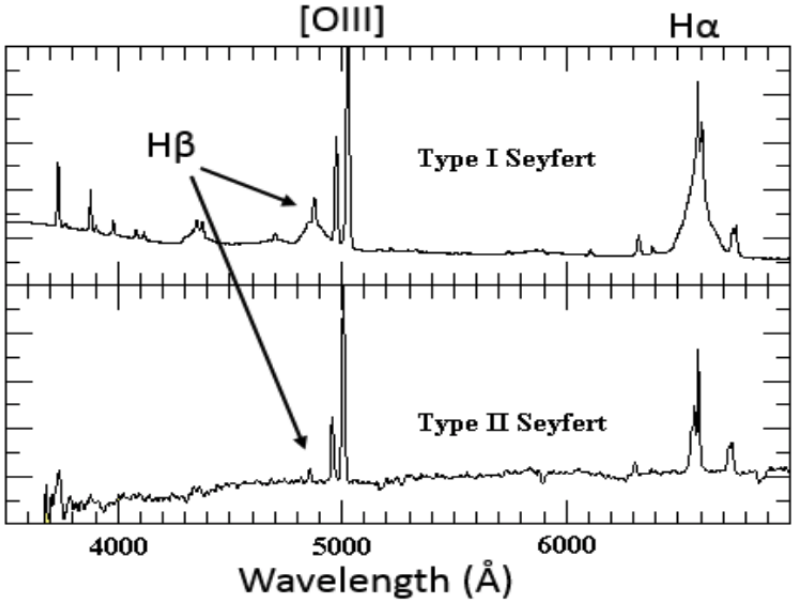

Figure 1.2: Comparison of the optical spectrum of a Seyfert 1 and Seyfert 2 galaxy. (Morgan 2002)

Figure 1.2 shows that broad $H\alpha$ and $H\beta$ emission lines are observed only in Seyfert 1s. Strong narrow $[OIII]$ emission lines are observed in both Seyfert 1 and 2, but they are relatively stronger in Seyfert 2. These differences in the observed spectra can be described by the unification model of radio-quiet galaxies (Urry 1995). Seyfert 1 and 2 galaxies may be similar objects, viewed from a different angle. Seyfert 1 galaxies allowing for a direct view of the

galaxy nucleus, while Seyfert 2 galaxies are viewed through the dusty torus. The viewing angle can explain these differences in observed spectra.

Examples of radio-loud AGN include blazars and radio-loud quasars. Blazars are viewed directly down the jet (Fig 1.1) and emit extremely variable light across all energy bands. Quasars are the same object as blazars, but are viewed with the jet pointing away from the observer. Radio-loud quasars show the same characteristics as radio-quiet quasars, with the addition of jet emission.

1.1.2 Accretion

A process that is integral to the study of black holes and AGNs is the accretion of mass, which is the major energy source. Compact objects which undergo accretion are a powerful source of energy. A complete description of this accretion process is outlined in Kolb (2010).

Mass accretion is one of the most important processes in astrophysics. This occurs when a body with a strong gravitational field accumulates matter from some external reservoir, and thus increases in mass. Accretion releases gravitational potential energy, which can result in these accreting objects being extremely powerful sources of energy and radiation.

For a spherically symmetric object with mass M and radius R, the gravitational potential energy for a smaller object (sometimes known as a "test mass" m), at a distance R is:

$$E_g(R) = -\frac{GMm}{R} \tag{1.1}$$

As the test mass moves from very far away ($r \approx \infty$), to the surface of the gravitating body

($r = R$), the change in gravitational potential energy is:

$$\begin{aligned}\Delta E_g &= E_g(r \approx \infty) - E_g(r = R) \\ &= 0 - \left(- \frac{GMm}{R} \right) \\ &= \frac{GMm}{R}\end{aligned}$$

$$\Delta E_g(R) = \frac{GMm}{R} \tag{1.2}$$

Consider a gravitating body, known as the accretor, accreting mass at the rate $\dot{M}$. For a time range Δt, it will accrete an amount of mass $\Delta M = \dot{M}\Delta t$. Then from equation 1.2, an amount of mass $m = \Delta M$ will be accreted, and the following amount of energy is released:

$$\Delta E_g(R) = \frac{GM\Delta M}{R} = \Delta E_{acc} \tag{1.3}$$

If all of the accretion energy ΔE_{acc} is radiated at the same rate at which it is liberated, the luminosity due to accretion is:

$$L_{acc} = \frac{\Delta E_{acc}}{\Delta t}, \tag{1.4}$$

and hence,

$$L_{acc} = \frac{GM\dot{M}}{R} \tag{1.5}$$

This is called the accretion luminosity.

It is useful to estimate the mass accretion rate needed for significant accretion luminosity for a typical star such as the Sun, and to compare it with mass flow rates in the universe. Mass accretion rate is usually expressed in solar masses ($M_\odot$) per year, which amounts to 6.31×10^{22} kg s^{-1}. The mass accretion rate required for the solar luminosity is approximately $3.2 \times 10^{-8} M_\odot$ yr^{-1}. To achieve this luminosity, for an AGN system that is the radius of our solar system, approximately 100 solar masses of matter would need to be accreted in one year. For a fixed mass accretion rate, the luminosity increases proportional to the compactness M/R of the gravitating body.

1.1.3 The Accretion Disk

Accreting matter rarely falls into the accretor in a straight trajectory. The conservation of angular momentum will usually cause the accretion disk to form into a flat plane-like structure, normal to the net angular momentum of the accretion material. As "blobs" of plasma[1] orbit the accretor, they slowly drift towards the center, losing angular momentum and therefore gravitational potential energy. Accretion disks are like engines which extract the gravitational potential energy and angular momentum from plasma. There is a full description of these optically thick, geometrically thin, accretion disks in Shakura & Sunyaev (1973).

In the simple case where plasma is at a radial distance r from a spherically symmetric accretor of mass M[2], the plasma will be orbiting the gravitating body in a Keplerian orbit with a speed of:

$$v_K = \left(\frac{GM}{r}\right)^{1/2} \tag{1.6}$$

The orbit of some blob of plasma in the accretion disk is a Kepler orbit, but with a non-constant

[1] Plasma is a conducting fluid such as ionized gas. Its properties are determined by its composition of ions and electrons. Stellar matter is usually fully ionized, unless it is at a cool temperature.

[2] It is assumed that the plasma is first at $r = \infty$.

radius. As the blob drifts towards the gravitating body, the radius of the Kepler orbit slowly decreases. This results in the blob losing gravitational potential energy and gaining kinetic energy. Since the kinetic energy is: $E_K = \frac{1}{2}mv_K^2$,

$$E_K = \frac{1}{2}\frac{GMm}{r} \tag{1.7}$$

The gravitational potential energy is:

$$E_g = -2E_K \tag{1.8}$$

$$E_g = -\frac{GMm}{r} \tag{1.9}$$

And the total energy, is $E_K + E_g + E_R = 0$:

$$E_{tot} = E_K + E_g + E_R \tag{1.10}$$

$$E_{tot} = \frac{1}{2}E_g + E_R \tag{1.11}$$

$$E_R = -\frac{1}{2}E_g = 0 \tag{1.12}$$

$$E_{tot} = 0 \tag{1.13}$$

From these results we can see that for the plasma, one half of the gravitational potential energy is converted into kinetic energy, while the other half of the energy that heats the plasma and fuels the radiation emission over the entire electromagnetic spectrum has to have been dissipated in E_R, though local heating of the gas in the accretion disk which increases the local gas temperature until the radiative losses are balanced with the dissipative heating.

When quantifying the luminosity due to accretion, at most only half of the energy from the

gravitating body (Eq 1.2) is available for radiation and therefore the luminosity can be expressed as:

$$L_{disc} = \frac{1}{2}\frac{GM\dot{M}}{R} \tag{1.14}$$

From this result, it is evident that the accretion disk luminosity is proportional to two quantities; the mass accretion rate $\dot{M}$, and the compactness M/R. Converting gravitational energy into radiation can be highly efficient - almost 20 - 30 times greater than in nuclear fusion. Combining this more efficient conversion of energy, with the fact that accretion timescales are much shorter than nuclear fusion timescales of main sequence stars, results in AGN being orders of magnitude more luminous than all the stars in a galaxy.

1.1.4 Emission of Light

The processes by which the radiation is emitted are generated by the gravitational effects of the SMBH on the accretion disk, which is sometimes referred to as "the central engine". The intense gravity of the SMBH is what drives this emission. As matter is swirling around near the center, its trajectories are dominated by the gravitational field of the SMBH. The conservation of angular momentum causes the matter which would have originated from random directions, to form a flat accretion disk. Due to the gravitational force, the material closer to the SMBH has a much higher velocity than the material that is further out. This difference in velocity generates friction between neighboring regions of the accretion disk, causing nearer material to transfer angular momentum to the further material. This transfer of angular momentum outwards allows more matter to fall towards the SMBH.

The emission of light from AGNs differs from that of non-active galaxies. The total emission from non-active, or "normal" galaxies is the combination of the radiative flux of all its con-

stituent stars, with each star radiating approximately as a blackbody with the peak somewhere around the visible or infrared frequency bands. However, in AGNs the emitted flux spectrum is dominated by non-stellar processes (Oke & Sargent 1968), and they emit strongly over the entire electromagnetic spectrum from extremely long radio waves, to extremely high frequency gamma waves. Therefore AGN emission does not follow a blackbody spectrum. The peak of AGN emission is typically in the UV band where the thermal disk emission peaks. However, much of this UV light does not make it to our space telescopes that are orbiting Earth, due to the absorption by the interstellar medium in our Galaxy. An example of the broadband spectral energy distributions (SEDs) for radio-loud and radio-quiet AGNs is shown in Fig 1.3.

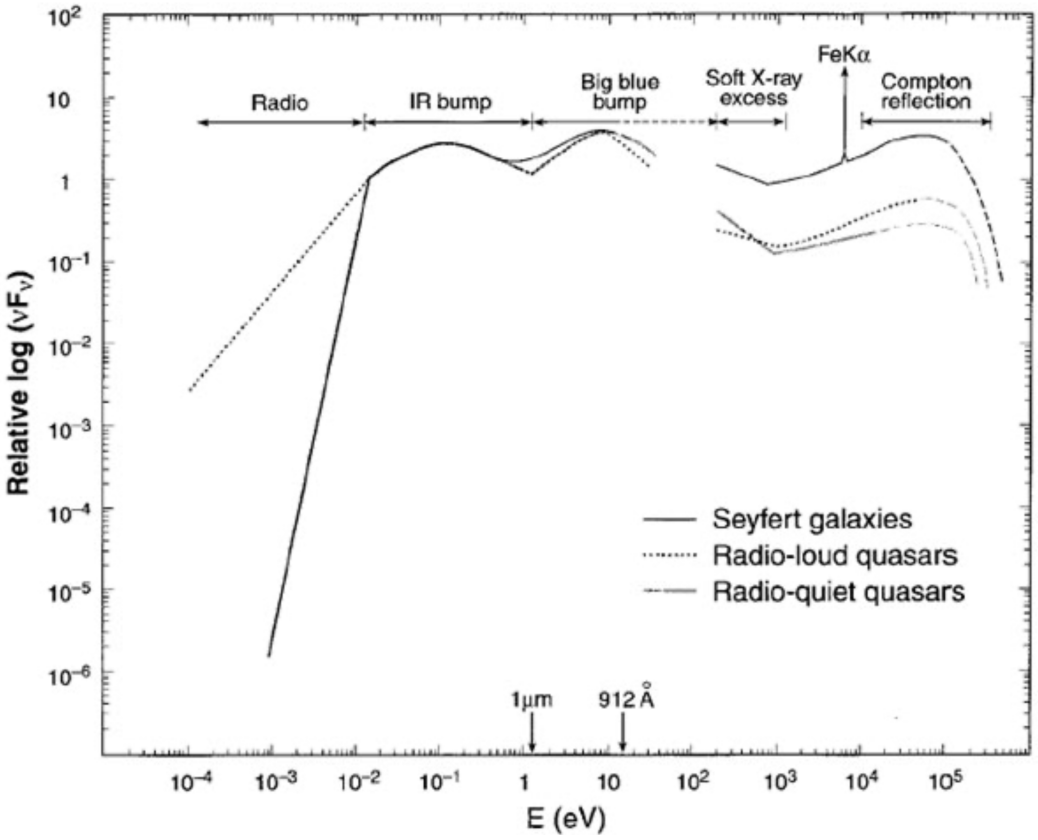

Figure 1.3: Radio to X-ray SED for various AGN types. (Koratkar & Blaes 1999)

As stated, the UV peak (big blue bump) is attributed to the thermal pressure in the accretion disk. The IR bump arises from dusty torus emission. The radio emission originated from the jets seen in some objects. The X-ray emission originates on small physical scales closest to the

black hole, of approximately $\sim 10\ r_g$, where r_g is known as the gravitational radii and is defined as $r_g = \frac{GM}{c^2}$ [3].

1.1.5 The X-ray Emitting Region

Even though the accretion disk may be the most prominent component of an AGN, the high energy X-rays are not directly emitted from the accretion disk. One reason is that the temperature of the disk is too low compared to the energy of the X-ray emission. The region is also much more compact than the disk. The variability seen in X-rays of an isotropic emitter is limited by the light travel time across the region. Since AGN X-ray emission can vary on timescales down to hours, this suggests the the X-ray emitting region is quite compact. For an AGN with a central black hole of $\sim 10^7 M_\odot$, the X-ray emitting region will have a radius less than 100 gravitational radii r_g.

The general process behind AGN X-ray emission, are described in Gallo (2011) (Fig 1.4). Ultraviolet (UV) photons are emitted from the accretion disc. A portion of these UV photons interact with the corona, which is essentially a cloud of hot electrons with $T > 10^8$ K surrounding the inner accretion disc in some configuration. In the corona, the UV photons undergo a process called inverse Compton scattering (or Comptonization), where through photon-electron collisions, energy is on average transferred from the higher energy electrons to the lower energy photons. This "bumps up" the photons from UV to X-ray energy (factor of 10 for soft X-rays, factor of 100 for hard X-rays). Comptonization is revealed in the energy spectrum by its power-law shape. The temperature and density in the corona determine the slope of the power

[3] Gravitational radii can also be expressed as:

$$r_g = \frac{r_s}{2}$$

Where r_s is the Schwarzchild radius. Note, the event horizon of a Schwarzschild black hole (non-rotating), is $2r_g = r_s$. For $M = 10^7 M_\odot$, we have $r_g \approx 10^{-7}$ pc. For comparison, the distance between the Sun and Neptune, i.e. the radius of our Solar System, is about 1.5×10^{-4} pc. As the X-ray emitting region is unresolved, our understanding relies on timing and spectral observations of AGNs.

law.

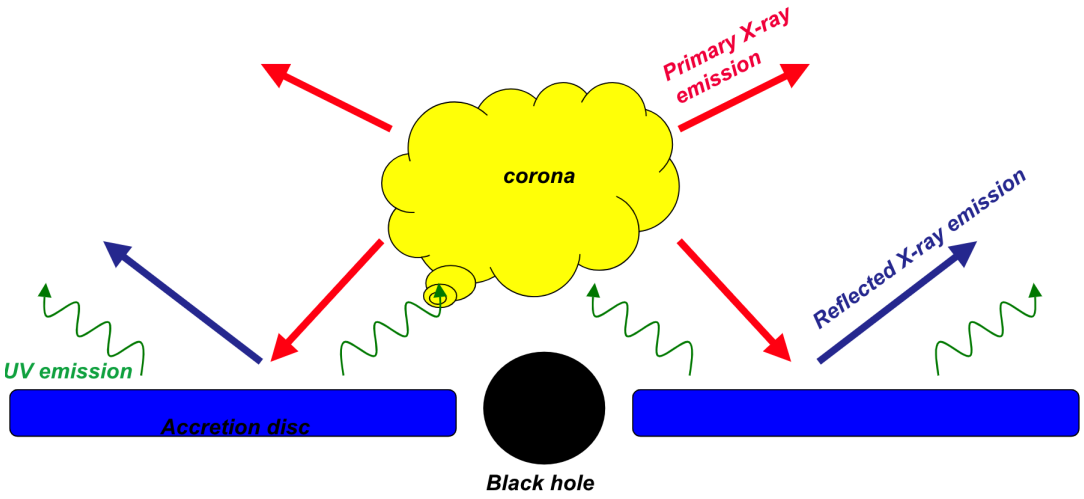

Figure 1.4: Illustration of the geometry and emission processes in the compact X-ray inner region (Gallo 2011).

Due to the maximum energy of the Comptonized photons being limited by the maximum energy of the electrons in the corona, there will be a high-energy cutoff in the power-law spectrum. If measured, this cutoff gives the corona temperature.

As the corona emits isotropically, some of the power law emission will illuminate the accretion disc. This emission is reprocessed and blurred from the relativistic effects close to the black hole in the accretion disc. The strongest signatures of this reflected emission are the soft-excess, Compton hump, and the FeKα emission seen in Fig 1.3.

1.2 X-ray Space Telescopes

XMM-Newton is one of the most prominent space[4] telescopes used in X-ray astronomy. *XMM-Newton* was launched on December 10th, 1999, from the Guiana Space Centre in French Guiana, located on the east coast of South America, and travels in a highly elliptical orbit around Earth (Fig 1.5). By May 2018, there had been approximately 5600 scientific papers published either about data collected by *XMM Newton*, or on the telescope itself (Kretschmar 2018). That is, on average, a paper being published approximately every 29 hours.

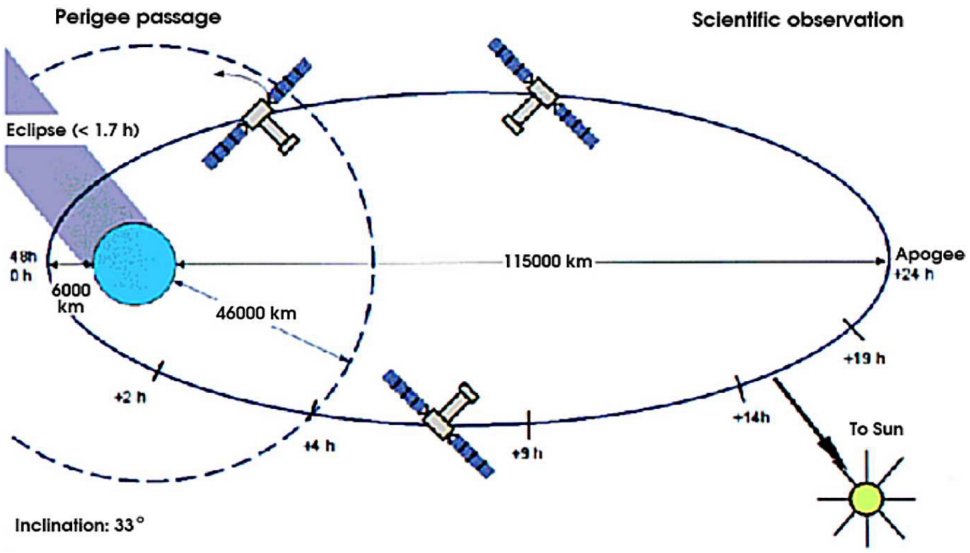

Figure 1.5: The orbit of *XMM-Newton* is highly elliptical to allow for longer consecutive observations of target objects(ESA Handbook).

Detailed information on the all aspects of the *XMM-Newton* science instruments can be found at in the ESA Handbook[5].

1.2.1 XMM-Newton overview

XMM-Newton consists of three X-ray telescopes and an imaging unit called the European Photon Imaging Camera (EPIC). EPIC consists of three CCD (Charged Coupled Device) cameras,

[4]Due to the strong absorption of X-rays by the Earth's atmosphere, all X-ray telescopes must operate from space.

[5]The *XMM-Newton* User's Handbook is available at `https://xmm-tools.cosmos.esa.int/external/xmm_user_support/documentation/uhb/`.

that are all capable of creating X-ray images, spectroscopy, and X-ray lightcurves. Two of the detectors are MOS CCDs, and the other is a pn CCD. The payload is shown in Figure 1.6.

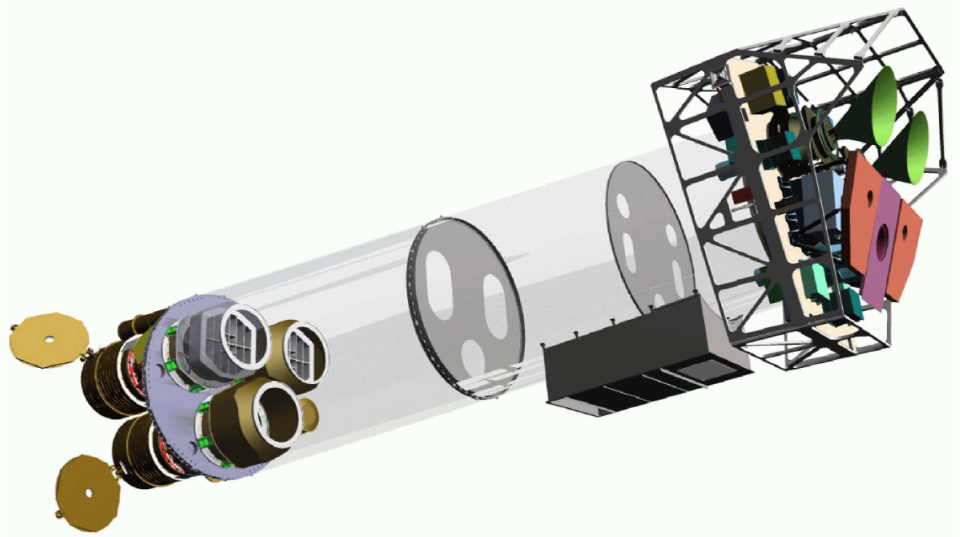

Figure 1.6: Schematic of the *XMM-Newton* payload. On the right side, are the X-ray instruments. The EPIC MOS cameras are the green horns, and the EPIC pn camera is the centered violet component (ESA Handbook).

While the focus of this work is on the two different EPIC cameras, MOS and pn, there are also the Reflection Grating Spectrometer (RGS) and the Optical Monitor (OM). The three EPIC cameras and two RGS spectrometers are in the focal planes of the X-ray telescopes, and the OM has its own telescope. There are a total of six science instruments on *XMM-Newton*, which collect data simultaneously. Each instrument can operate independently as they can be turned on/off at separate times. One scenario where it is useful to turn on/off different instruments at different times is if the source target is so bright that it could damage one of the instruments.

The key characteristics of *XMM-Newton* are as follows: *(i) High sensitivity*. The *XMM Newton* telescopes have the largest effective area of any focusing X-ray telescope, with a total geometric effective area at 1.5 keV of 1550 cm^2 per telescope, for a total area of 4650 cm^2. *(ii) Good angular resolution*. Each X-ray telescope consists of 58 nested mirror shells. The resulting Point Spread Function (PSF) FWHM is approximately 6". *(iii) Moderate spectral resolution*. The EPIC CCD cameras have a resolving power $E/\Delta E$ of approximately 20-50.

(iv) Long continuous visibility of the target. The *XMM-Newton* orbit is highly elliptical and can achieve continuous visibility of up to approximately 40 hours. The minimum altitude for observations is 46,000 km, which is very useful for variability studies (Fig 1.5).

1.2.2 How X-ray telescopes observe light

A brief overview of how X-ray telescopes observe light is as following. X-ray photons are emitted from a distant object. These photons travel through space, being stretched by the expansion of space (redshifted), and a fraction being obscured by gas and dust in the source galaxy, Milky Way, and the intergalactic medium. These X-ray photons then arrive in our Solar System near Earth.

A small fraction of these X-rays then enter a space telescope such as *XMM Newton*. They graze the telescope mirrors at a very small angle. There are two mirrors placed consecutively to each other: a parabolic mirror followed by a hyperbolic mirror (Fig 1.7).

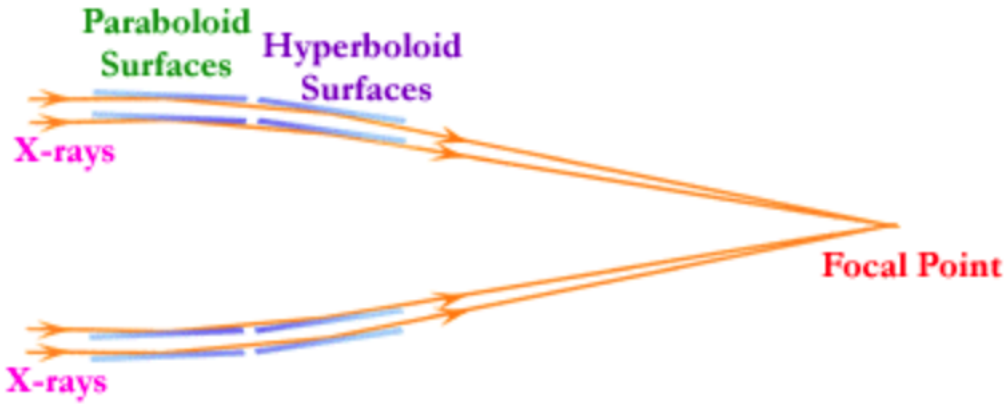

Figure 1.7: Schematic of the mirror setup for an X-ray telescope: A parabolic mirror, followed by a hyperbolic mirror, reflecting the light to the focus (NASA 2019).

Figure 1.8 highlights a key difference between X-ray and optical telescopes. A conventional optical telescope has its mirror perpendicular to the path of the light rays, which are then reflected back towards a focus. However, this design would be extremely ineffective for X-rays. Due to their high energy, the X-rays would pass right through the mirror. To get around this issue, for

X-ray telescopes the mirrors are oriented almost parallel to the light rays, at a very small angle, called the grazing incidence angle. This small angle allows the X-rays to be redirected towards the focus.

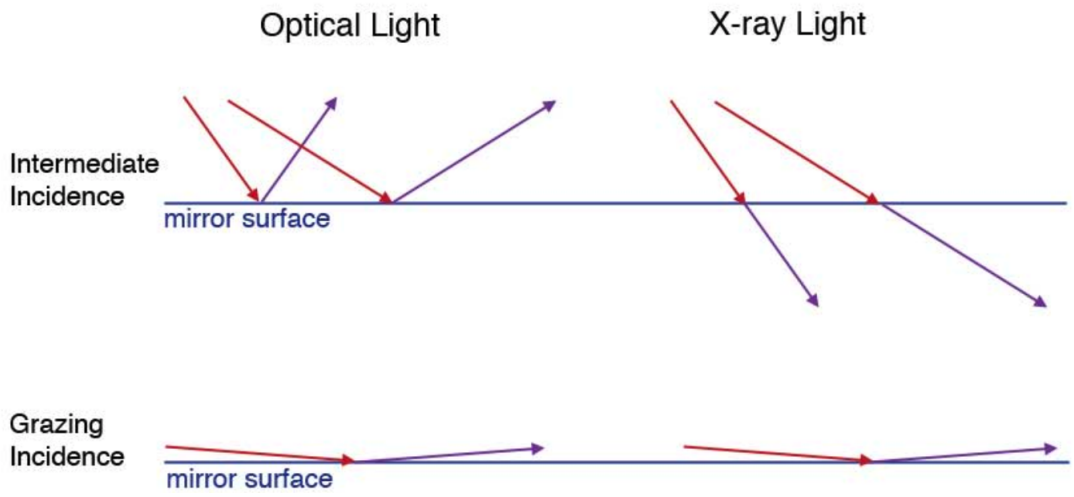

Figure 1.8: The difference in orientation between the mirrors in optical and X-ray telescopes. X-ray telescope mirrors use a very small grazing incidence angle to properly reflect the light towards the focus (`https://xrtpub.cfa.harvard.edu/xray_astro/history.html`).

The X-ray photons are then directed to the telescope focus where the EPIC detectors are. Two of the *XMM Newton* telescopes direct X-rays to MOS (Metal Oxide Semi-conductor) CCDs, and the third direct X-rays to pn CCD camera. The pn camera has a very high time resolution of 0.03 ms in timing mode.

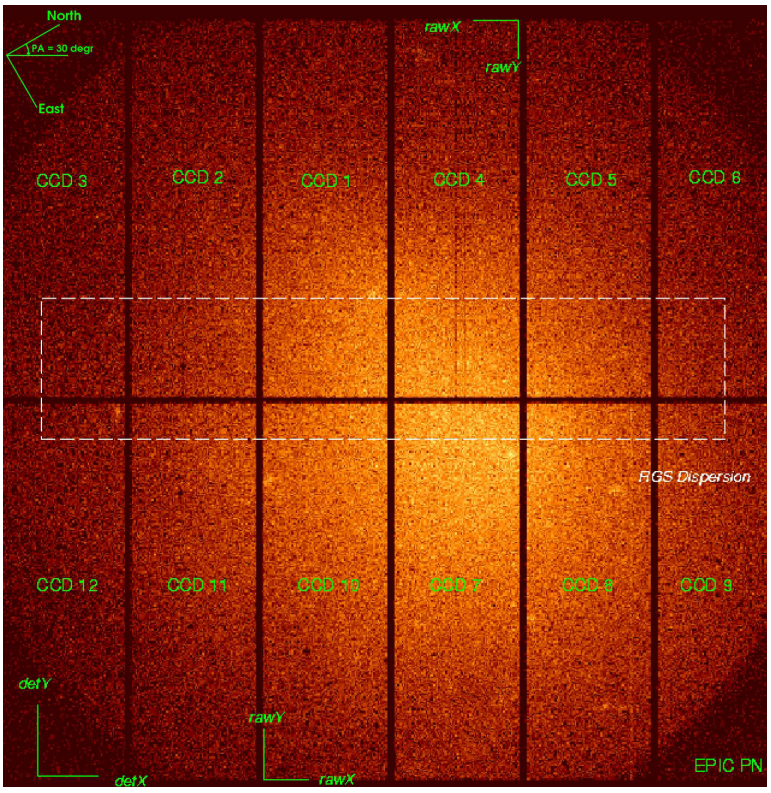

Figure 1.9: Configuration of the pn CCD layout(ESA Handbook).

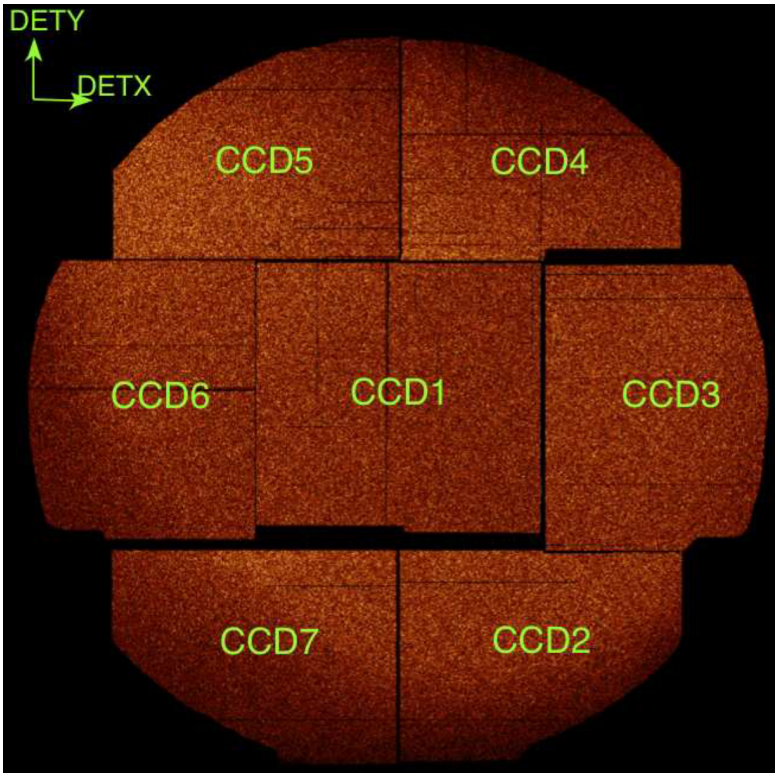

Figure 1.10: Configuration of the MOS CCD layout(ESA Handbook).

There are a few differences between the MOS and pn detectors. First, the chip arrays are significantly different (Fig 1.9 and 1.10). The pn camera is a silicon wafer with 12 CCD chips. The pn chips operate with a significantly faster readout than the MOS, because there is a readout node for each pixel column. The MOS CCDs are front-illuminated, while the pn CCDs are back illuminated. This makes the MOS CCDs more sensitive to lower energies.

What is a CCD?

Old optical telescopes made use of photographic plates to create an image. Modern telescopes use CCDs. CCDs provide a direct connection between the photons emitted by an object and the image created. CCDs are based on the photoelectric effect. If a photon interacts with an electron in the outer shell of an atom, the energy transfer to the electron can be enough to liberate it from the atom. CCDs use a thin silicon wafer to convert photons to electrons. A positively charged capacitor is connected to the silicon wafer to collect the liberated free electrons.

In X-ray astronomy, the photon energy is so high that one photon will liberate many electrons. The number of free electrons is proportional to the energy of the photon. Therefore in X-ray astronomy, CCDs provide spectral information as well as imaging.

Quantum efficiency is the efficiency of a detector to convert incident photons to electrons. If q incident photons result in p events of liberated electrons (multiple liberated electrons count as one event), that is quantified as a quantum efficiency of p/q. Quantum efficiency is a function of photon energy. The quantum efficiencies of the pn and MOS cameras are shown in Fig 1.11 and 1.12[6].

[6]To put these quantum efficiencies into perspective, the quantum efficiency of the human eye in the visible light band ($\sim$2 eV) is approximately 1% (Engstrom 1974).

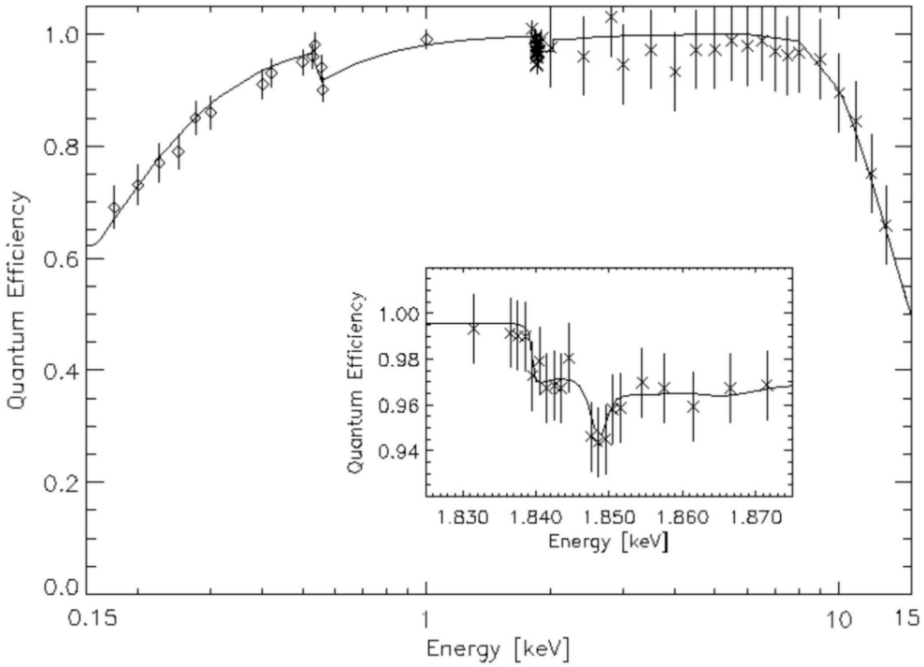

Figure 1.11: Quantum efficiency of the EPIC pn CCD chips, as a function of photon energy(Strüder et al. 2001).

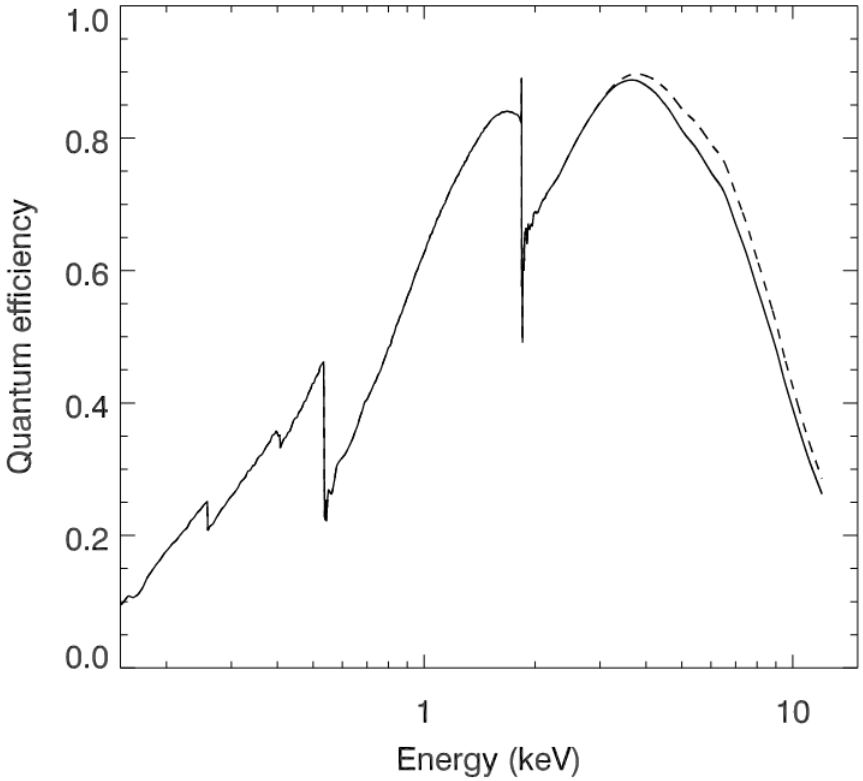

Figure 1.12: Quantum efficiency of the EPIC MOS CCD chips, as a function of photon energy (ESA Handbook).

The photons interact with the electrons in the silicon once the shutter is opened. There is a capacitor connected to the silicon, which collects the free electrons. The voltage across the capacitor represents the number of electrons collected in the capacitor, which can then be used to determine the energy of the observed photon. This setup exists in each pixel of the CCD. There is an array of these pixels, which make up the cameras.

X-ray data

For each detected photon, the EPIC cameras record four variables: x location on the camera, y location on the camera, photon energy E, and arrival time t. It is this set of measurements (x, y, t, E) that allow astronomers to probe into the inner workings of AGNs, and study their host black holes.

By utilizing x and y, astronomers can create an image. From E, we can create spectra. From utilizing the arrival time, we can create light curves to measure how the source brightness changes with time. Light curves are the crux of the work done here.

1.3 Variability

Astrophysical sources which are powered by accretion, such as AGNs, are generally highly variable sources of radiation. AGN X-ray radiation is extremely variable on all observable timescales, from hours to years (Gallo 2011) and may even be extremely variable over a wider range of timescales, from seconds to centuries and longer. This variability provides insight to the physical processes that power these sources.

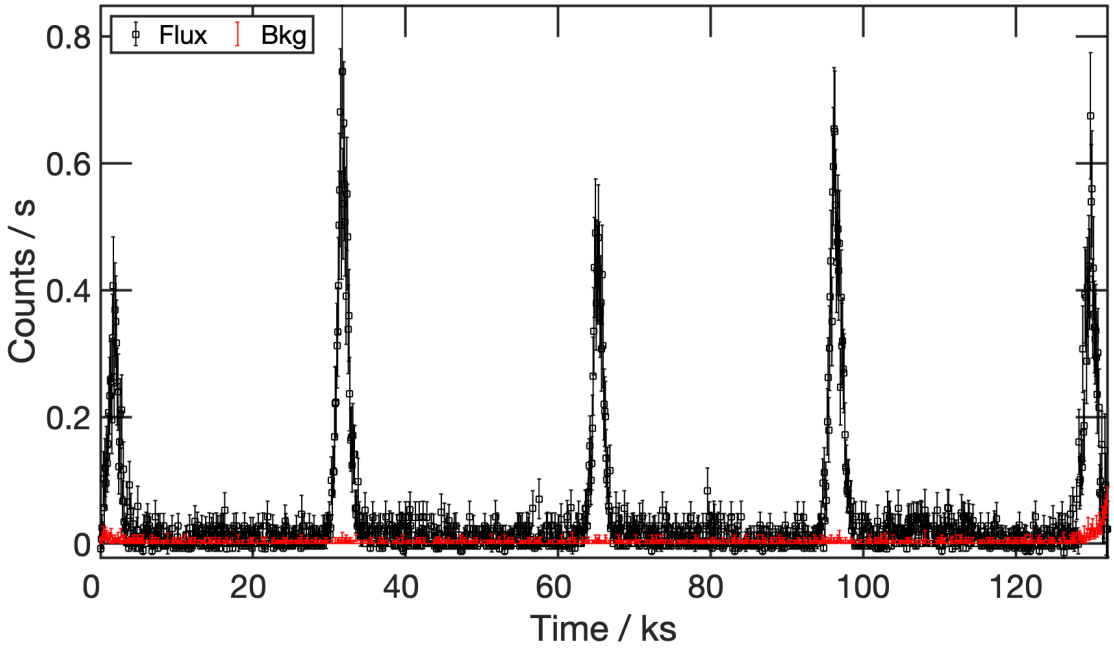

Figure 1.13: An example of an X-ray light curve. This is an *XMM-Newton* observation of GSN 069 (Obs ID: 0851180401). Note the periodic "erupton" behaviour, which is referred to as a "quasi-periodic oscillation", and was a major part of the analysis presented in Chapter 2.

Variability of Seyfert 1 AGNs has been observed over all frequency bands. The correlation between the amplitude of AGN X-ray variability and frequency band, is still largely unknown. For example, there are many cases of light curves in the soft X-ray band exhibiting high amplitude variations over shorter timescales than the hard X-ray band. There is correlation between variability at different frequency bands, which reveals key information about the physics of the radiation source. For example, it is thought that X-ray variations arise from instabilities in the corona, and that optical variations originate in extended/colder parts of the accretion disk (Netzer

2013).

Many studies involving AGN X-ray timing involve Fourier analysis and the Fourier transform. The basis vectors of the Fourier transform are complex exponentials parameterized by frequency f, in the form of $e^{-i2\pi ft}$, that is the $\sin$ and $\cos$ functions, which are a function of time t and span $t \in (-\infty, +\infty)$. Due to the infinite domain where each t contributes the same, the Fourier transform therefore implicitly assumes *stationarity*, which in simple terms can be thought of as the amplitude of the frequency components being constant in time. A characteristic of a stationary process is that the mean and variance of a time series converge to well defined values over sufficiently long timescales (Alston et al. 2019).

However, there is evidence to suggest that AGN X-ray emission may actually be a *non-stationary* process (Gliozzi et al. 2004a). AGN flux has been shown to vary at every frequency range and timescale. The most prominent variations are in the X-ray band (Padovani et al. 2017). The X-ray amplitude variations have been observed on timescales down to ~100 s (Vaughan et al. 2011a). This variation on short timescales implies that the X-ray emitting region is small (Mushotzky et al. 1993).

Seyfert 1 galaxies emit light in a way that appears to be random and aperiodic (Vaughan et al. 2003). This random variability is called noise, and is the manifestation of a stochastic process, instead of a deterministic process. Deterministic processes are common in astrophysics[7]. A stochastic process is an ongoing process in which the next state of the system may depend on the previous state, plus some random element. In a stochastic process, the noise is inherent to the source, and not a result of measurement errors.

A common method for studying a noise process such as AGN X-ray emission, is looking at the fluctuations in the Power Spectral Density (PSD). The PSD, $\mathcal{P}(f)$ can be estimated from an ensemble of periodograms, $P(f)$. $P(f)$ is calculated from the modulus square of the Fourier

[7] An example of a deterministic process is the orbit of a celestial body around a central object.

transform of the light curve (Uttley et al. 2014):

$$P(f) = \frac{2\Delta t}{\langle x \rangle N} |X(f)|^2, \tag{1.15}$$

where N is the number of data points; $\Delta t = (t_{max} - t_{min})/N$ is the sample spacing of the lightcurve; $\langle x \rangle$ is the mean flux which is strictly positive; and $X(f)$ is the Fourier transform of the light curve $x(t)$. Figure 1.14 shows an example of a periodogram calculated from an observation of IRAS 13224-3809.

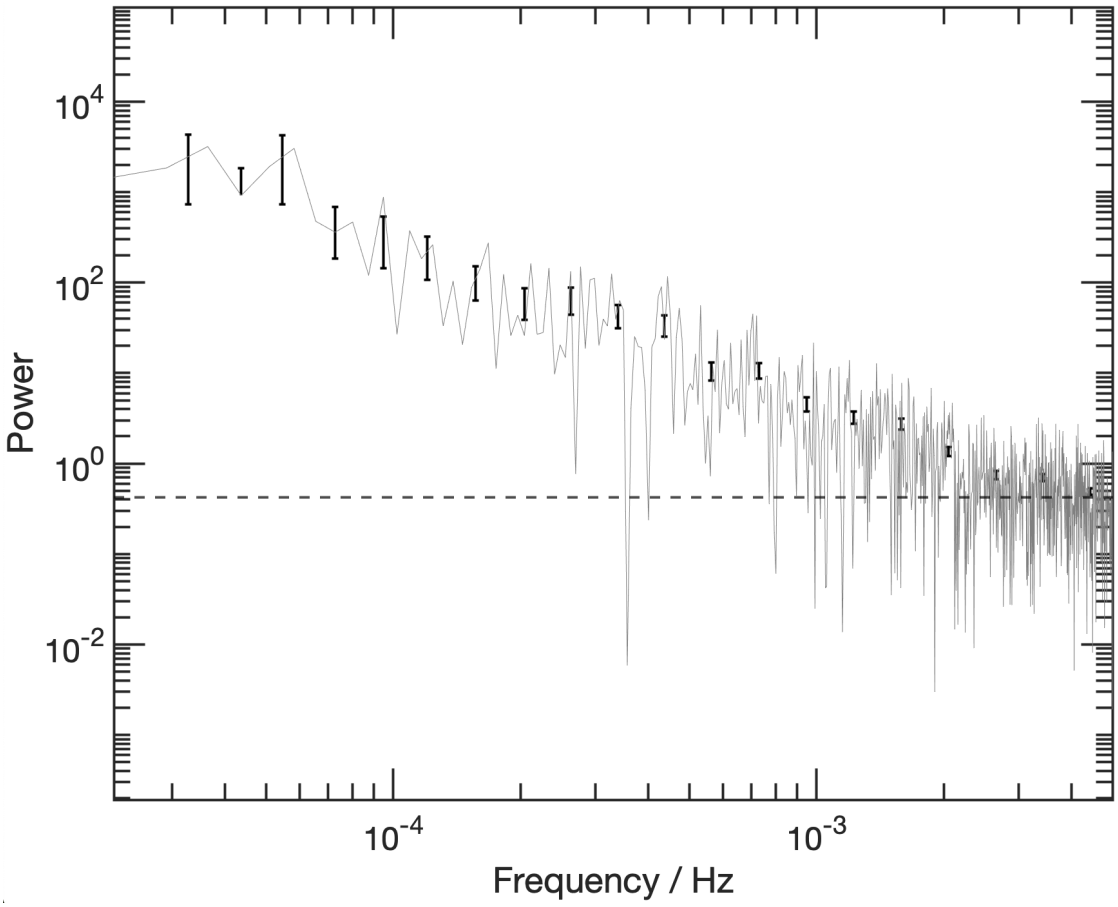

Figure 1.14: An example of a periodogram of an X-ray light curve. This is an *XMM-Newton* observation of IRAS 13224-3809, revolution 3044. The light grey line represents the raw PSD, which contains as many data points as the light curve. The data points with error bars represent the binned PSD. Since it is customary to plot the PSD with the frequency axis on a log scale, the PSD is then "geometrically binned", which results in the data points being evenly spaced in log space. So instead of each bin containing an equal number of data points, each subsequent bin contains 1.3 times more data points than the previous bin.

The Fourier transform can be defined as:

$$X(f) = \int_{-\infty}^{+\infty} x(t) e^{-2\pi i f t} dt \tag{1.16}$$

The PSD of X-ray variability from Seyfert galaxies, or any active galaxies, can usually be parameterized by the power-law α (Vaughan et al. 2003). The power law in its simplest form is:

$$\mathcal{P}(f) \propto f^{-\alpha} \tag{1.17}$$

For Seyfert galaxies, the index of the X-ray PSD is typically $\alpha \in [1, 2]$. The index $\alpha = 0$ corresponds to a "white noise" spectrum, where the power is constant across all frequencies. A steeper power-law of $\alpha \gtrsim 1$ corresponds to a "red noise" spectrum, where there is greater power at lower frequencies.

1.3.1 Stochasticity of AGN X-ray Emission

As mentioned, AGN variability is governed by an underlying stochastic process, as opposed to a deterministic one. An implication of this is that a measurement of the light curve and its periodogram, are just one instance of the ensemble of all possible realizations of light curves and periodograms. A second measurement can vary by more than just the expected measurement errors, due to the inherent randomness of a stochastic process. Due to this, statistical moments such as mean and variance can vary from one observation to the next. It is therefore important to study the distribution of statistical moments from an ensemble of realizations of the process, and if the expectation values of these statistical moments are time-dependent (Alston et al. 2019).

1.3.2 Non-Stationarity: Weak and Strong

One way of defining a stationary process, is that the statistical properties are independent of time. However, when studying a red noise process, changes in the statistical moments are not a strong claim that the process is non-stationary (Vaughan et al. 2003). Instead, it is preferable to check the time dependence of the expectation values of the statistical moments, such as the variance.

One useful statistic is from the integrated power of the PSD, to calculate the expectation value of the "true" variance between the frequencies, f_1 and f_2, corresponding to the timescale $t \in [1/f_1, 1/f_2]$ (Vaughan et al. 2003):

$$\langle S^2 \rangle = \int_{f_1}^{f_2} \mathcal{P}(f) df \tag{1.18}$$

A red noise process which results in a steep PSD with $\alpha \gtrsim 1$, will result in the integrated power diverging in the limit as f approaches 0. A consequence of this is that there is no well-defined mean (Press & Rybicki 1997). This type of variability is defined as *weakly non-stationary*.

For a physical process, the power must be finite and therefore the PSD must become flat at low frequencies, that is, for a sufficiently long observation[8], $\alpha < 1$ at low frequencies. However, for AGN these low frequencies are only apparent in long observations that are not always accessible with current X-ray telescopes. Therefore this weak non-stationarity is an effect of the typical observation timescales of AGN light curves, and for the length of a typical AGN X-ray observation, the time series should be assumed to be weakly non-stationary (Alston et al. 2019).

While an AGN X-ray observation is first assumed to be at least weakly non-stationary, sometimes the variability can change with time, that is, the PSD is not constant in time. A time series

[8]The timescale to observe the low-frequency rollover is dependent on the black hole mass, but for $M/M_\odot \sim 10^6$, this rollover occurs at $\sim 10^{-6}$ Hz (McHardy 2001), corresponding to a timescale of approximately 12 days. *XMM-Newton* can only make a continuous observation for approximately 1.5 days.

with a time-dependent PSD is called *strongly non-stationary*, and suggests that there may be some underlying physical process present in the AGN that is causing changes to the PSD.

One of the major goals of X-ray astronomy is to distinguish between these two processes, weak and strong non-stationarity. Are the changes in variance caused by the random fluctuations due to red noise (weak non-stationarity), or from the physical processes which influence the X-ray emission from the AGN (strong non-stationarity)? If the ongoing process in the AGN is truly stationary, and therefore its PSD does not change with time, the expected variance should be constant across different time segments (the individual variances will still fluctuate). With enough data, one can determine from an ensemble of light curves if the expected variances are consistent with what would be expected in a stationary process.

1.4 The Wavelet Transform

A drawback of Fourier analysis and the Fourier transform is that it assumes the input signal is stationary and that the amplitudes of each frequency component are constant in time[9]. While this assumption was valid for Jean-Baptiste Joseph Fourier solving for the heat distribution of a metal bar in the 1810's, for the analysis of X-ray emission from an active galaxy this assumption may not hold (Hovatta et al. 2008).

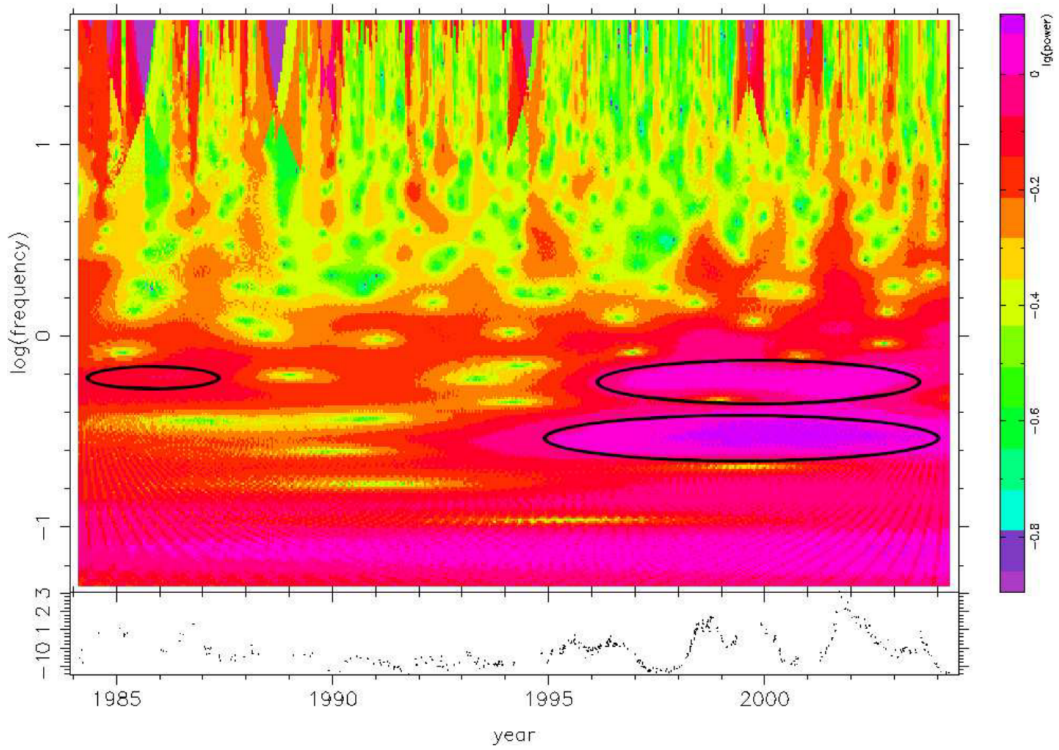

Figure 1.15: An example of a wavelet transform of an AGN X-ray light curve (Hovatta et al. 2008).

The wavelet transform uses basis vectors known as wavelets or the mother wavelet, denoted by $\psi(t)$. The wavelet undergoes a series of two different types of transformations: translation and dilation. This picks out which frequencies are prominent at each point in time (e.g. Fig 1.15).

Any wavelet basis vector must obey the following mathematical requirements:

[9]This is a very simplified explanation of stationarity. A more detailed explanation is described in Alston et al. (2019).

1. Finite energy:

$$E = \int_{-\infty}^{+\infty} |\psi(t)|^2 dt < \infty$$

2. For the Fourier transform of $\psi(t)$, denoted by $\hat{\psi}(f)$[10], the wavelet must have no zero-frequency component. In other words, the admissibility constant C_g must be finite:

$$C_g = \int_0^{\infty} \frac{|\hat{\psi}(f)|^2}{f} df < \infty$$

The wavelet transform does not make any assumption of stationarity, and thus could be useful for the study of AGN variability signals. While the Fourier transform basis vectors ($\sin$ and $\cos$, i.e. complex exponential $e^{i\phi t}$) span over all t equally, the wavelet transform is designed such that its basis vectors do not give equal "weight" to each t.

The wavelet transform can be thought of as an extension of the Fourier transform, with the output being a function of frequency *and* time, which differs from the Fourier transform output, which is a function of only frequency.

1.4.1 Definition of the Continuous Wavelet Transform

Generally, the translation and dilation of the wavelet are parameterized by a and b, respectively. Therefore, the wavelet takes on the form:

$$\psi(t) \rightarrow \psi\left(\frac{t-b}{a}\right) \tag{1.19}$$

[10]The Fourier transform $\hat{\psi}(f)$ of a signal $x(t)$ can be defined as:

$$\hat{\psi}(f) = \int_{-\infty}^{+\infty} x(t) e^{-2\pi i f t} dt$$

The wavelet transform $T(a, b)$ of a signal $x(t)$ is then defined as the integral over all time of the signal multiplied by the complex conjugate[11] of the wavelet:

$$T(a,b) = w(a) \int_{-\infty}^{+\infty} x(t) \psi^* \left(\frac{t-b}{a} \right) dt \tag{1.20}$$

Here, $w(a)$ is the "weighting function", which scales the amplitude at each frequency. A common choice for this is $w(a) = 1/\sqrt{a}$, as it results in the wavelets at each frequency containing the same energy.

An alternate definition for the wavelet transform is that it is the cross-correlation of a signal $x(t)$ with a set of wavelets parameterized by their widths b (Figs 1.16 and 1.17). Quoting Addison (2017): *"The wavelet transform has been called a 'mathematical microscope', where b is the location on the time series being 'viewed' and a is associated with the magnification at location b."*

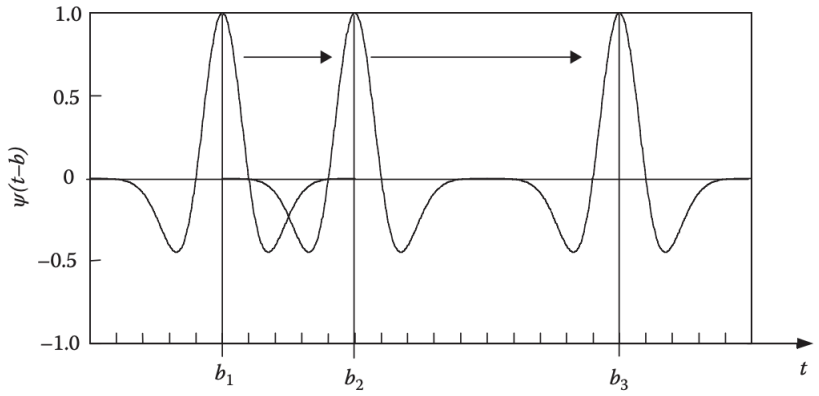

Figure 1.16: Wavelet transform basis function translated to various positions b_n (Addison 2017).

[11] The complex conjugate z^* of a complex number $z = a + ib$ is $z^* = a - ib$. Equivalently, for $z = e^{i\phi}$, $z^* = e^{-i\phi}$.

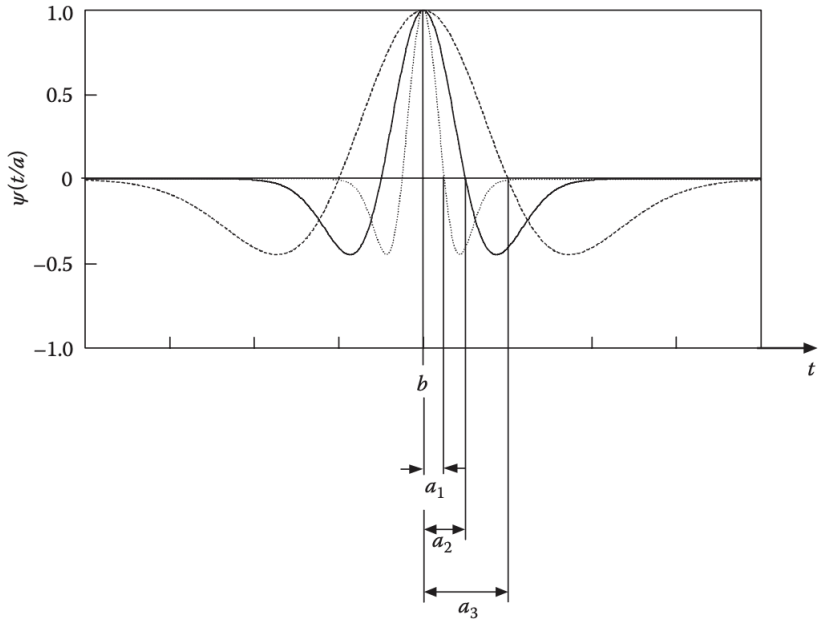

Figure 1.17: Wavelet transform basis function dilated to various scales a_n (Addison 2017).

When applied to signals of physical phenomena, such as the number of counts of X-ray photons over time, the translation and dilation factors a and b in the wavelet transform can be replaced with time t and frequency f, respectively. Thus the wavelet transform definition becomes:

$$T(t,f) = w(f) \int_{-\infty}^{+\infty} x(t')\psi^* \left(\frac{t'-t}{f} \right) dt' \tag{1.21}$$

1.4.2 Choice of Wavelet transform basis vectors

Unlike the Fourier transform, which has its standard basis vectors, the wavelet transform does not, and therefore a choice must be made (Fig 1.18). This can be seen as a drawback to the wavelet method, as it is possible that a difference in choice of basis vector can lead to different results. For X-ray astronomy a common choice is the “Morlet wavelet”. The Morlet wavelet can be thought of as a complex exponential multiplied by a Gaussian window. The reason this is a useful basis vector is its symmetry with the Fourier transform, which assumes the signal is

composed of a sum of sine and cosine waves. A general form of the Morlet wavelet is:

$$\psi(t) = \pi^{-1/4} \left(e^{i2\pi f_0 t} e^{-(2\pi f_0 t)^2/2} \right) e^{-t^2/2}, \tag{1.22}$$

where f_0 is the central frequency of the wavelet. It is common that $f_0 >> 0$, which results in the second factor being negligible. The Morlet wavelet can then be expressed as:

$$\psi(t) = \pi^{-1/4} e^{i2\pi f_0 t} e^{-t^2/2}. \tag{1.23}$$

In this form, it is clear that the Morlet wavelet is the product of a complex exponential, and a Gaussian window (and a normalization factor).

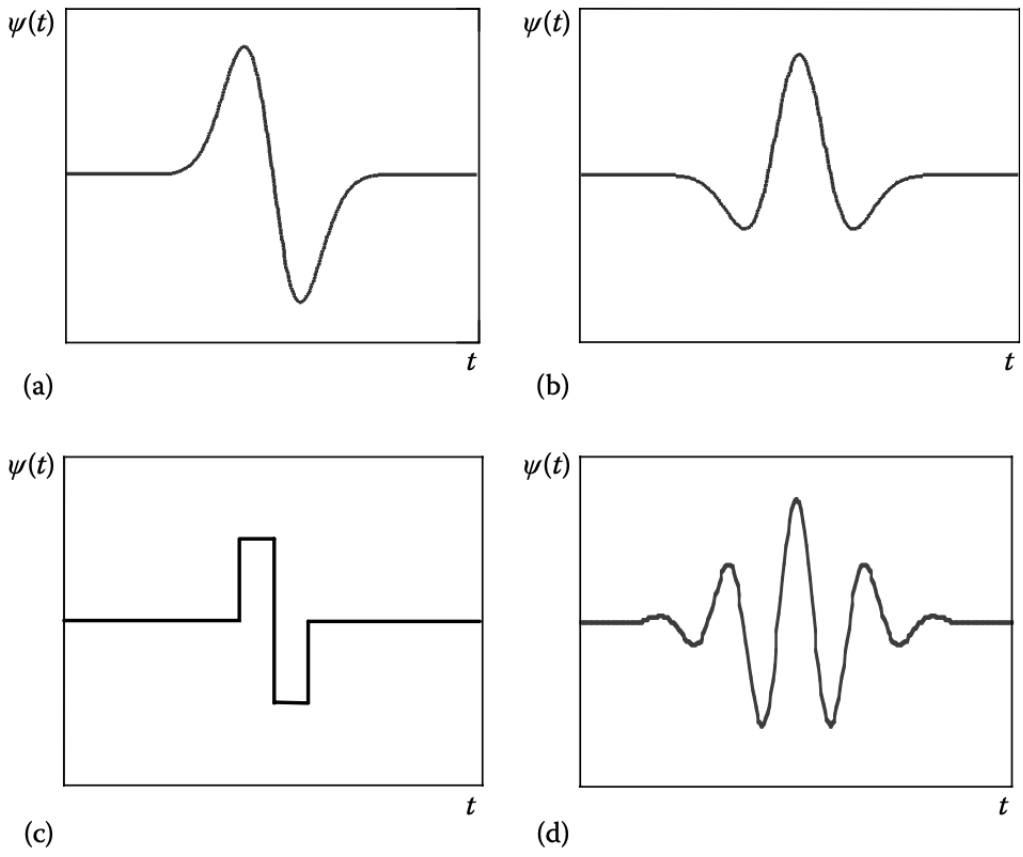

Figure 1.18: Some example wavelet basis vectors: a) Gaussian wave; b) Mexican hat; c) Haar; d) Morlet (real part). (Addison 2017)

1.4.3 Wavelet Power Spectrum

Due to the complex nature of the wavelet basis vectors $\psi(t, f)$, and the Fourier transform, the wavelet transform T is generally complex. It is common in physics when dealing with complex quantities such as a Fourier transform or wavefunction of a particle, to take the modulus square which is always real [12]. Thus the wavelet power spectrum $|T(t, f)|^2$ is defined as:

$$|T(t, f)|^2 = T^*(t, f)T(t, f) \tag{1.24}$$

From the wavelet power spectrum, the global wavelet power spectrum $G(f)$ can be calculated:

$$G(f) \propto \int_{-\infty}^{+\infty} |T(t, f)|^2 dt \tag{1.25}$$

The global wavelet power spectrum will resemble a smoothed Fourier power spectrum (PSD).

1.4.4 Cone of Influence

Since the Fourier transform assumes the input signal is cyclic and is part of the wavelet transform calculation, and we are analyzing finite-length signals, there will be errors at the start and end of the wavelet power spectrum. The cone of influence is described in Torrence & Compo (1998).

One fix for this is padding zeros at the start and end of the signal, computing the wavelet transform, and then removing these zeros. It is typical to add an amount of zeros such that the total number of elements in the signal is the next highest power of 2. This speeds up the computation of the fast Fourier transform. However, padding with zeros adds discontinuities at the signal boundaries, and at large scales causes a drop in amplitude of the wavelet power

[12] This is apparent using the polar representation of a complex number with magnitude r and phase ϕ, $z = re^{i\phi}$.

$$|z|^2 = z^* z = (re^{i\phi})^* re^{i\phi} = r^2 e^{-i\phi} e^{i\phi} = r^2$$
$$\therefore |z|^2 \in \forall\, \phi$$

spectrum near the edges, as more zeros are added.

The cone of influence (COI) is the region of the wavelet power spectrum where the effects of the edge of the signal on the wavelet power spectrum become important. It is important to distinguish this region, as features may arise in this region that are an artefact of the wavelet transform, rather than the signal itself (Fig 1.19).

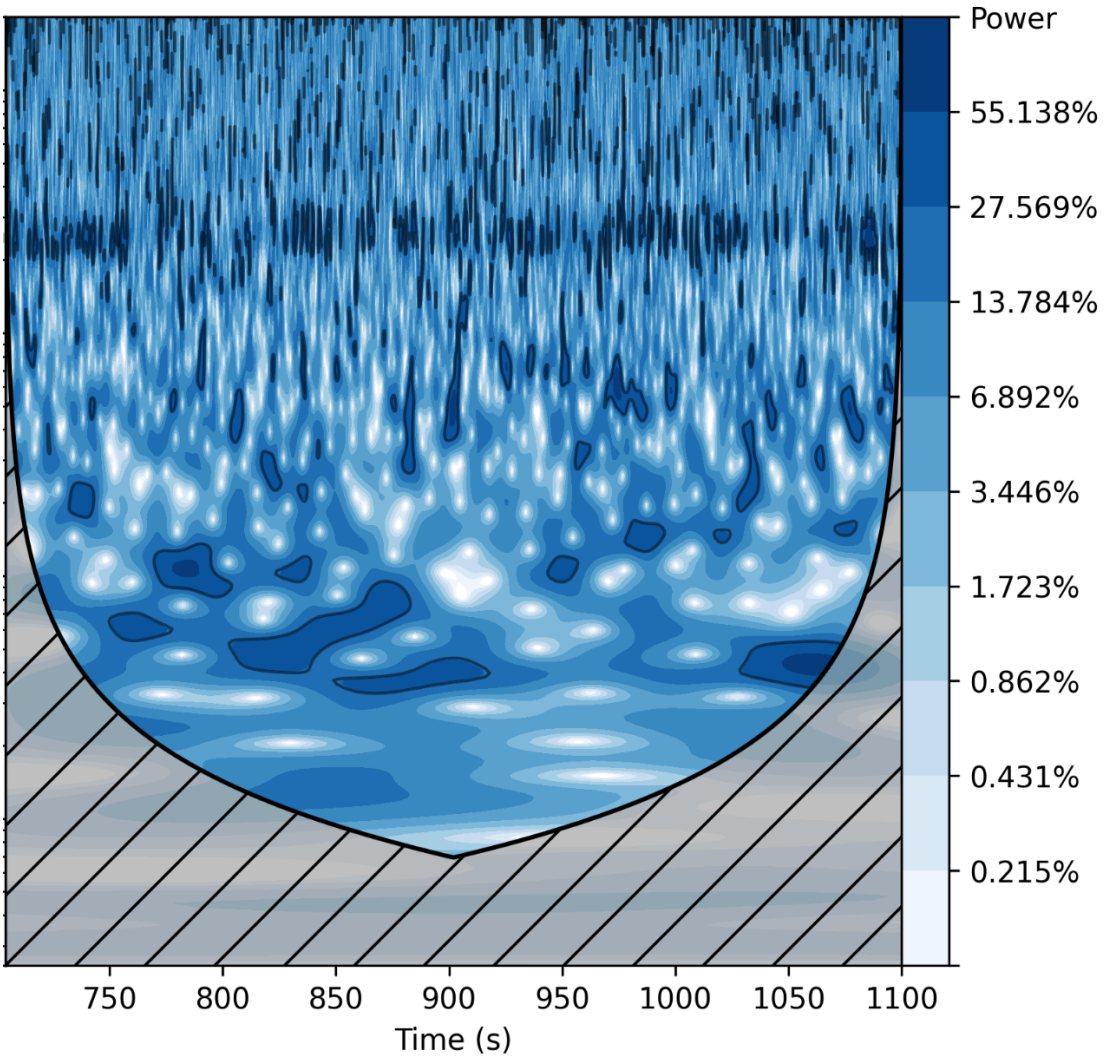

Figure 1.19: Wavelet power spectrum of an observation of the X-ray binary MAXI J1535-571. The greyed hashed area represents the cone of influence, where the wavelet power information is disregarded (Chen et al. 2022).

1.5 This Work

In this work, we will examine the application of wavelet analysis to AGN X-ray light curves. In Chapter 2 we introduce the wavelet concept in depth. The method for simulating AGN light curves is explained therein. The method for calculating the significance regions of the wavelet transform is presented next. This analysis approach is then applied to four unique objects: Ark 120, IRAS 13224-3809, RE J1034+396, and the QPE GSN 069. The results of this analysis are then discused. In Chapter 3, we will apply wavelet analysis to the AGN NGC 6814. This AGN underwent an eclipse during one of the observations in our data set. The wavelet results will be discussed. The results from the thesis are summarised in Chapter 4.

Chapter 2

Applying wavelet analysis to the X-ray light curves of active galactic nuclei and quasi-periodic eruptions

Note: This chapter was accepted for publication on July 26th 2023 in the Monthly Notices of the Royal Astronomical Society, in collaboration with L.C. Gallo and A.G. Gonzalez[1].

2.1 Introduction

Active galactic nuclei (AGN) consist of an accretion disk surrounding a host supermassive black hole (SMBH). The X-rays originate from a compact corona of hot electrons located close to the black hole. X-ray radiation from AGN can be extremely variable on all observable timescales, from hours (e.g. Vaughan et al. 2003; Paolillo et al. 2004; Gallo et al. 2018) to years (e.g. Markowitz & Edelson 2001; Gonzalez-Martin & Vaughan 2012). This variability provides insight to the physical processes that power these sources (e.g. Vaughan et al. 2003; Uttley et al.

[1] https://arxiv.org/abs/2306.14972

2014). Current analyses of this variability are usually based on Fourier techniques like the power spectral density (PSD) and lag-frequency analysis. Fourier techniques operate in the frequency domain and provide the average frequency distribution throughout the entire time series, but there is no time localization.

The Fourier transform assumes a stationary time series. For a stationary X-ray light curve, the count rate will be log-normally distributed and exhibit a linear rms-flux relation (Uttley et al. 2005; Alston 2019). However, there is evidence to suggest that AGN emission is actually non-stationary (e.g. Gliozzi et al. 2004b; Alston 2019). The defining characteristic of a stationary time series is that all of its statistical moments are constant (strong stationarity). A weakly stationary time series implies only the mean and variance remain constant (the first and second statistical moments). However, because of the scatter in the statistical moments that are intrinsic to red noise stochastic processes, different realizations of the same process can look very different from one observation to another, even with identical underlying properties (e.g. the PSD and probability distribution function [PDF]). In a time series analysis, we would like to infer the underlying physical process and not a single instance of that process which is affected by its stochastic nature (whether stationary or not), therefore it is useful to examine the time dependence of the expectation values of the statistical moments (Vaughan et al. 2003).

Physical changes to the AGN such as changes to the accretion disk or corona geometry could lead to non-stationarity in the flux variability (e.g. Alston et al. 2019, Panagiotou et al. 2022). In general, a non-stationary process could be attributed to the properties generating that process being dynamic.

Panagiotou et al. (2022) set out to explain the recent trend of lower-than-expected correlations between UV and X-ray emissions from the same object, where a correlation is expected when UV reprocessed emission from the accretion disk is driven by the X-ray illumination of the disk from the Comptonized photons of the corona. They discuss how the cross-correlation

function assumes that the input time series are stationary, as this is what causes a constant lag between the time series. In their simulations, the reprocessed UV emission depends on the X-ray emission and a response function which encodes the processes taking place in the accretion disk. The input parameters for the simulation correspond to the geometry and physical state of the AGN. More specifically, the height of the corona above the plane of the accretion disk (geometry), and the power law for the X-ray energy spectrum for the corona (physical state). For a static system, both of these parameters are held constant, and from this a stationary process would arise as there would be a single response function governing the reprocessing. However, when the system is dynamic, i.e. either the geometry or physical state have some time dependence, there must be a set of response functions, each corresponding to a point in the parameter space. Not only would this cause a lower-than-expected cross-correlation, it would also cause the AGN emission to be non-stationary.

Wavelet analysis, and more specifically the wavelet transform, can be thought of as an extension to the Fourier transform where the frequency decomposition can be carried out as a function of time. Unlike in the Fourier transform where the time information is lost, the wavelet analysis combines the time and frequency domains. In the most general sense, there are two overall types of wavelet transforms: the discrete wavelet transform (DWT), and continuous wavelet transform (CWT). The DWT is typically used for "practical" applications such as image processing (e.g. Broughton 1998, Chang & Girod 2007, Chervyakov et al. 2018); communications (e.g. Akansu et al. 1998, Saad et al. 2010, Baig et al. 2018); and data compression, especially in the medical field (e.g. Badawy et al. 2002, Qu et al. 2003, Jha & Kolekar 2021). The CWT is typically used for data analysis and scientific research such as seismology (e.g. Li et al. 2009, Karamzadeh et al. 2012, Balafas & Kiremidjian 2015); medicine (e.g. Bostanov 2004, Cheng et al. 2010, Komorowski & Pietraszek 2016); finance (e.g. Kristoufek 2013, Olayeni 2016, Tiwari et al. 2016); and understanding the impact of COVID-19 on the stock market (e.g. Caferra & Vidal-Tomás

2021, Goodell & Goutte 2021, Umar et al. 2022).

In general astronomy, wavelet analysis has been used to study chromospheric variations in main sequence stars (Frick et al. 1997); connecting different solar periodicities to a common physical mechanism (Krivova & Solanki 2002); deviations in the vertical structure of the outer Galactic HI disk (Levine et al. 2006); quasi-periodic pulsations of solar flares (Dominique et al. 2018); short-lived, narrow-banded solar emission peaks (Suresh et al. 2017); and searching for periodicities in the optical light curves of the blazar S5 0716+714 (Gupta et al. 2008).

In the study of AGN and compact objects, wavelet analysis has been used to study the characteristic timescales (radio frequencies) of a large sample of AGN (Hovatta et al. 2008); the X-ray variability of ultraluminous X-ray sources over large timescales (Lin et al. 2015); constraining the temperature of the intergalactic medium using high-redshift quasars (Wolfson et al. 2021); transient quasi-periodic oscillations (QPOs) in low-mass X-ray binaries (Chen et al. 2022); the search for QPOs in the γ-ray light curves of blazars (Ren et al. 2022); characterizing the X-ray flickering of cataclysmic variables (Anzolin et al. 2010); and the possible detection of a QPO in the narrow-line Seyfert 1 galaxy MCG 06 30 15 (Gupta et al. 2018).

Wavelet analysis is relatively underused in the field of AGN X-ray astronomy. In this chapter we will examine the application of the wavelet transform power spectrum on the X-ray light curves of AGN and quasi-periodic eruption (QPE) sources. In Sec. 2.2, we discuss the specifics of wavelet transforms. In Sec. 2.3, we discuss the simulations used for testing and in Sec. 2.4 we apply the wavelet analysis to four AGN systems. We discuss and summarise our results in Sec. 2.5.

2.2 Wavelet Transforms

The wavelet transform is similar in essence to the Fourier transform as it calculates the frequencies present in a time series. However, there is a key difference. The Fourier transform is averaged over the entire series and all time domain information is lost. On the other hand, the wavelet transform preserves the timing information and therefore can be used to identify when specific frequencies appear in the time series. For a comprehensive review of wavelet transforms, see Torrence & Compo (1998) and the textbook by Addison (2017).

Similar to how the Fourier transform expresses the time series as a sum of sines and cosines, the wavelet transform uses basis vectors known as wavelets or the mother wavelet, denoted by $\psi(t)$. The wavelet undergoes a sequence of two different transformations, one in translation and the other in dilation. The combination identifies the different frequencies that are prominent at each point in time.

The wavelet transform does not assume a stationary time series (for a review of stationarity, see Alston et al. 2019) and, in principle, can be used on data with uneven sampling (e.g. Foster 1996, Daubechies et al. 1999, Bravo et al. 2014). Consequently, wavelet analysis should be ideal to study AGN X-ray light curves. For this work, computations of the continuous wavelet transform are carried out using the MATLAB application called WAVELET TOOLBOX.

The wavelet transform $T(a, b)$ of a time series $x(t)$ is defined as the integral over all times of the series multiplied by the complex conjugate of the wavelet basis vector (Addison 2017):

$$T(a,b) = w(a) \int_{-\infty}^{+\infty} x(t) \psi^* \left(\frac{t-b}{a} \right) dt, \tag{2.1}$$

where $w(a)$ is the weighting function. In the WAVELET TOOLBOX, $w(a)$ is chosen such that it uses L1 normalization, which preserves wavelet power spectrum amplitudes at different frequencies (Misiti et al. 1996). In other words, with the L1 normalization scaling, the time series

$y(t) = A_i \sin(f_i t) + A_j \sin(f_j t)$, will have the wavelet power spectrum amplitudes proportional as A_i/A_j for any f_i and f_j.

The parameters a and b represent the scaling and shifting of the wavelet basis vector ψ, respectively. The scaling parameter is similar to the scaling in the Fourier transform, which represents each frequency component. Therefore a can be considered equivalent to the Fourier frequency. The shifting parameter is not present within the Fourier transform and represents the time information that is lost when taking a Fourier transform. Therefore, the shift parameter b can be considered as the time. In practice, the wavelet transform takes on the form $T(t, f)$, that is, a function of time and frequency. For $\psi = e^{i2\pi t/a}$, Eq. 2.1 reduces to the Fourier transform.

Typically, the wavelet transform is calculated using a convolution between x and the Fourier transform of ψ, denoted as Ψ. The convolution theorem states that the Fourier transform of the convolution of two vectors is equal to the products of their respective Fourier transforms. This is useful, because convolution takes care of the shifting aspect of the wavelet transform.

Like the Fourier transform, the wavelet transform is not restricted to the real numbers, and can exist over the complex numbers. Similar to how the PSD of a time series is defined by the modulus square of the Fourier transform (Uttley et al. 2014), the wavelet power spectrum, $W(t, f)$, is defined as the modulus square of the wavelet transform (Torrence & Compo 1998):

$$W(t, f) = |T(t, f)|^2. \tag{2.2}$$

When calculating the wavelet power spectrum of a time series, a wavelet basis vector (mother wavelet) must be defined. While this step may appear arbitrary and could arguably lead to differing results, in essence it is no different with the Fourier transform because the choice of the basis functions are the sine and cosine functions (i.e. complex exponential). The wavelet basis functions are typically orthogonal and complex.

A commonly used wavelet basis is the Morlet wavelet, which is a complex exponential multiplied by a Gaussian window. One useful aspect of the Morlet wavelet is its symmetry with the Fourier transform, which is a complex exponential spanning all t. The Morlet wavelet at a central frequency of f_0 is defined by Torrence & Compo (1998) as:

$$\psi(t, f) = \pi^{-1/4} e^{i2\pi f_0 t} e^{-t^2/2}. \tag{2.3}$$

Another commonly used wavelet basis vector is the generalized Morse wavelet (Lilly & Olhede 2008), which is defined in the time domain as:

$$\psi_{P,\gamma}(t) = \frac{1}{2\pi} \int_0^\infty a_{P,\gamma} f^{\frac{P^2}{\gamma}} e^{-f\gamma} e^{ift} df. \tag{2.4}$$

The generalized Morse wavelet is parameterized by the time-bandwidth (P) and symmetry (γ). The parameter P controls the time/frequency variance. A low value results in a wavelet that is more localized in time and spread out in frequency, while a high value of P results in a wavelet that is more localized in frequency and spread out in time. In the WAVELET TOOLBOX, this parameter can exist in the range $P \in [\gamma, 120]$.

The γ parameter dictates the symmetry of the wavelet about the central frequency $f_c = (P/\gamma)^{2/\gamma}$. The wavelet is most symmetric when $\gamma = 3$ (Lilly & Olhede 2008). For this work, γ is held constant at 3, and $P = 60$, which is the MATLAB default value, was used for each wavelet power spectra unless specified otherwise. The parameter $a_{P,\gamma}$ is a normalization constant.

The translation and dilation of the wavelet basis vector is ultimately what identifies the prominent frequencies at points in time. The wavelet power spectrum can essentially be thought of as the modulus square of the inner product between the time series and the wavelet basis vector at each time–frequency pairing, up to some resolution.

2.3 Simulations

To test the effectiveness of wavelet analysis for AGN X-ray light curves, several investigations are carried out on simulated light curves. Before presenting specific simulations, we describe how the light curves are generated and how the wavelet transform can be examined.

2.3.1 Method for Simulating AGN X-Ray Light Curves

The simulations are based on the method of Emmanoulopoulos et al. (2013), which uses an iterative method to build off the classic light curve simulations of Timmer & Koenig (1995), which generates Gaussian distributed light curves for a given PSD. Emmanoulopoulos et al. (2013) uses phase and amplitude adjustments to modify the Timmer & Koenig (1995) light curves, such that their flux can be described by some specified distribution. This better replicates AGN X-ray light curves, which typically have fluxes that are log-normally distributed (Uttley et al. 2005).

The three input parameters in the Emmanoulopoulos et al. (2013) method are the light curve flux distribution, PSD, and number of iterations. For the flux distribution, if a simulated light curve was meant to replicate an observation, the distribution of that observation was adopted; otherwise, a theoretical log-normal distribution was used. For the PSD, a simple power law functional form of $P(f) \propto f^{-\beta}$, where β is the power law slope, was used, with the option to add in one or multiple Lorentzian profiles to replicate QPOs. For each simulation, 80 iterations were used as the process typically converges after ~ 50 iterations.

Due to the counting nature of AGN X-ray emission, these light curves are a Poisson process and therefore contain a Poisson noise component. The Poisson noise component is added to the simulated light curve x_{sim} by resampling each point at times t_i from a Poisson distribution based on the bin size Δt (Emmanoulopoulos et al. 2013):

$$x(t_i) = \frac{Pois(\mu = x_{sim}(t_i)\Delta t)}{\Delta t}, \tag{2.5}$$

where μ is the mean of the Poisson distribution being sampled. All of the observed and simulated light curves in this work have a bin size of 100 s.

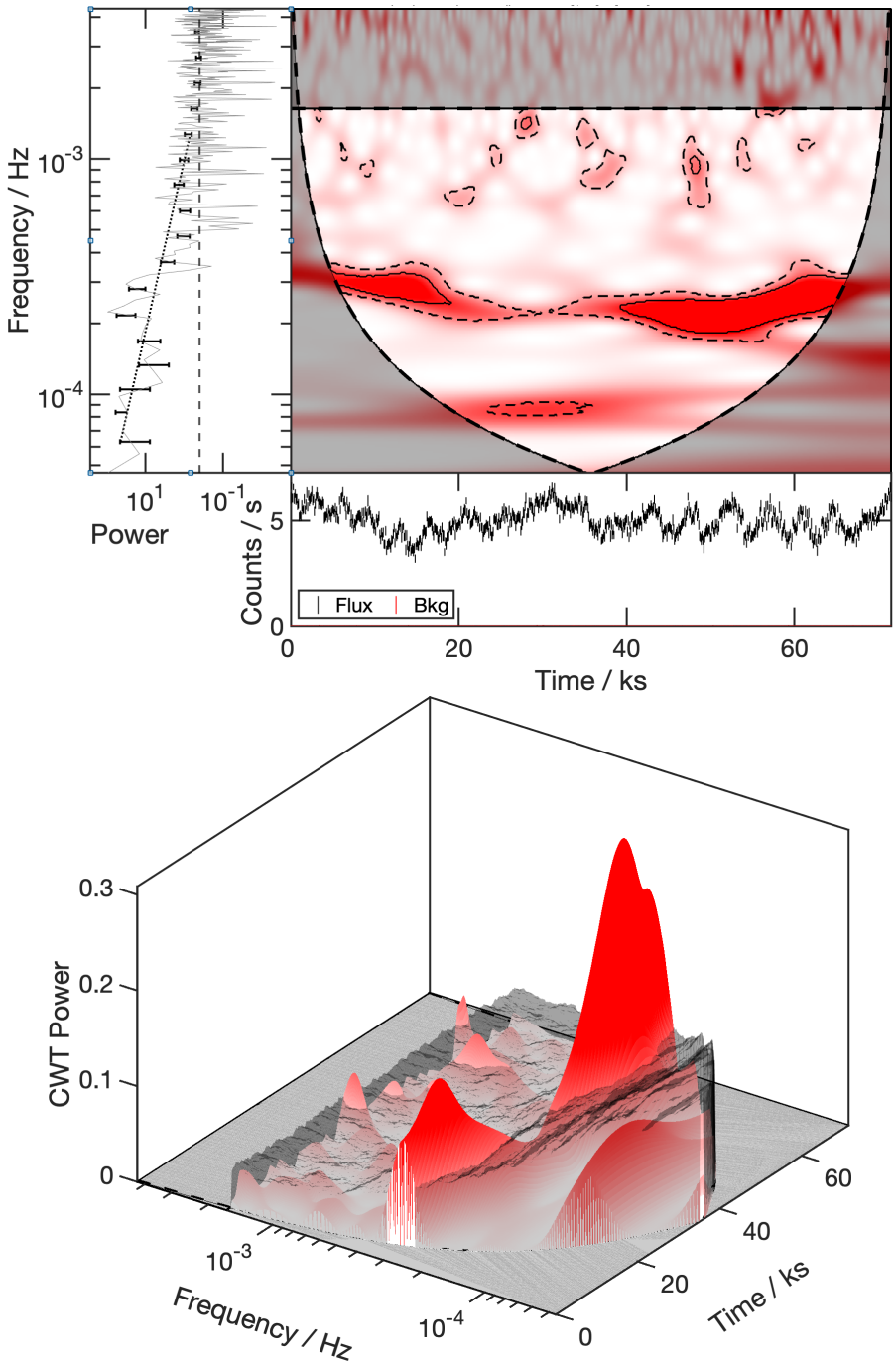

Figure 2.1: The wavelet power spectrum of a simulated time series consisting of an underlying red noise continuum, with a Lorentzian component at 2.5×10^{-4} Hz. The generalized Morse wavelet parameters used were $\{\gamma, P\} = \{3, 60\}$. Upper panel: The shade of red represents the wavelet power. The curved lines in the upper-right panel defines the cone of influence (COI). The shaded (grey) regions below the COI and above the Poisson noise line mark the frequencies that should be treated with caution. The regions in the dashed contour lines represent the amplitudes that are significant at the 90% level (S_{90}), and the solid contour lines are are significant at the 99% level (S_{99}). In the PSD on the left, the vertical line marks the Poisson noise level and the dotted line is the best-fit to the binned PSD used to estimate the underlying noise in the light curve (lower panel). Lower panel: The 3-dimensional representation of the left panel. The grey surface is the plane of significance at the 95% level, i.e. M_{95}. All points of the wavelet power spectrum that are at a greater CWT power (i.e. wavelet power or amplitude) than M_{95} are in the region S_{95}. For both panels, S were calculated using 1000 simulated light curves, consisting of a simple power law PSD (without the Lorentzian component present). Each subsequent wavelet power spectrum plot in this work uses the same generalized Morse wavelet parameters, and respective confidence levels for the 2-dimensional and 3-dimensional representations. The 'rms-squared' normalization (Uttley et al. 2014) was used for each PSD in this work.

2.3.2 Interpretation of the Wavelet Power Spectrum

One challenge of the wavelet analysis is that the wavelet power spectrum is a surface in 3-dimensions and might be more difficult to quantify than a Fourier transform. Not all features in the image are necessarily important or significant. Understanding how to interpret the results correctly, and identify artifacts that arise from either statistical fluctuations or from the nature of the wavelet transform itself, is paramount.

The wavelet power spectrum amplitudes are represented in 2-dimensions as a shade of red. In 3-dimensions these amplitudes are represented by both a height along an axis orthogonal to the (t, f) plane, as well as the same shade of red used in the 2-dimensional representation. Due to long tails in the distribution of wavelet power spectrum amplitudes across the entire (t, f) space and the visual limitations of using a colour to plot information, the entire range of wavelet power amplitudes are not represented equally. The "maximum" colour was cut off at the 97.5^{th} percentile, so any amplitude at or greater than that percentile shows up as the darkest shade of red, and/or the highest height. Similarly, the "minimum" percentile was cut off at the 0.1 percentile.

It is important to note that the wavelet power spectrum amplitudes (i.e. the colour of red) are relative in each spectrum. One wavelet power spectrum can not be directly compared to another because the colours and amplitudes will be different.

2.3.2.1 Cone of Influence

The finite length of the light curves implies that not all frequencies can be examined with significance at any given time. From the onset of the observation, higher frequencies can be examined at earlier times than lower frequencies. As the observation trails off, again the examination of lower frequencies will have to be concluded prior to study of the higher frequencies. This produces a so-called cone of influence (COI) in the time–frequency space of the wavelet power

spectrum, which corresponds to a region where the data can be best studied (Fig. 2.1 or any other figure).

There is no precise mathematical definition for the COI, which depends on the choice of wavelet basis vector.[2] In the case of the generalized Morse wavelet, the COI definition also depends on the parameters P and γ. In the MATLAB WAVELET TOOLBOX implementation of the generalized Morse wavelet with an input time series, the COI is defined as a function of frequency and calculated as (Misiti et al. 1996):

$$\mathrm{COI}(f) = \frac{f_c \sigma_{t,\psi}}{2\pi S dt}. \tag{2.6}$$

Here, f_c is the central frequency of the generalized Morse wavelet, which is a function of P and γ. The time series bin width is dt and S is a vector called "samples" which is a function of the time series length N. Each element of S takes on an integer value, starting at 1, stepping to $N/2$ at the halfway point, and then stepping back down to 1. For an even N, S takes on the values:

$$S = (1, 2, ..., N/2, N/2, ..., 2, 1), \tag{2.7}$$

and for an odd N:

$$S = (1, 2, ..., (N+1)/2, ..., 2, 1). \tag{2.8}$$

The wavelet standard deviation is defined in Lilly & Olhede (2008) as:

[2]For detailed descriptions and definitions of the COI, see Torrence & Compo (1998), Nobach et al. (2007), and Lilly (2017).

$$\sigma_{t,\psi} = f_c \frac{\int |\Psi'(f)|^2 df}{\int |\Psi(f)|^2 df} \tag{2.9}$$

where $\Psi(f)$ is the wavelet basis vector projected to the frequency domain and $\Psi'(f) = d\Psi/df$. For the generalized Morse wavelet, this is:

$$\Psi_{P,\gamma}(f) = a_{P,\gamma} f^{\frac{P^2}{\gamma}} e^{-\gamma f}. \tag{2.10}$$

When plotting the COI of the wavelet power spectrum as an image projected to 2-dimensional time–frequency space, the regions below the COI are shaded as a reminder to treat any apparent wavelet peaks in that region with skepticism, as they could be due to the boundary effects which arise from the finite time series length (e.g. Fig. 2.3). The frequency at which the Poisson noise begins to dominate is calculated using the Poisson noise power as defined in Uttley et al. (2014). The region above the Poisson noise level is also shaded to indicate that it is dominated by noise.

When plotting the wavelet power spectrum as a surface in 3-dimensional time–frequency–amplitude space, the regions below the COI and in the Poisson noise are fully subtracted to zero (e.g. Fig. 2.1). This is simply done to improve clarity.

2.3.2.2 Confidence Intervals

An important aspect of the wavelet power spectrum, is to determine intervals in the time–frequency space where the amplitudes of the wavelet power spectrum are significant. In Torrence & Compo (1998), a method is outlined to estimate the significant regions, for Gaussian distributed time series which follow a red-noise distribution. Since AGN light curves typically have log-normal, or generally non-Gaussian flux distributions, a Monte Carlo process is adopted

in this work to estimate the significant regions.

The significant regions $S_\alpha(t,f) \in W(t,f)$, where α is the confidence level, were calculated using light curve simulations described in Section 2.3.1. First, an ensemble of light curves $x_{ensemble}(t)$ mimicking each observation were simulated. Here, each ensemble consisted of 1000 light curves. The input parameters for these simulations were: the observed flux distribution; the PSD slope based on a simple power law fit to the observed binned PSD; the number of data points; and the light curve duration. From this information, an ensemble of wavelet power spectra $W_{ensemble}(t,f)$ were calculated from the simulated light curves. From $W_{ensemble}(t,f)$ and a desired confidence level α, the α^{th} percentile can be calculated at each (t_i, f_i). This set of points forms a "plane of significance" $M_\alpha(t,f)$ in the 3-dimensional plot (right panel of Fig. 2.1), and the significant region S_α consists of all the points $W > M_\alpha$. The derived confidence contours and intervals are shown in Fig. 2.1 for a simulated time series.

2.3.3 Simulation Tests

A variety of simulations are carried out to determine the effectiveness of distinguishing and identifying (periodic) signals in AGN light curves. Here we examine light curves with different power distributions, periodic signals, and with non-stationary behaviour to better understand the appearance of the wavelet power spectrum.

2.3.3.1 Different Colours of Noise

Light curves with power spectra in the form of $f^{-\beta}$ are examined to visualize the effect of different values of β on the wavelet image. AGN commonly have $\beta \sim 2$ (red noise), but for simulation purposes β ranged from 0 (white noise) to 3 (black noise).

A simulation with $\beta = 2$ is already shown in Fig. 2.1. In Fig. 2.2, examples with $\beta = 0$ and $\beta = 3$ are displayed. There are no true (periodic) signals in either of these tests.

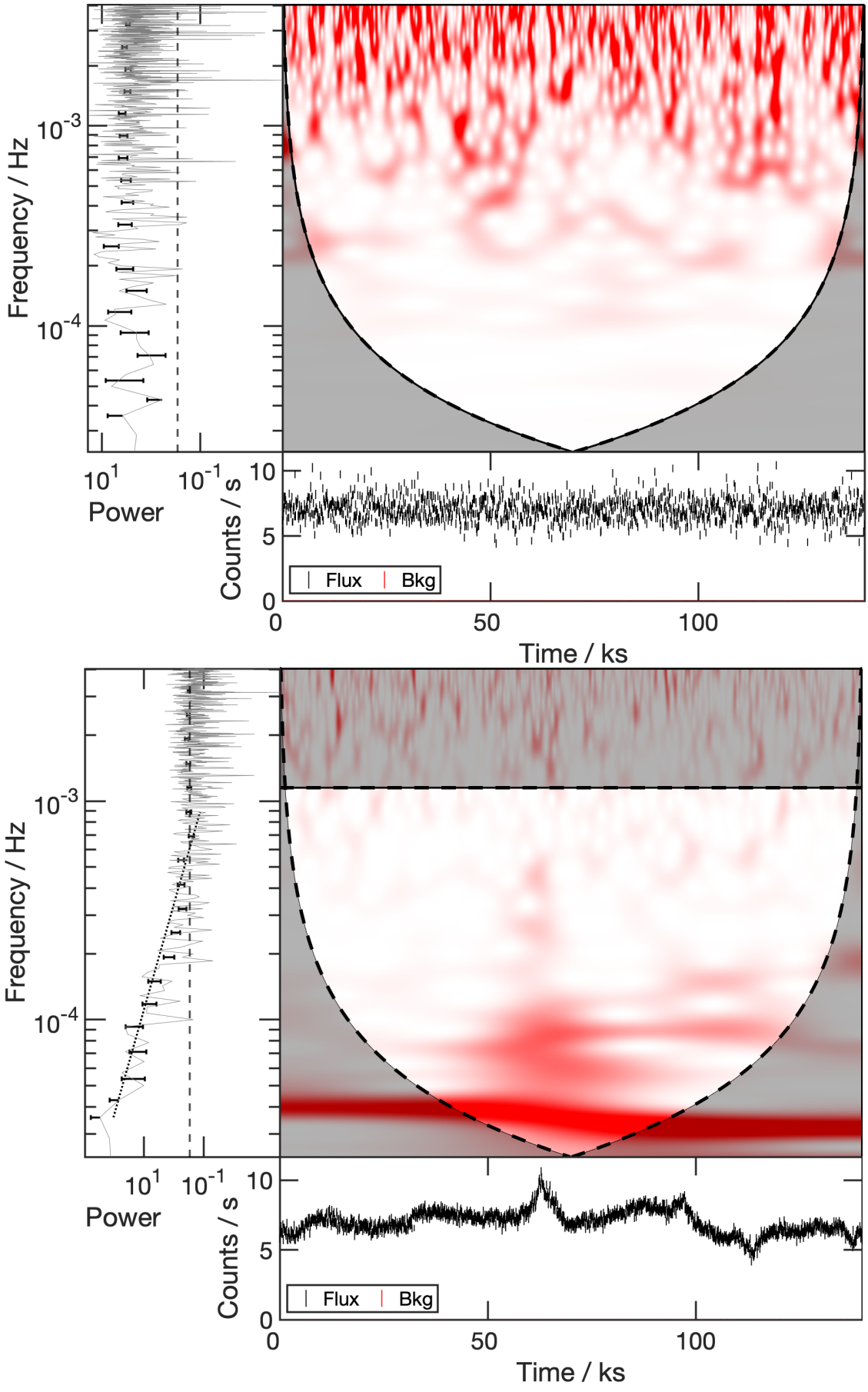

Figure 2.2: Wavelet power spectra of two simulated time series consisting of pure power law noise. As the time series are pure noise, no confidence levels are plotted. The light curves have input $\beta = 0$ (top panel) and $\beta = 3$ (lower panel) PSDs. An example with $\beta = 2$ was already shown in Fig. 2.1.

The random noise in the wavelet power does depend on index β. At $\beta = 0$, much of the random power is evident at high frequencies. As β is increased, the wavelet power amplitudes are skewed towards lower frequencies where the PSD has more power. This behaviour is largely expected, but highlights that signal detection may depend on the underlying power spectrum shape.

2.3.3.2 Different Types of Signals

The most basic pure component in a signal would be a perfect sine wave. The wavelet power spectrum of two sine waves is shown in Fig. 2.3 (top panel). Here it can be seen that since there is no variability in the frequencies present in the signal, a pure sine wave results in a constant band in the wavelet power spectrum.

In the lower panel of Fig. 2.3, the wavelet power spectrum for a single Lorentzian component is shown. Here it becomes evident that even though the signal is a persistent and single Lorentzian component, there is still variability in the overall amplitude of the signal since the Lorentzian does have some "width" to it. Based on the colours in the wavelet spectrum, the feature appears to fluctuate, despite the fact that it is persistent in the input PSD. Therefore, due to the random variability intrinsic to the Lorentzian profile, a persistent peak in the PSD may not be always appear constant with time in the wavelet power spectrum.

2.3.3.3 The effects of count rate and exposure for detecting periodic signals

Adjusting the average count rate by multiplying the time series by a constant will not change the relative wavelet amplitudes throughout the (t, f) space. The absolute amplitudes of both W and M will be affected, but this has no effect on the ability to detect a significant region. This is demonstrated in the wavelet power spectra in Fig. 2.4 showing that the overall scaling will not affect which (t, f) regions are significant, since both W and M scale identically. From this, we

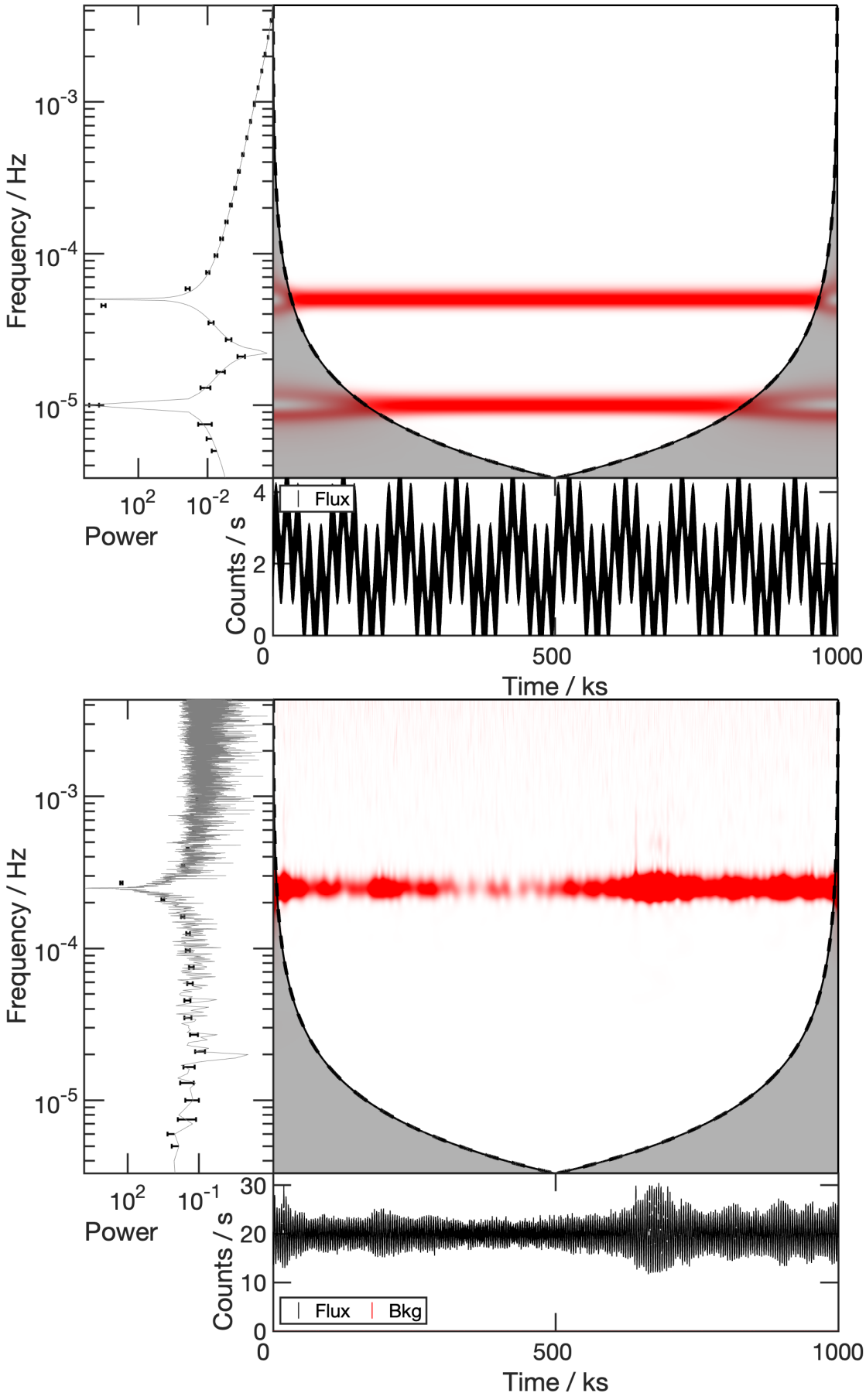

Figure 2.3: Top panel: The wavelet power spectrum of the function $f(t) = \sin(2\pi f_1 t) + \sin(2\pi f_2 t)$, where $f_1 = 10^{-5}$ Hz and $f_2 = 5 \times 10^{-5}$ Hz. Lower panel: A simulation of a time series consisting of a single Lorentzian profile at 2.5×10^{-4} Hz and with a full-width half-maximum of 2×10^{-5} Hz.

see that wavelet timing methods can be useful even for dim objects.

Another important aspect in X-ray observations is the exposure time needed to detect a feature in the light curve. This is shown in Fig. 2.5, where the wavelet power spectrum is calculated for a 20 ks and 200 ks light curve drawn from a long 1 Ms simulation. Here, we can see that a shorter exposure will limit the frequency range that can be examined significantly. As with the Fourier transform, repeated occurrences of a signal will improve the potential of detecting it with significance. With longer exposures, there is a stronger possibility of the signal being significant in the wavelet power spectrum.

2.3.3.4 The Effects of the PSD and Signal Strength

The input power spectra from the previous section are modified by including a Lorentzian profile at a given frequency to replicate a periodic signal. In Fig. 2.3, it is clearly demonstrated that a periodic signal is straightforward to detect with a wavelet power spectrum in the absence of noise. Fig. 2.6 shows that the underlying power law will affect which regions are significant in the wavelet power spectrum.

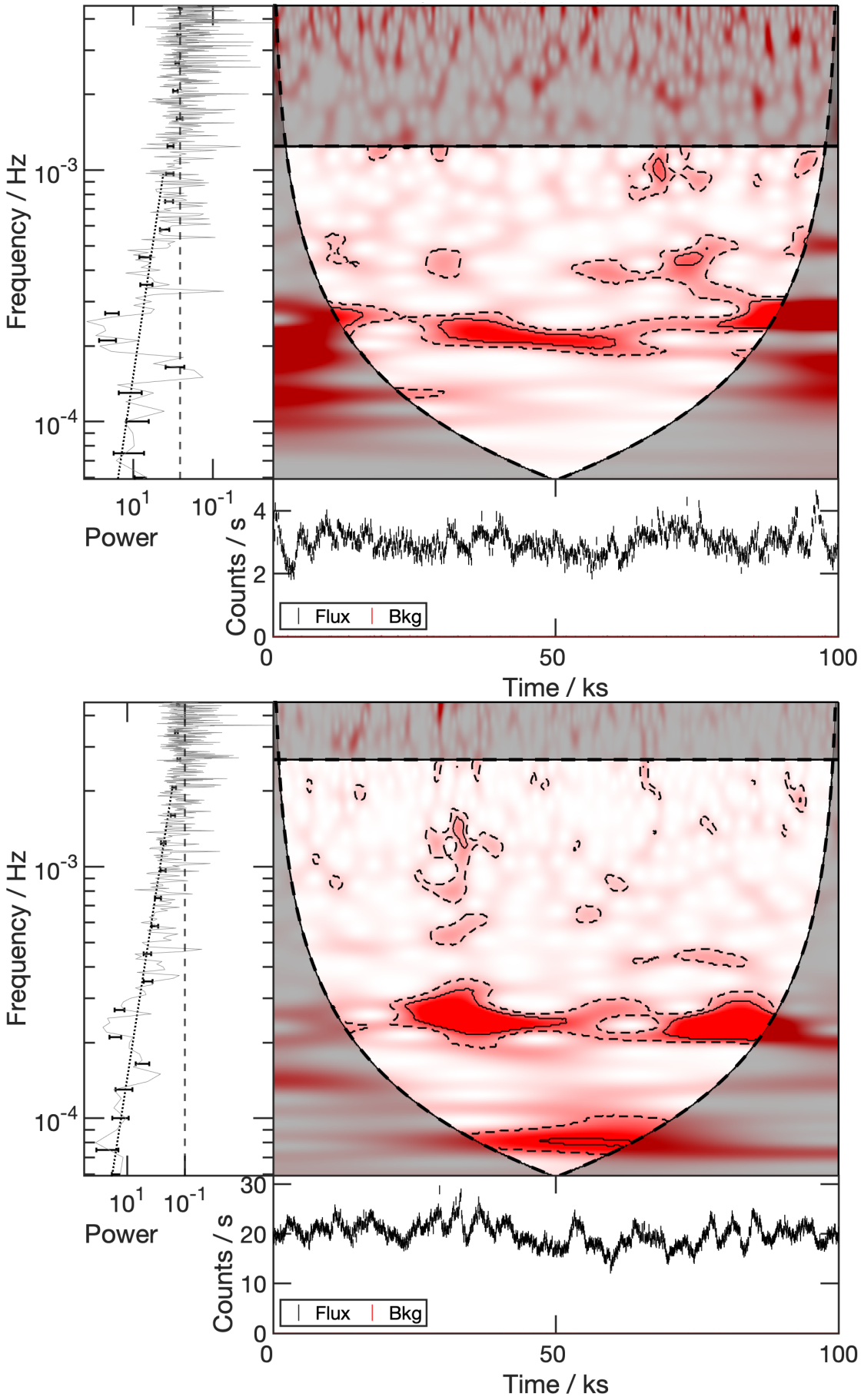

Figure 2.4: An example of two simulated time series consisting of identical input PSDs of a power law with $\beta = 1.7$ and a Lorentzian profile centered at 2.5×10^{-4} Hz. These differ only by average count rate (3 on top and 20 below).

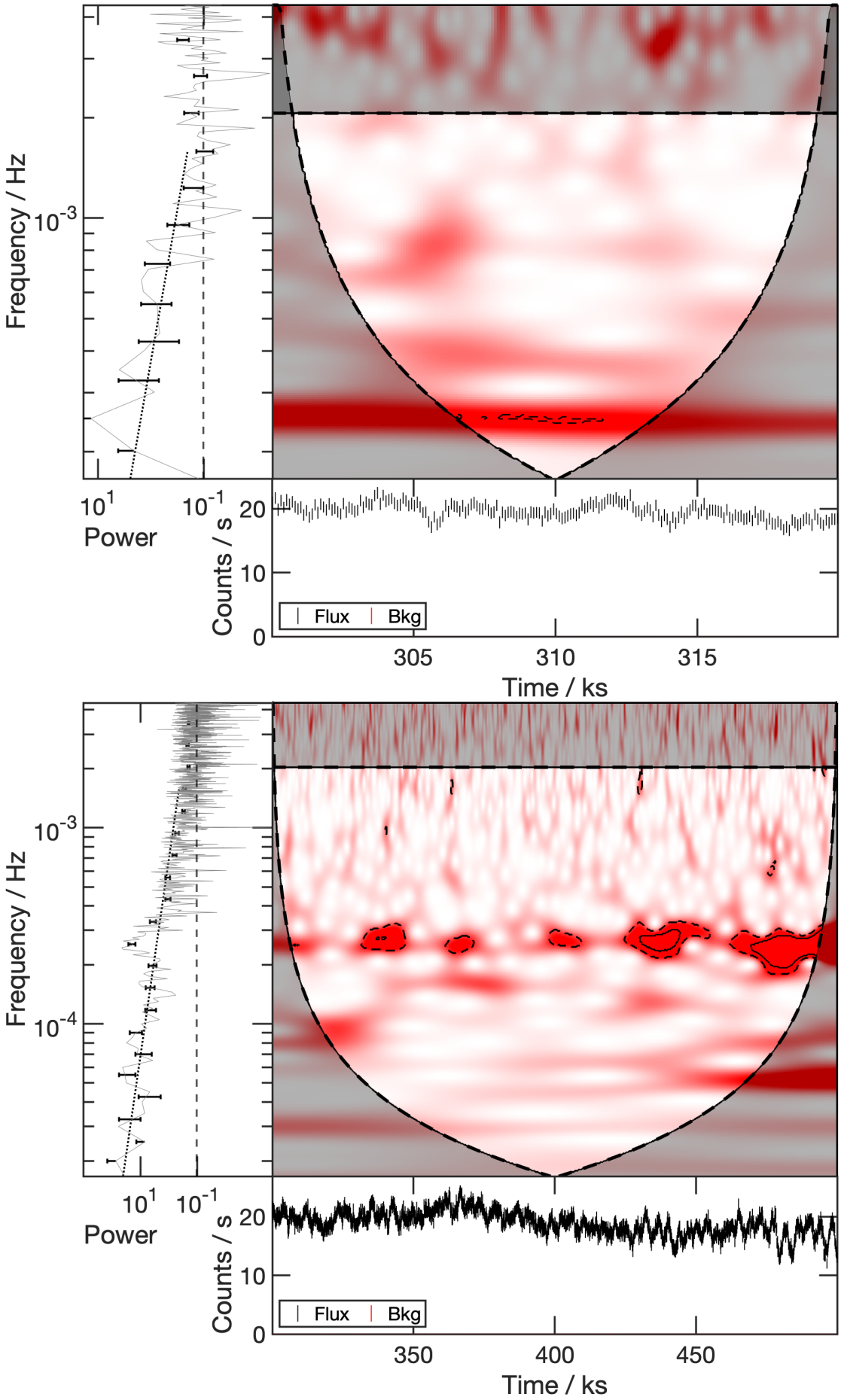

Figure 2.5: An example of two simulated time series that are each a subset from the same 1 Ms time series, consisting of a power law with $\beta = 1.7$ and a Lorentzian profile centered at 2.5×10^{-4} Hz. The top panel is 20 ks long, and the bottom panel is 200 ks long.

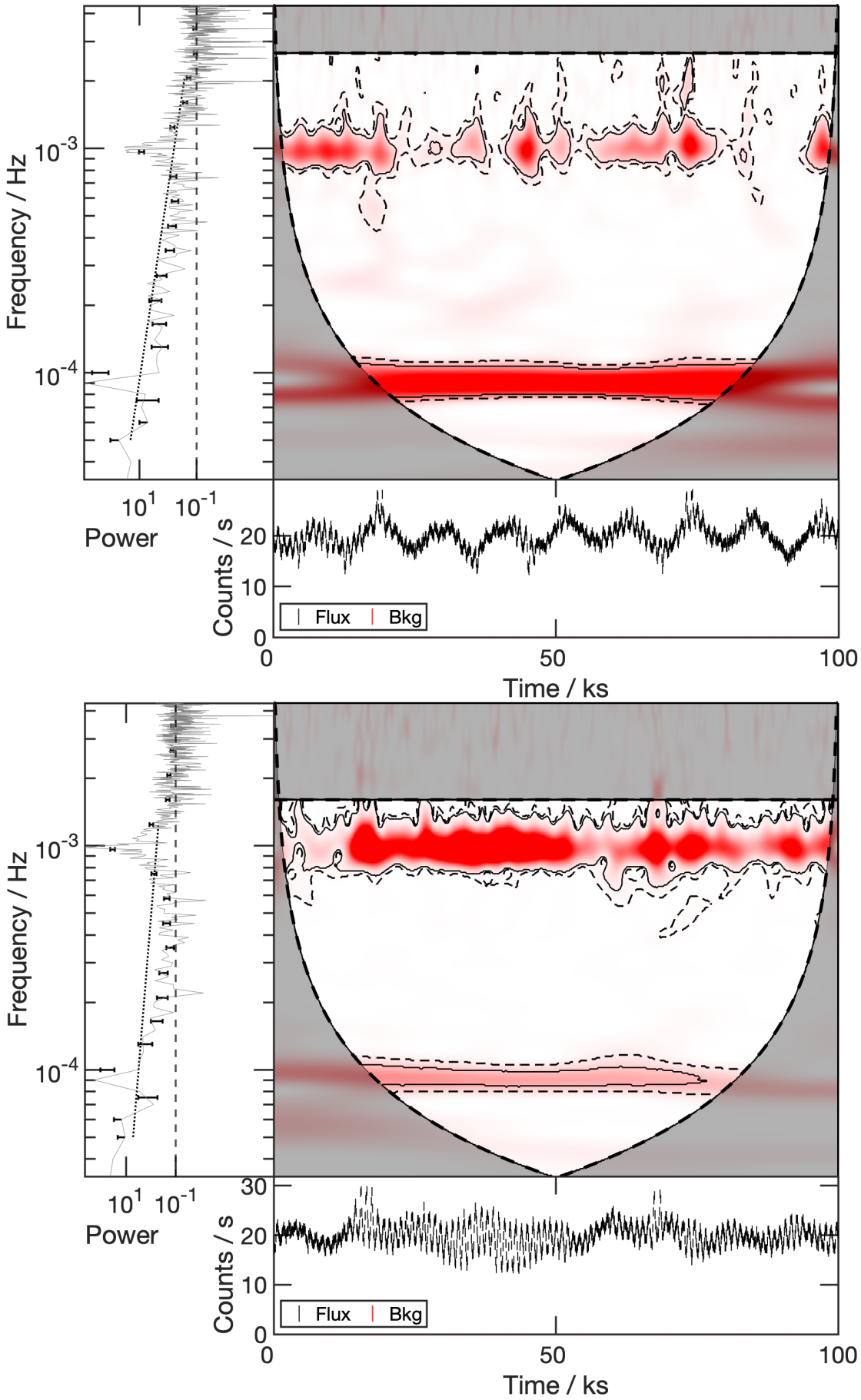

Figure 2.6: Wavelet power spectra of two simulated time series consisting of an underlying power law and two Lorentzian profiles centered at 10^{-4} Hz and 10^{-3} Hz. Top panel: The power law is $\beta = 2$, and the lower frequency Lorentzian appears to be more significant in the wavelet power spectrum. Bottom panel: The power law is $\beta = 3$, and the higher frequency Lorentzian appears to be more significant in the wavelet power spectrum.

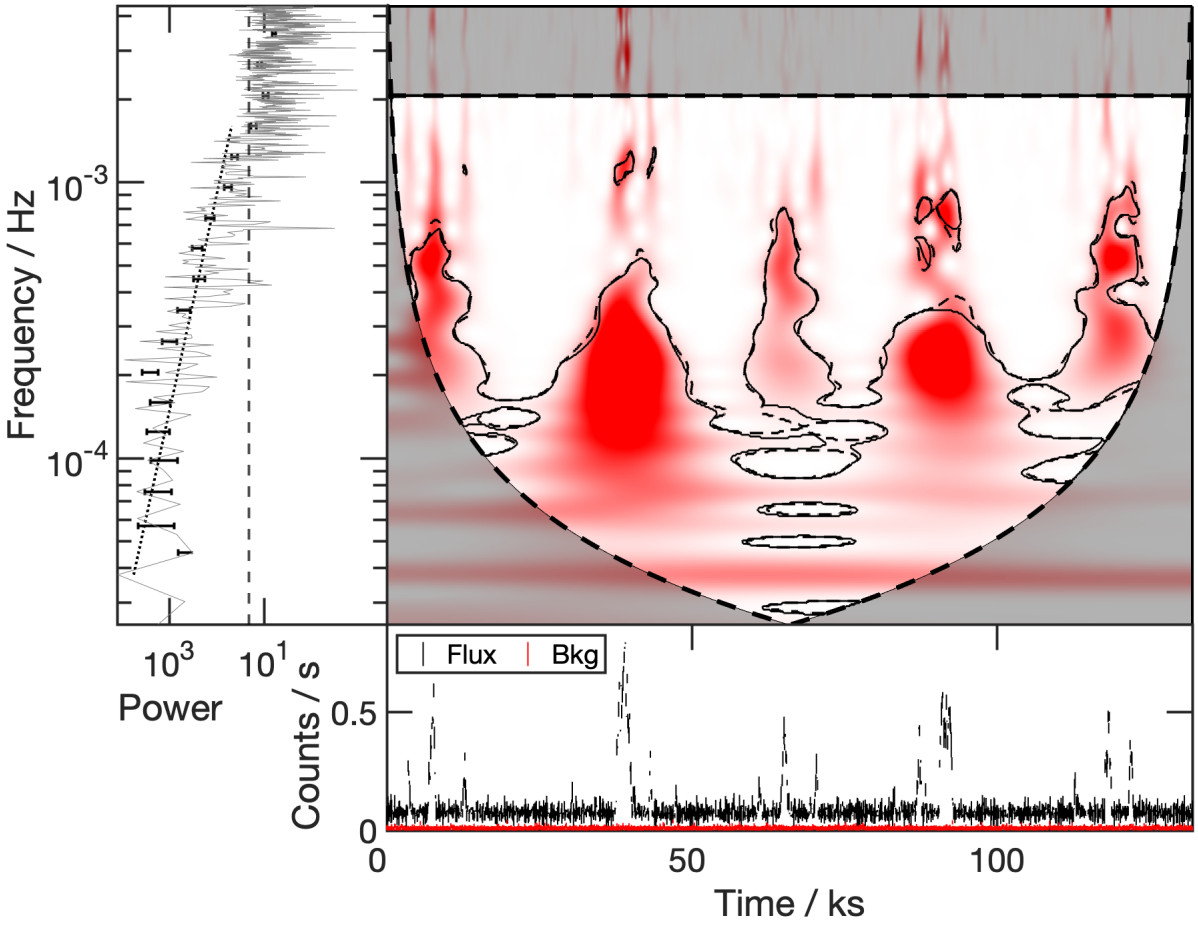

Figure 2.7: A simulated time series with a white noise PSD and consisting of ten Lorentzian components spaced in frequency and power.

In addition, we also examine the potential of identifying multiple periodic signals. For this, multiple Lorentzian profiles were added to PSDs with different slopes. Again, in the absence of noise, Fig. 2.3 demonstrates that multiple signals are easily distinguished. In Fig. 2.7, we examine an extreme case where ten Lorentzian profiles are added to an underlying white noise spectrum. The Lorentzian profiles are spaced in frequency to resemble harmonics of equal power. The frequencies are spaced by a geometric factor of 3/2, which is the harmonic spacing of QPOs in stellar mass X-ray binaries. The lowest frequency harmonic is $(9\ \mathrm{hr})^{-1} = 3 \times 10^{-5}$ Hz, which is the lowest harmonic present in the AGN GSN 069 (Miniutti et al. 2019). For this simulation, the harmonics all had equal power. Multiple features stand out as potentially interesting. In such a situation, it is challenging to accurately model the underlying power law,

as can be seen in fitted PSD in Fig. 2.7. With all the signals present and overlapping, the best-fit power law has $\beta = 1.26$, even though the input was $\beta = 0$. However, the wavelet spectrum clearly indicates that multiple frequencies might be important.

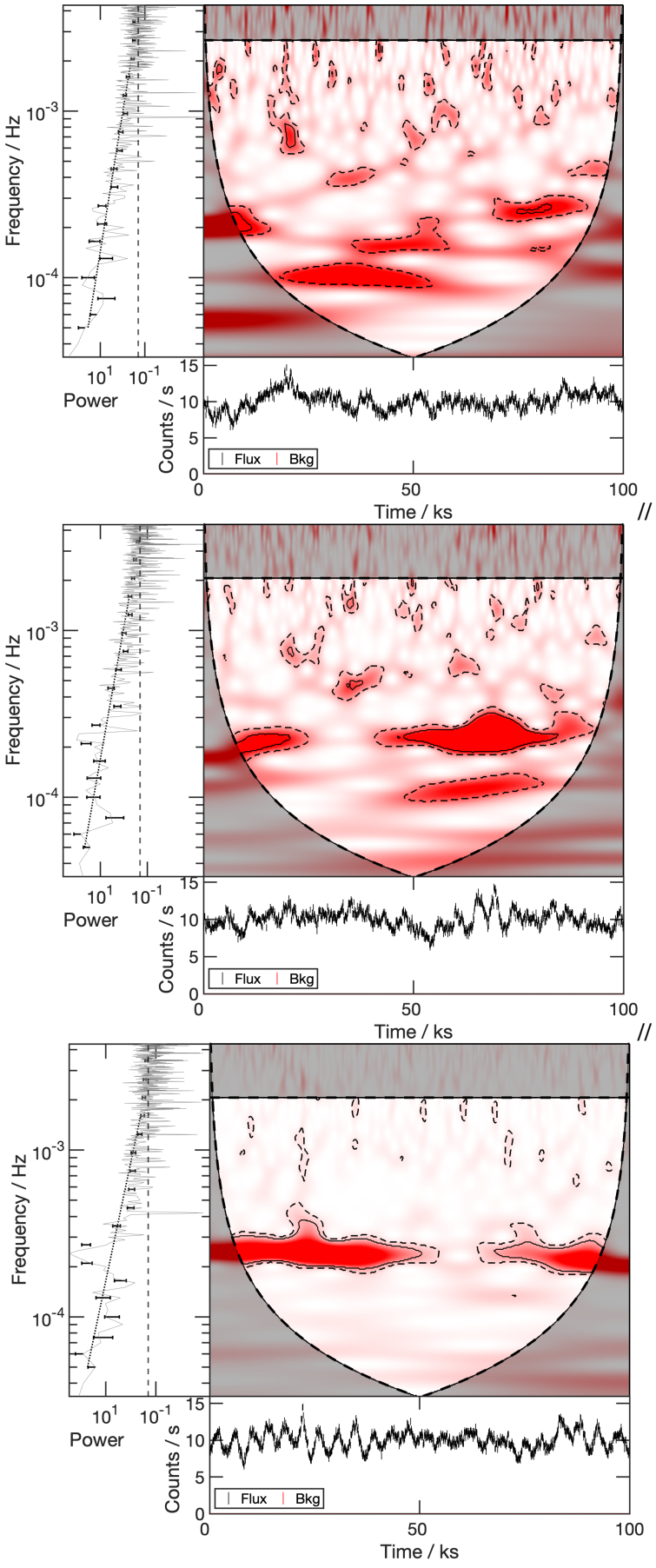

Figure 2.8: Simulated time series consisting of a Lorentzian component centered at 2.5×10^{-4} Hz, and a power law component with $\beta = 1.7$. The ratio of the Lorentzian/power law respective integrals are 1% (top panel), 10% (middle panel), and 100% (bottom panel).

We also examined the effect on the wavelet power spectrum of varying the ratio of power between the Lorentzian component and power law slope, by dividing the integral of the Lorentzian component by the integral of the power law component. In Fig. 2.8 it is apparent that when the Lorentzian component is very weak compared to the power law component, for example around 1% of the strength, it does not appear to be significant in the wavelet power spectrum despite being persistent. At 10% the Lorentzian component is significant but not fully persistent in the wavelet power spectrum. At 100% the Lorentzian component is significant, and fully persistent other than a small segment in the middle of the time series, due to the random variance of the Lorentzian strength as shown in Fig. 2.3. Note that for the *XMM-Newton* observation of RE J1034+396 (Obs ID: 0506440101), the Lorentzian to power law ratio was approximately 10%, and was fully persistent at the 90% confidence level in the wavelet power spectrum (see Section 2.4.3).

2.3.3.5 Non-stationary Signals

Non-stationarity was simulated by approximating the non-stationary time series as an ensemble of stationary light curves, i.e. a non-stationary piecewise PSD as suggested in Alston (2019). Different tests of non-stationary time series were completed, to see how the wavelet power spectrum coefficients change with time. Tests included:

- varying the overall PSD power
- varying the overall PSD power with a constant power and frequency Lorentzian
- varying the PSD slope β
- varying the Lorentzian power with constant frequency
- varying the Lorentzian frequency with constant power

- varying the PSD slope as a random flicker by sampling from a Gaussian distribution
- varying the PSD slope as a randomly increasing flicker by sampling from Gaussian distributions with increasing mean values

In Fig. 2.9, we show a test where we have a constant Lorentzian signal and an underlying PSD that is varying in slope. The power law slope increases from $\beta = 0$ to 3 linearly in 20 ks intervals while the Lorentzian profile remains constant at 2.5×10^{-4} Hz. The degree of variability is likely extreme compared to real sources.

Fitting the averaged PSD with a single power law is obviously incorrect but still allows us to examine the wavelet spectrum for significant features. A roughly persistent signal is present at the correct frequency, indicating that signals can examined even if the true underlying PSD slope is not well known.

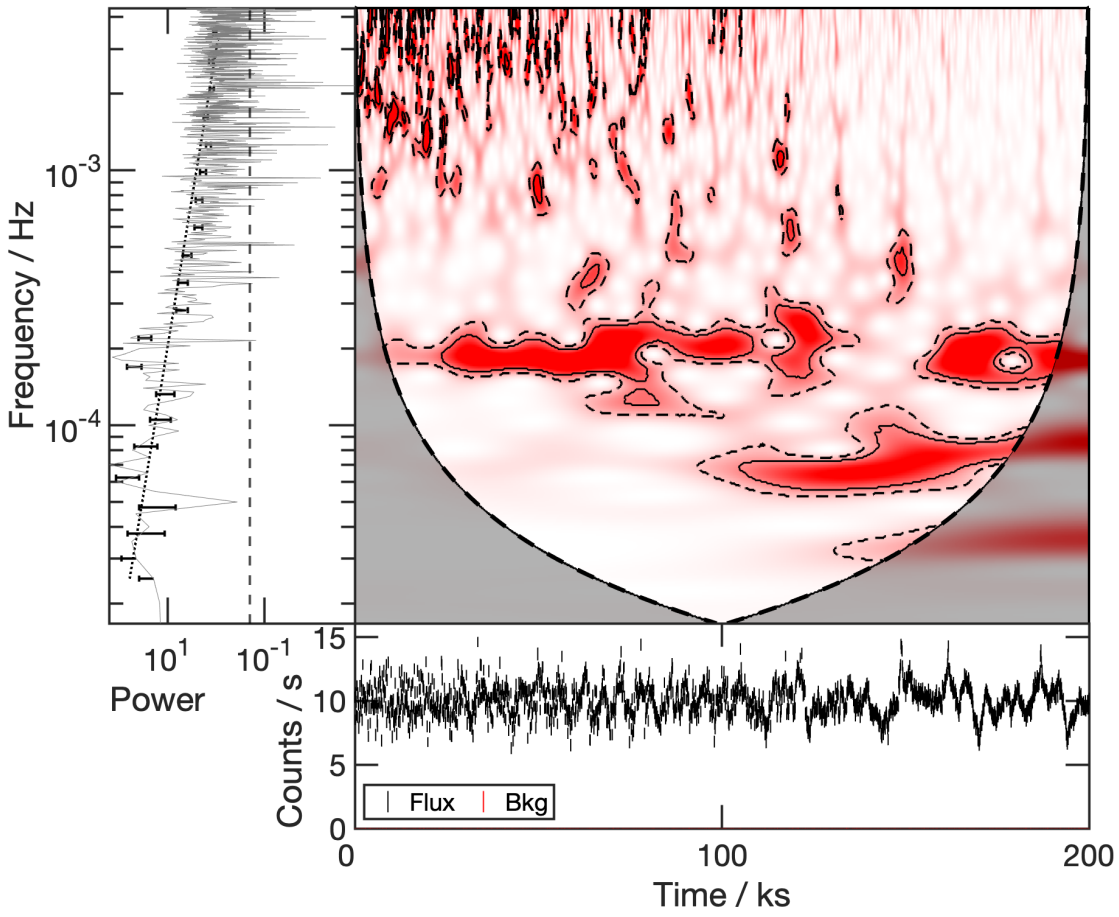

Figure 2.9: Simulation of a non-stationary time series, using a non-stationary piecewise PSD. The Lorentzian component is constant at 2.5×10^{-4} Hz throughout the entire light curve. The power law component varies from $\beta = 0$ to 3 linearly in 20 ks intervals. We can see that the Lorentzian component is still significant in the wavelet power spectrum, for different β values. We can also see a general shift in the noisy amplitudes in the wavelet power spectrum, from higher to lower frequencies as the power law becomes steeper.

2.4 Applications of Wavelets to AGN and QPE X-ray Light Curves

As a proof of concept, four AGN are used to examine the effectiveness of the wavelet analysis. All of the objects have been observed with *XMM-Newton* in the $0.3 - 10$ keV band, and their variability has been analysed with Fourier techniques or other methods.

We use archival data obtained from the *XMM-Newton* (Jansen et al. 2001) Science Archive (XSA) for these four AGN, one of which exhibits QPE behaviour, to examine the effectiveness of the wavelet analysis on a wide range of variability behaviour. We focus on data collected by

the EPIC pn (Strüder et al. 2001) detector, which were processed in the following way using the *XMM-Newton* Science Analysis System (SAS) version 20.0.0. From the *XMM-Newton* Observation Data Files (ODFs) of each observation (see following subsections for specific observation IDs), we created event lists with the EPPROC task. These event lists were filtered using the EVSELECT task with conditions PATTERN ≤ 4 and FLAG $= 0$ to extract only single and double events. Source counts were extracted from a circular region of radius $35''$ centred on the source position (obtained from the NASA/IPAC Extragalactic Database), and background counts were extracted from a nearby off-source circular region of radius $50''$. Light curves were then created using the EPICLCCORR task and were rebinned to 100 s. We note that mild to negligible background flaring is present in each observation, however, we chose not to filter out these segments of the light curves in order to preserve light curve continuity. The effect of background flaring in the wavelet analysis is discussed, where applicable. Finally, we note that only RE J1034+396 exhibited significant photon pile-up (evaluated using the EPATPLOT task), with ~ 10 per cent in single and ~ 30 per cent in double events over the $0.5 - 2$ keV band; all other sources had < 5 per cent and < 10 per cent pile-up in single and double events, respectively. Since here we investigate only broad band light curves such levels of pile-up should not significantly impact the interpretation of our results, and therefore we perform all forthcoming analysis on the uncorrected light curves.

Since we are outlining a preliminary method for using wavelet transforms, in general, the objects selected exhibit distinct behaviour from each other. Here, we use the methods outlined above to produce wavelet power spectra and identify significant features. The results are then compared to the simulations in Section 2.3.3 and previous literature results.

2.4.1 Ark 120

An observation of the 'bare' Seyfert 1 galaxy Ark 120 ($z = 0.03271$) (Matt et al. 2014) (Obs ID: 0147190101) is examined in the $0.3 - 10$ keV energy band. The X-ray spectrum of Ark 120 is unremarkable, exhibiting a smooth soft excess above a harder power law, and a narrow Fe Kα emission line (Nardini et al. 2011, Nandi et al. 2021). There is no observed warm absorber, hence it is labeled as 'bare'. The central black hole has a high mass of $(150 \pm 19) \times 10^6\, M_\odot$ (Peterson et al. 2004).

Ark 120 serves as a good control test for our wavelet analysis. The object is very bright ($\sim$ 30 counts per second), and shows low variability (lower panel of Fig. 2.10), compared to most other Seyfert 1s. This is consistent with work showing the excess variance, which is a measure of variability, is significantly (linearly) anti-correlated with black hole mass (Lu & Yu 2001).

The measured PSD is very flat ($\beta \approx 0.96$) at frequencies not dominated by the Poisson noise. In Fig. 2.10, the wavelet spectrum appears completely consistent with a flat noise spectrum (e.g. compare to top panel of Fig. 2.2) with no obvious frequencies of importance.

2.4.2 IRAS 13224-3809

IRAS 13224–3809 ($z = 0.066$) is a highly variable Narrow-Line Seyfert 1 (NLS1; e.g. Gallo 2018) active galaxy. This AGN is reported to have a maximum spinning black hole $a_* > 0.94$ (Jiang et al. 2018) and a black hole mass of $(1.9 \pm 0.2) \times 10^6\, M_\odot$ measured from X-ray reverberation (Alston et al. 2020). The low black hole mass is expected to be accompanied with high flux variability.

If Ark 120 is noted for its simplicity, then IRAS 13224-3809 exemplifies the opposite extreme. For decades, it has been recognized for its persistent, rapid, and high-amplitude variability (e.g. Boller et al. 1997; Dewangan et al. 2002; Gallo et al. 2004). Deep observations with *XMM-Newton* show the source possesses a strong reverberation lag at a frequency

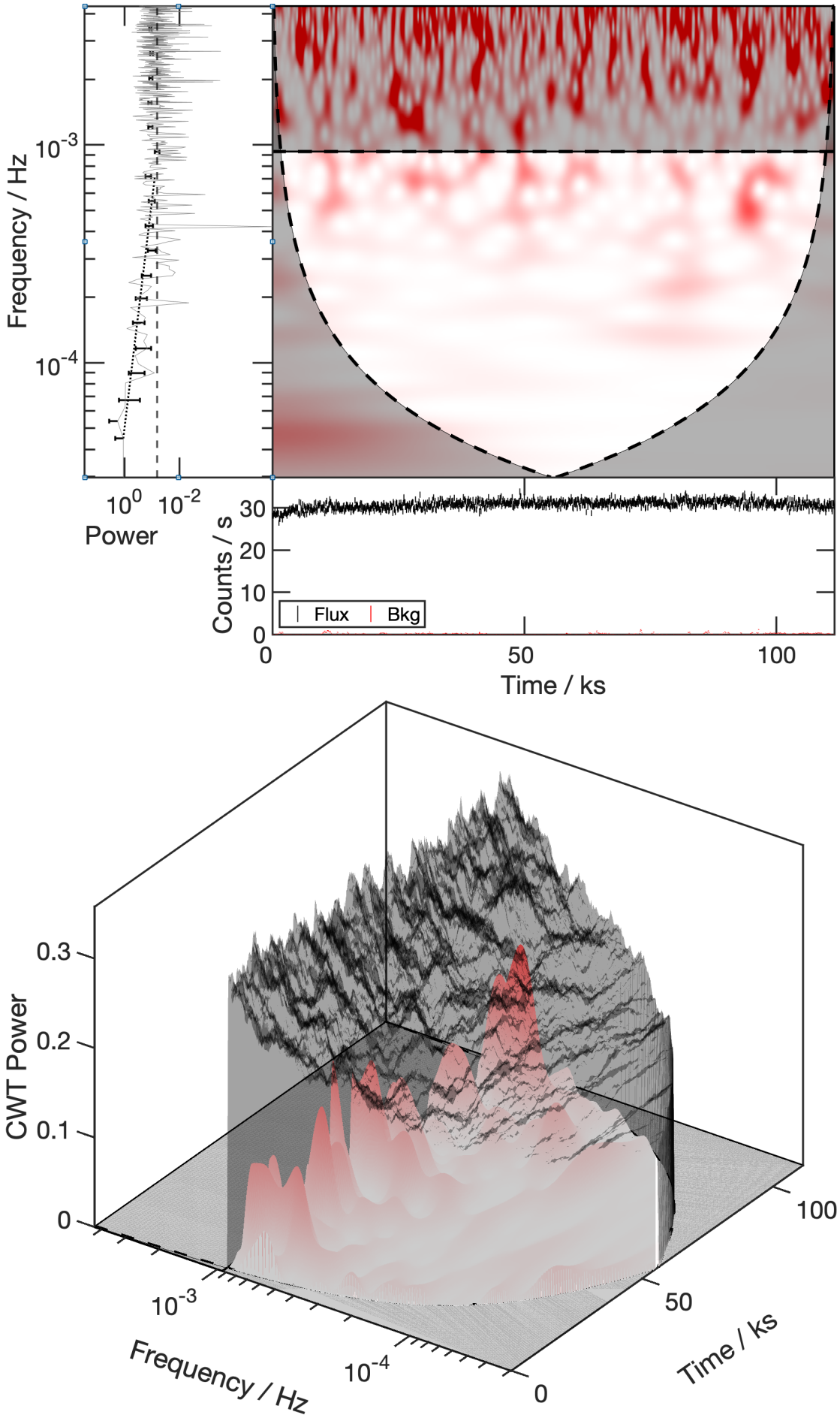

Figure 2.10: Left panel: The wavelet power spectrum of Ark 120 (Obs ID: 0147190101) appears similar to the white noise spectrum seen in Fig. 2.2. Right panel: The wavelet power shown in 3-dimensions emphasizing there are no significant features.

of $\sim 2 - 5 \times 10^{-4}$ Hz (e.g. Fabian et al. 2013, Kara et al. 2013). There is also evidence of a QPO at 7×10^{-4} Hz (Alston et al. 2019). In addition, there is evidence the AGN X-ray variability is non-stationary as IRAS 13224–3809 displays a time-dependent PSD, non-log-normal flux distribution, and a non-linear rms-flux relation (Alston et al. 2019).

With the exceptional amount of *XMM-Newton* data, IRAS 13224-3809 is an excellent target for a wavelet analysis. The AGN provides the opportunity to investigate non-stationary processes and the persistence of QPOs and reverberation lags. In this work, we examine only one observation (Obs ID: 0780561601) in the $0.3 - 5$ keV energy band, and leave analysis of all the data for future work.

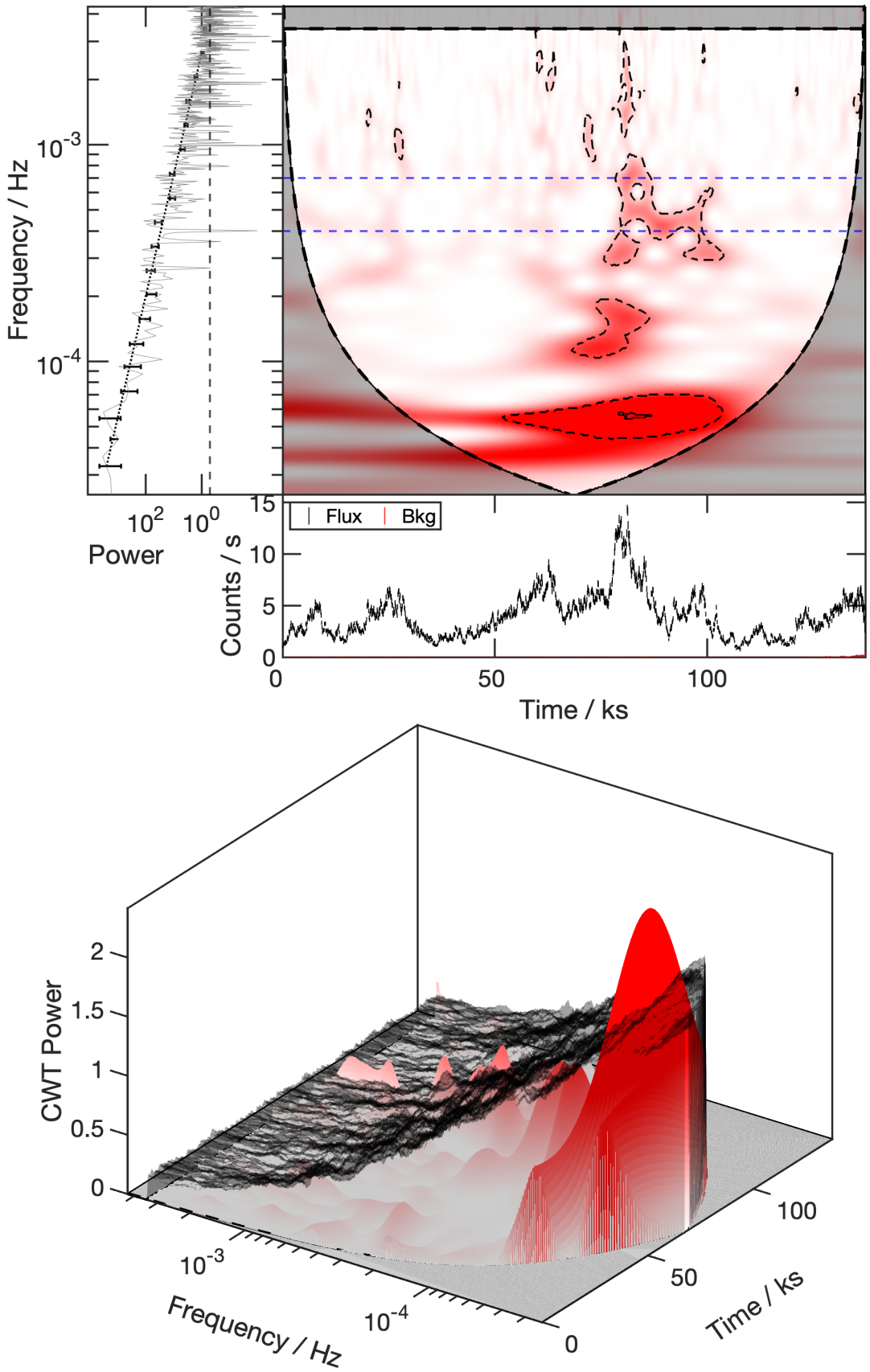

Figure 2.11: Wavelet power spectrum of IRAS 13224-3809 from revolution 3044 (Obs ID: 0780561601). Left panel: The higher frequency blue dashed line represents the QPO frequency at 7×10^{-4} Hz (Alston et al. 2019). The lower frequency blue dashed line represents the reverberation lag frequency at $\sim 4 \times 10^{-4}$ Hz (Kara et al. 2013). Right panel: The amplitude peak coincides with the flare in the light curve. It is also apparent that for a steeper red noise PSD such as this one, that the plane of significance is also steep with respect to the frequency axis. Thus, amplitudes at lower frequencies must be much greater to be significant.

The wavelet power spectrum for IRAS 13224-3809 in Fig. 2.11 is dominated by power at lower frequencies, less than $\sim 10^{-4}$ Hz. In addition, during a flaring event at ~ 75 ks, the wavelet power increases at all frequencies. In Section 2.3.3.1, we found that as β increases, the wavelet amplitude increases toward lower frequencies. This observation of IRAS 13224-3809 was measured to have $\beta = 1.8$ and we can make comparisons with the steeper noise spectrum seen in Fig. 2.2. Moreover, in the noise simulation in Fig. 2.2, we note that flares in the count rate can increase the wavelet power at all frequencies. Looking specifically at the frequencies associated with the reverberation lag ($\sim 2 - 5 \times 10^{-4}$ Hz) and the QPO (7×10^{-4} Hz), we note that the power at these frequencies is only significant during the flaring event at ~ 75 ks.

The wavelet spectrum of IRAS 13224-3809 is intriguing and motivates a deeper analysis of all the available data. The single observation we have examined here displays behaviour that is consistent with simple red-noise fluctuations. Analysis of all the available light curves would establish if there is some time or flux dependency for the QPO and reverberation signals.

2.4.3 RE J1034+396

QPOs are regularly observed in stellar-mass black holes (e.g. Remillard et al. 1999, Strohmayer 2001, Remillard et al. 2002, Remillard & McClintock 2006, Vaughan et al. 2011b), but the case is less robust in AGN. The best example of a QPO in an AGN is from observations of the NLS1 galaxy, RE J1034+396 ($z = 0.0424$) (Gierliński et al. 2008), which has an estimated mass of $\sim 2 \times 10^6 M_\odot$ (Middleton et al. 2009). Repeated observations of RE J1034+396 have confirmed the existence of the QPO, which appears to be caused by a dynamic structure in the inner disk (Jin et al. 2021). When present, the QPO occurs at $\sim 2.8 \times 10^{-4}$ Hz.

Examining the 2007 *XMM-Newton* observation (Obs ID: 0506440101) of RE J1034+396 in the $0.3 - 10$ keV energy band, which exhibited the strongest signal, finds the feature significantly detected in the wavelet power spectrum (Fig. 2.12). At the 90% confidence level it is persistent

across the entire observation, but the signal is more sporadic at the 99% confidence level. The signal compared to the 95% confidence level is shown in the 3-dimensional representation (Fig. 2.12). This 3-dimensional representation accentuates the variability of the QPO signal in the light curve.

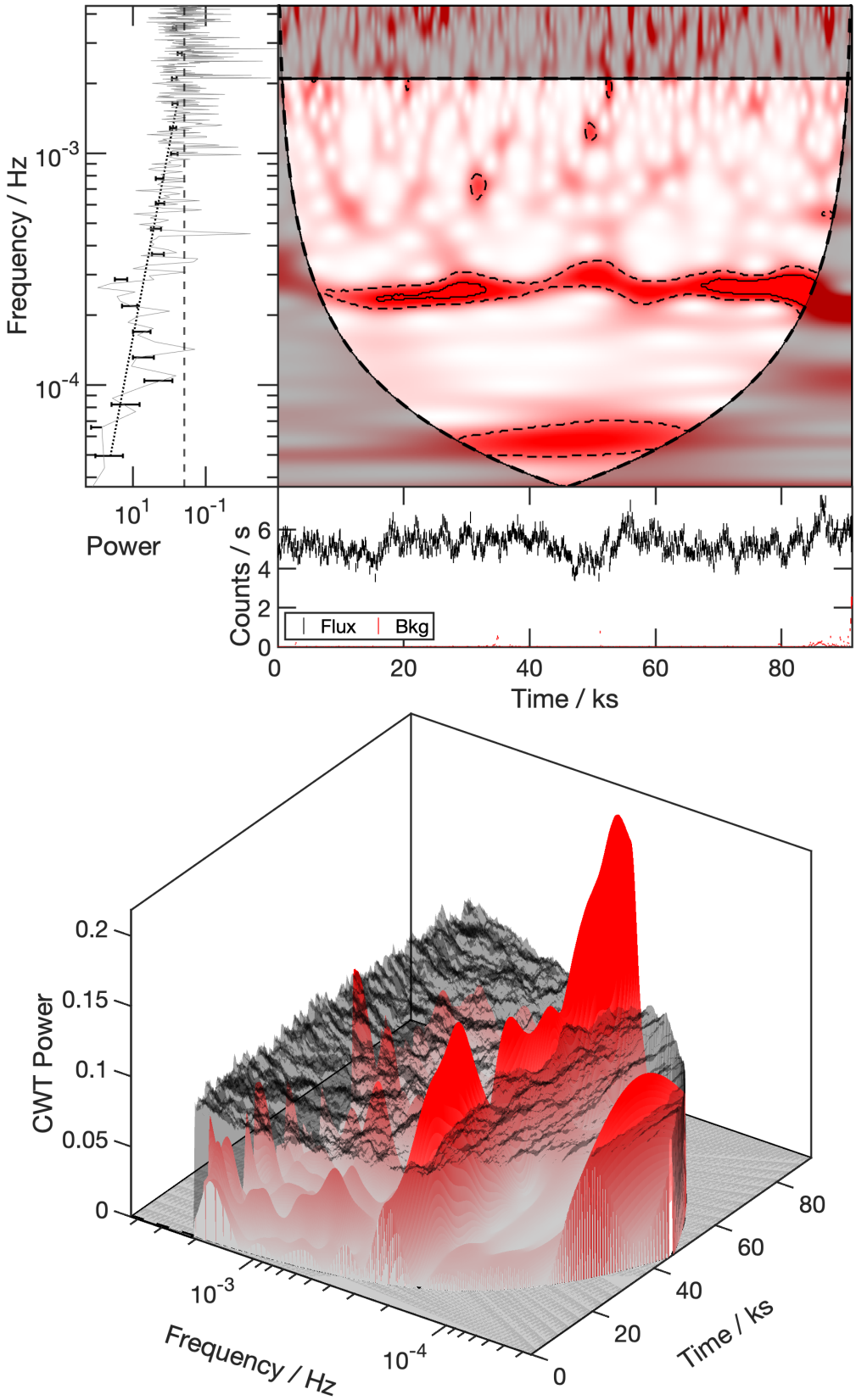

Figure 2.12: Wavelet power spectrum of RE J1034+396 (Obs ID: 0506440101). The strong, persistent QPO (e.g. Jin et al. 2020, Jin et al. 2021) is apparent here. Left panel: It is apparent that the QPO is fully persistent and significant at the 90% confidence level. It is not fully persistent at the 99% confidence level. Right panel: We can see that the QPO is almost fully persistent at the 95% confidence level. This 3-dimensional representation accentuates the variability of the Lorentzian component. There is also a significant frequency component at $\sim 6 \times 10^{-5}$ Hz, which is likely due to the underlying red noise.

The fluctuating significance of the feature does not necessarily indicate the signal is variable. As seen in Section 2.3.3, the significance of a constant feature can fluctuate in a red noise spectrum or if the underlying noise is non-stationary (Fig. 2.9). In addition, if the physical signal resembles a Lorentzian profile with some width in frequency, it can also exhibit fluctuations in wavelet power (Fig. 2.3).

There is also a feature at the 90% confidence level at $\sim 6 \times 10^{-5}$ Hz. As in Fig. 2.2, such a feature could be attributed to the steep underlying power spectrum ($\beta = 1.2$) in RE J1034+396.

2.4.4 GSN 069

GSN 069 ($z = 0.018$) was the first galaxy discovered to show QPEs in its X-ray flux (Miniutti et al. 2019). These eruptions are short-lived X-ray flares with a duration of approximately 1 hour occurring approximately every 9 hours. The QPEs are transient in GSN 069 (e.g. Miniutti et al. 2023) and several scenarios have been proposed to describe the behaviour, including unstable mass transfer occurring between a low mass star and the supermassive black hole (Lu & Quataert 2022), or instabilities in the inner accretion disk (Pan et al. 2022). The behaviour could be linked to a previous tidal disruption event (TDE) in the galaxy (e.g. Miniutti et al. 2019, Miniutti et al. 2023). The black hole mass has been estimated to be on the order of $10^5\, M_\odot$ (Miniutti et al. 2023).

The observation of GSN 069 used here is from May 2019 (Obs ID: 0851180401) in the $0.5 - 2$ keV energy band, and has an exposure of 132 ks. The wavelet power spectrum of GSN 069 might be the most unusual one we have examined here (Fig. 2.13). The wavelet power exhibits amplitude peaks across a range of frequencies during each of the eruption events in the light curve. However, there are also a number of persistent frequencies throughout the light curve.

Comparing the wavelet power spectrum to the simulations in Section 2.3.3, we note a strik-

ing resemblance with Fig. 2.7 that displays harmonic behaviour over a white noise spectrum. We can further examine the wavelet power by calculating the global wavelet transform (GWT) (Fig. 2.14), which effectively integrates the total power at each frequency over all times (as defined in Torrence & Compo 1998). There are five peaks that obviously coincide with the statistically significant contours in Fig. 2.13. These peaks are at frequencies of approximately 3.02, 6.04, 9.19, 12.62, and 20.62×10^{-5} Hz.

With the exception of the lowest frequency at 3.02×10^{-5} Hz, which is consistent with the 9 hour flaring period and is sampled for the least amount of time in the light curve (just at the bottom of the COI), the ratio between each subsequent higher frequency is approximately 1.5 (specifically $\sim 1.5, 1.4,$ and 1.6). The 3:2 ratio is coincident with what is observed in the QPOs of X-ray binaries.

However, we cannot rule out that this pattern is an artefact of the the underlying Fast Fourier Transform process present within the calculation of the CWT. Simulations have been done on an artificial signal consisting of a series of evenly spaced delta functions. The CWT was calculated on these signals, which also exhibited a similar pattern between the peaks of the GWT. When dividing the frequency of the $n^{th} + 1$ harmonic by the n^{th} harmonic, the ratios followed as 2/1, 3/2 and 4/3, after which the GWT was dominated by noise. The two latter ratios being slightly different for observations such GSN 069 could be due to the QPE peaks not being exactly evenly spaced, like with the delta function signal. For reference, the three lowest frequency ratios of the harmonics present in GSN 069 were 2.0, (3/2 + 0.02) and (4/3 + 0.04).

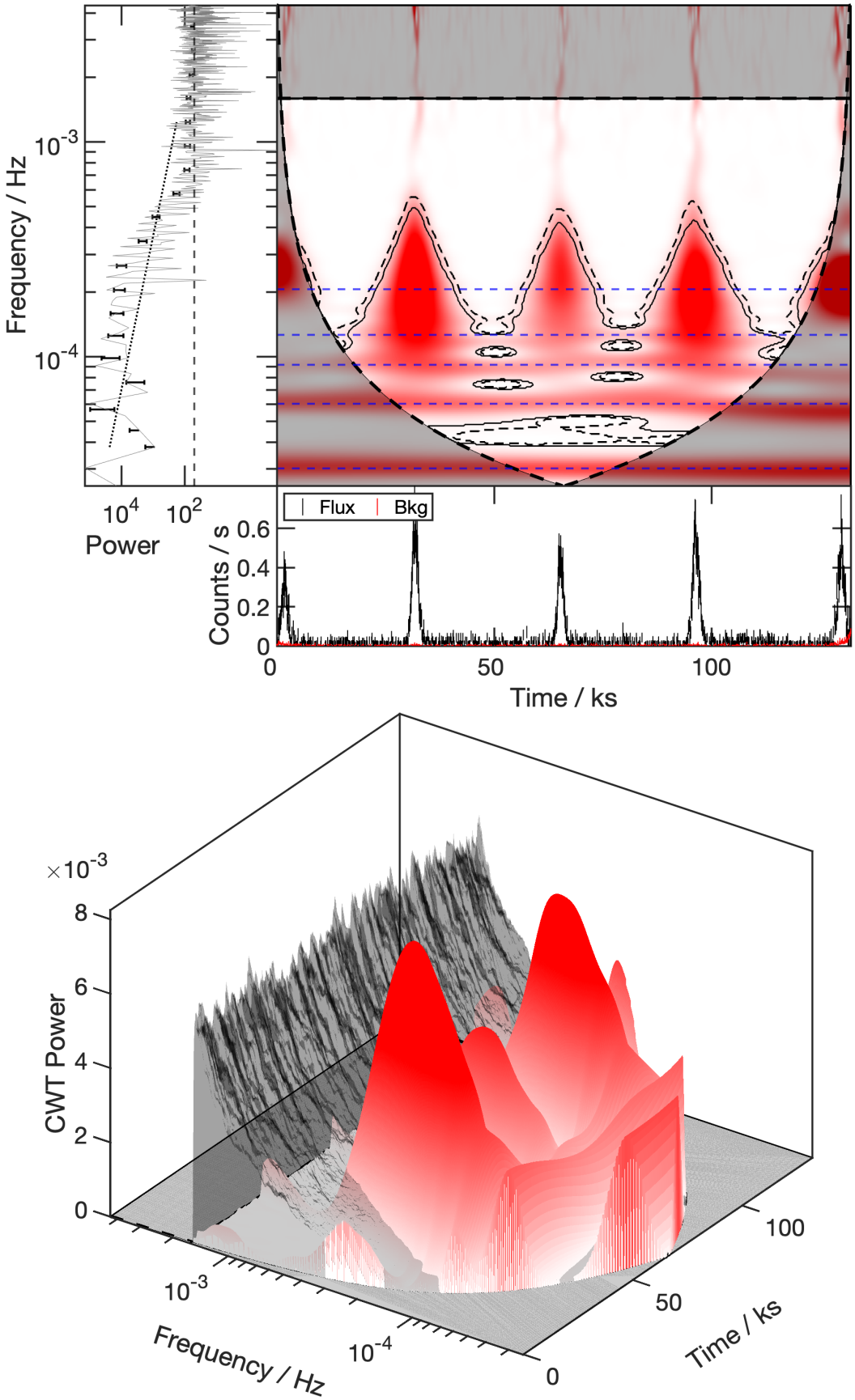

Figure 2.13: The wavelet power spectrum of GSN 069 (Obs ID: 0851180401). Left panel: The dashed blue lies represent the harmonics, which are taken to be the frequencies corresponding to peaks in the global wavelet power spectrum (Fig. 2.14. Right panel: The 3-dimensional representation emphasizes the amplitude peaks in the vicinity of the eruption events in this light curve.

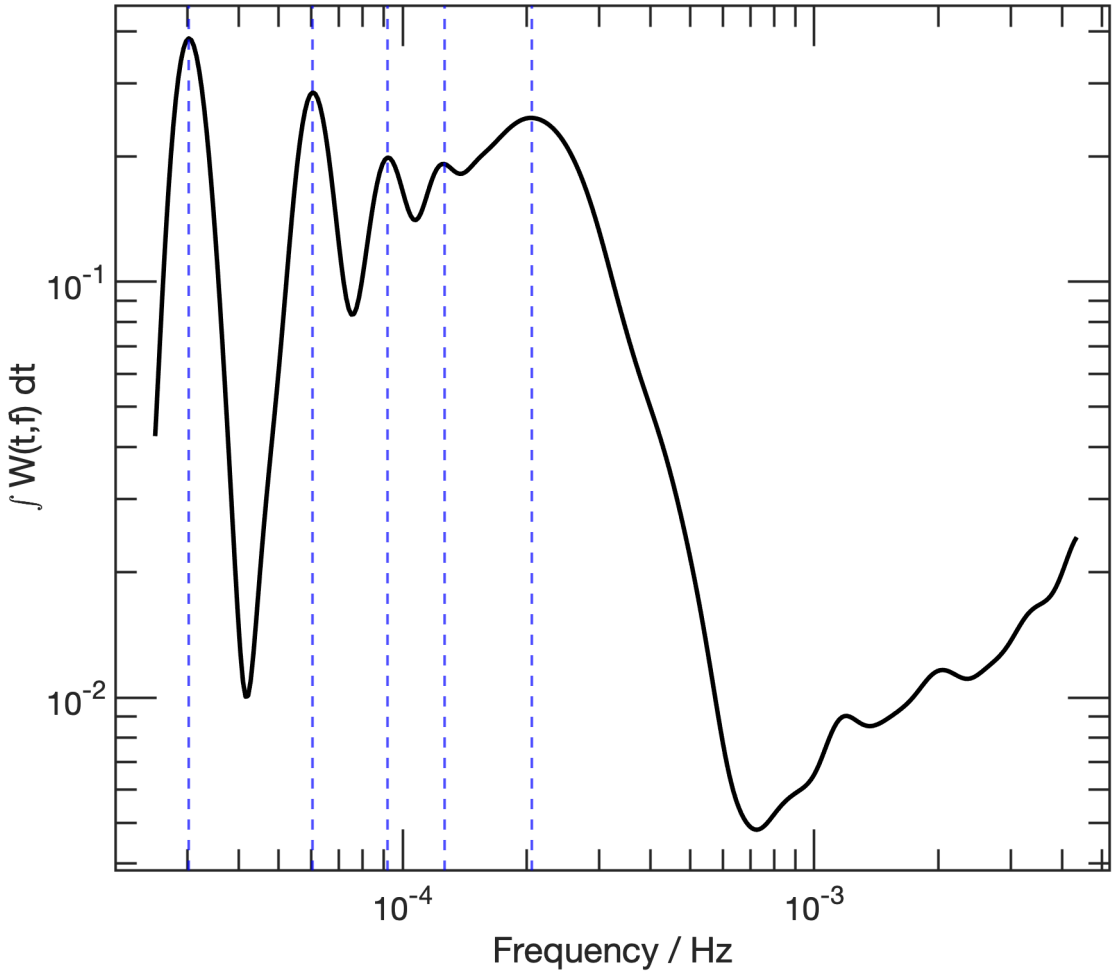

Figure 2.14: Global wavelet transform of GSN 069. The vertical lines highlight the frequencies where the wavelet power peaks. These will naturally coincide with the most significant regions in Fig. 2.13.

2.5 Discussion and Conclusions

With the understanding that the X-ray emission from AGN may be non-stationary, it is important to consider timing analysis tools that account for this. Fourier transforms which are widely used for analyzing AGN variability make the underlying assumption that the time series is stationary. The wavelet transform makes no such assumption. In addition, the wavelet transform preserves timing information while extracting the important frequencies in a series. In this work, we examine the application of the wavelet transform to the X-ray timing properties of AGN and QPEs.

Several simulations are carried out to test the effectiveness of the wavelet analysis for AGN light curves. The most basic was to examine the effects of different colours of underlying noise (i.e. different values of β for the PSD). As the slope increases, more noise will be introduced in the wavelet image at lower frequencies (Fig. 2.2). This needs to be considered for objects with steep PSDs like IRAS 13224-3809, which displays a persistent-looking feature at low frequencies (e.g. Fig. 2.11) that might simply be noise.

Since overall flux can vary significantly in AGN, we tested the effects of different average count rates and exposure lengths for wavelet analysis (e.g. Fig. 2.4). The main effect of the observation duration is the ability to explore lower frequencies and detect signals with higher significance. Obviously, the more often a frequency is observed in a light curve the more confidence there is in its importance.

The brightness of the AGN is less important at detecting signals in wavelets than the relative strength of the signal above the underlying PSD. A strong signal can be significantly detected at low count rates. It is obviously important that there is sufficient data to get a reasonable representation of the PSD and this is easier to achieve with bright objects (e.g. Fig. 2.8). Signals that exhibit a Lorentzian-to-power law ratio of $\sim 10\%$ can be robustly detected. The signal strength is comparable to that of the QPO in RE J1034+396.

The manner in which the periodic signal is modelled can also influence the appearance of the wavelet power spectrum. QPOs in AGN and X-ray binaries are often modelled with Lorentzian profiles. In this work we considered pure sine waves as well as Lorentzian profiles (Fig. 2.3). A sine function results in a persistent feature in the wavelet spectrum that is at constant power. The situation is more complicated with the Lorentzian profile as it possesses some natural width (i.e. range of frequencies). The power in the feature can appear to fluctuate with time in the wavelet spectrum even if it is persistent.

This is important to keep in mind when examining the time dependency of a periodic signal.

For example, the QPO in RE J1034+396 appears persistent over the duration of the observation, but its power appears to fluctuate. This might simply arise from the nature of the Lorentzian signal (Fig. 2.12).

In considering the variable nature of the Lorentzian profile we have touched on non-stationarity. As part of this examination, we looked at the effects of a variable PSD on the ability to detect signals (Fig. 2.9). We find that periodic signals can still be recovered when modelling the variable underlying PSD with an average value.

Wavelet power spectra were used to analyze an initial sample of four AGN, all exhibiting different behaviours from one another. For this work, the generalized Morse wavelet basis vector was used. By varying the time-bandwidth parameter, either the time-localized frequencies or persistent frequencies can be accentuated. For this work, the time-bandwidth parameter was held constant at the 60, which is provides moderate time and frequency resolution without preferring one over the other.

The wavelet power spectrum of Ark 120 was entirely consistent with noise. Given the large black hole mass and the low amplitude of variability, the result was expected.

IRAS 13224-3809 exhibits a steep red noise PSD. As stated, this will produce noise at lower frequencies in the wavelet. For the most part, there are no discerning features in the wavelet, except during a count rate flare at ~ 75 ks (Fig. 2.11). At that time, a number of frequencies are detected at > 90 per cent confidence. Interestingly, two of these frequencies correspond to the reverberation lag between $\sim 2 - 5 \times 10^{-4}$ Hz (e.g. Fabian et al. 2013; Kara et al. 2013; Alston et al. 2019) and the QPO at 7×10^{-4} Hz (Alston et al. 2019) previously reported in this object. This raises the possibility that these frequencies are time- and/or flux-dependent. However, with only the one observation examined here, we cannot rule out that the enhanced power at all frequencies during the flare is not simply a red noise characteristic. Analysis of the all the archival data of IRAS 13224-3809 will be important.

Examining the *XMM-Newton* observation of RE J1034+396 that exhibited the strongest QPO, we find the feature is significantly detected in the wavelet power spectrum (Fig. 2.12). At the 90% confidence level it is persistent across the entire observation, but the signal is more sporadic at the 99% confidence level. The fluctuations in the power of the QPO could be attributed to the Lorentzian nature of the signal.

GSN 069 possesses a unique wavelet power spectrum compared to the other sources examined, as it is a rare AGN that exhibits QPE phenomena in its light curves. There are several frequencies that are significantly detected. The primary frequency at $\sim 3 \times 10^{-5}$ Hz is coincident with the ~ 9 hour flares. However, there are higher frequencies detected with significance at 6.04, 9.19, 12.62, and 20.62×10^{-5} Hz. The ratio between these frequencies and each subsequent lower frequency is approximately 1.5 exhibiting a roughly 3:2 ratio that is similar with what is observed in the QPOs of X-ray binaries. This pattern cannot yet be rules out as being an artefact of the CWT calculation. The origins of QPOs is still uncertain, but this coincidence in the ratio of the oscillation frequencies draws direct comparison between supermassive and stellar mass black holes.

Wavelet analysis is a potentially powerful tool to study AGN X-ray light curves. It is complimentary to Fourier analysis and provides the potential to reveal signals that are transient in time or variable in power. Deeper analyses making use of multi-epoch data to examine transient features in the wavelet power spectrum of AGN, X-ray binaries and QPE sources will be important.

Chapter 3

The wavelet analysis of an eclisping X-ray event in NGC 6814

3.1 Introduction

NGC 6814 is a nearby (z = 0.00521) Seyfert 1.5 galaxy[1], which means that it is seen at relatively high angle through some fraction of the obscuring torus. Indeed, measurements of the inclination from the X-ray spectrum (Gallo et al. 2021) and the optical BLR (Rosenblatt et al. 1992) put it at about 60 degrees.

[1]For information on the AGN classification system and the AGN unification model, see Section 1.1.1.

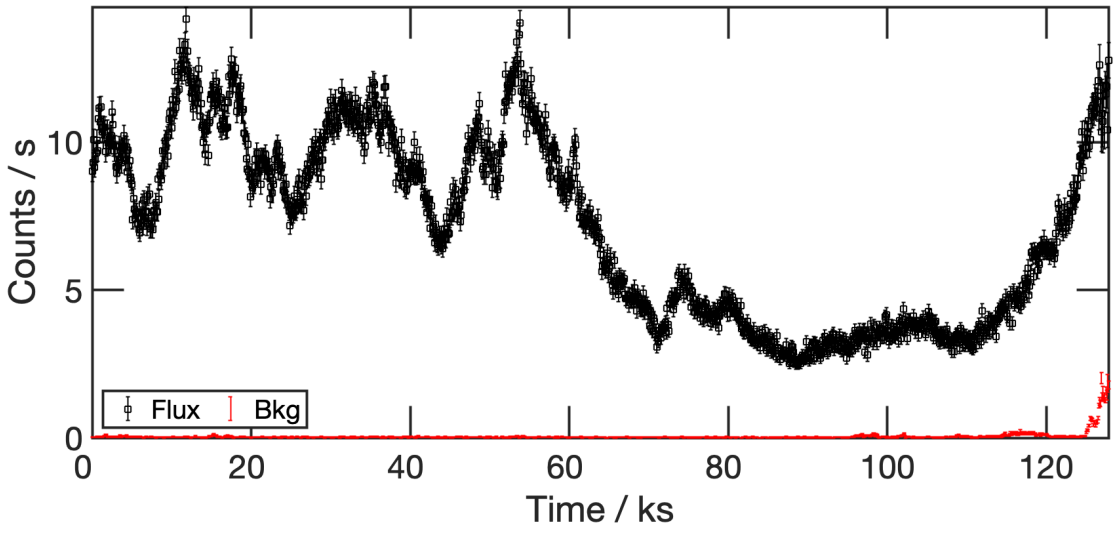

Figure 3.1: *XMM Newton* observation of NGC 6814, revolution 2991 (Obs ID: 0764620101) in the 0.3 - 10 keV band. The eclipse occurs between $\sim 55,\ 125$ ks. Note the rapid transition from pre-eclipse to eclipse (ingress), and eclipse to post-eclipse (egress).

NGC 6814 has also been observed to have a moderate amount of absorption in the X-ray band (Leighly et al. 1994). The X-ray spectrum is typical for a Seyfert 1.5 galaxy, showing a weak soft-excess below $\sim$ 1 keV and modest levels of absorption (Waddell & Gallo 2020). The X-ray band emission is rapidly variable on both short-term (hours) (Walton et al. 2013) and long-term (years) (Mukai et al. 2003) scales. Interestingly, in 2016 NGC 6814 underwent a rare, transient event as the X-ray emitting region was eclipsed by a dense, obscuring cloud (Gallo et al. 2021), (Fig. 3.1).

The eclipse starts at $\sim$ 60 ks in Fig. 3.1. Ingress lasts for approximately 15 ks, before reaching minimum for 40 ks. The duration of egress is identical to ingress (15 ks). The combination of spectral and timing analysis allowed Gallo et al. (2021) to use the eclipse to determine properties of the absorber and of the X-ray source. The size of the X-ray source is $\sim 25\ r_g$. The absorber is located at $r \sim 2694\ r_g = 4.34 \times 10^{15}$ cm and covers 80% of the source during the low flux state. It has a column density of 1.37×10^{23} cm^{-2} and ionisation parameter of $\log \xi/\text{erg cm}^{-2}\text{s}^{-1} = 1.09$ (Gallo et al. 2021).

In this chapter, we will examine the eclipsing event in NCG 6814 with the wavelet power

spectrum. To our knowledge, this is the first time wavelet analysis has been used to examine X-ray eclipses. We will also examine a later 2021 observation of NGC 6814 that did not exhibit an eclipse.

3.2 Analysis

We will examine two observations of NGC 6814 using archival data from the *XMM-Newton Science Archive* (Jansen et al. 2001). These light curves were processed using the *XMM-Newton* Science Analysis System (SAS) version 20.0.0 as in Section 2.4.

Both analyses use photons in the 0.3 - 10 keV energy band. The first observation (Obs ID: 0764620101) was in 2016 from April 8th at 4:59 AM to April 9th at 5:27 PM and contains the eclipsing event. The second observation (Obs ID: 0885090101) was in 2021 from October 1st at 1:11 PM to October 3rd at 10:47 PM and does not contain an eclipsing event. As in Sec. 2.4, the CWT was calculated for each of these observations.

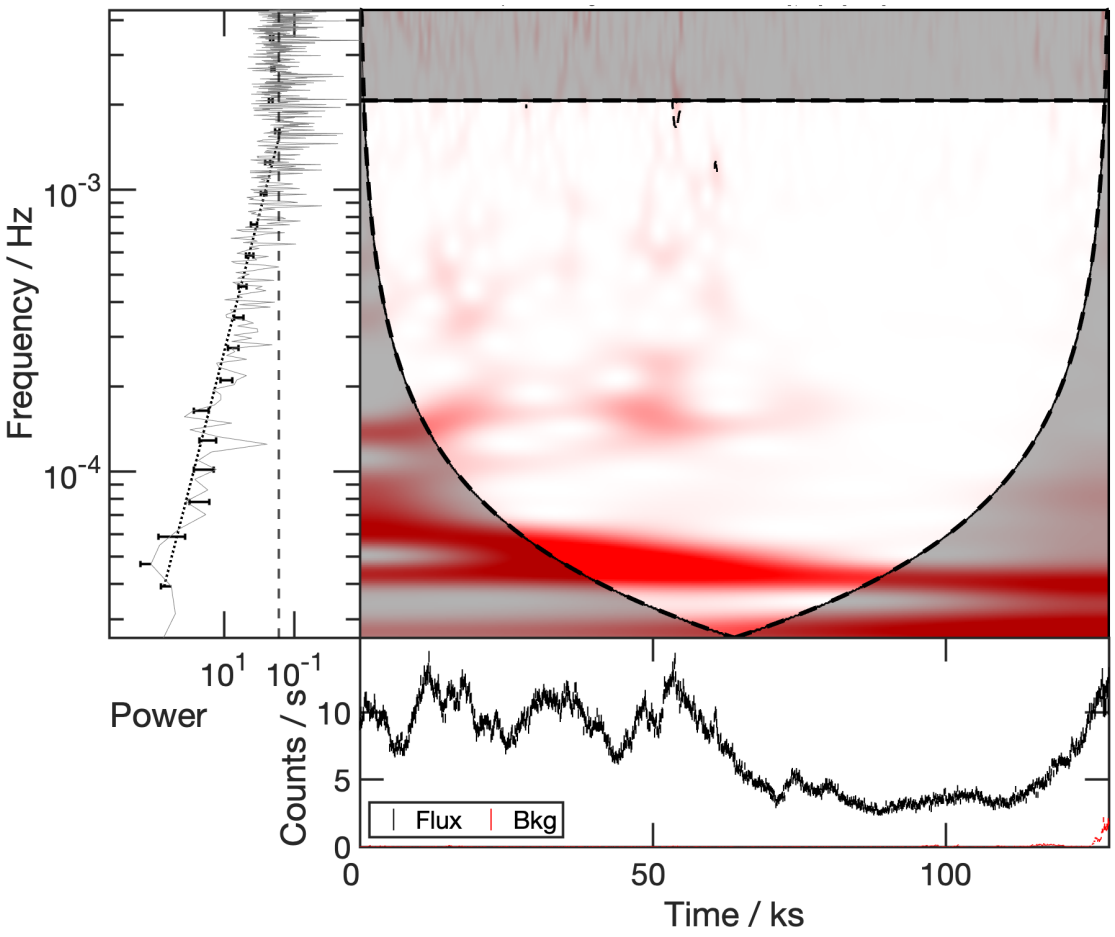

Figure 3.2: The generalized Morse wavelet of NGC 6814, revolution 2991 (Obs ID: 0764620101) in the 0.3 - 10 keV band. The generalized Morse wavelet parameters, cone of influence, and plane of significance contour lines are all as explained in Fig. 2.1.

The 2016 CWT is shown in Fig. 3.2. The only obvious feature is at $\sim 5 \times 10^{-5}$ Hz. Interestingly, this frequency is even visible by-eye in the pre-eclipse data, shown in Fig. 3.3. There are some minor amplitude peaks at the higher frequencies (the red spots), during the non-eclipsing state before 55 ks. Then during the eclipsing state, these amplitude peaks are non-existent.

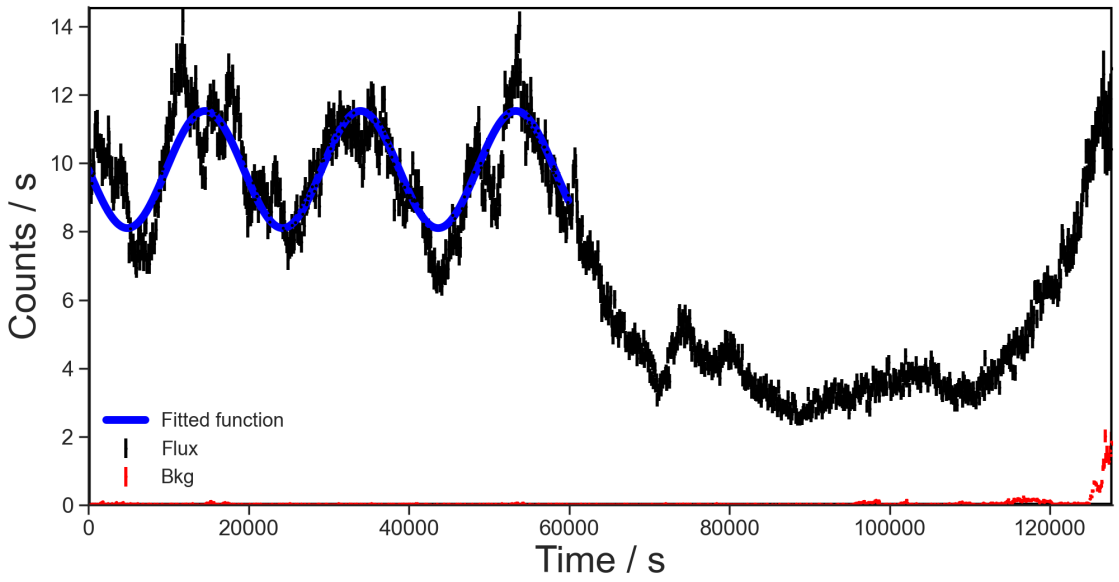

Figure 3.3: *XMM Newton* observation of NGC 6814, revolution 2991 (Obs ID: 0764620101) in the 0.3 - 10 keV band, with a sine wave ploted to the pre-eclipse state. The frequency of the sine wave is 5.16×10^{-5} Hz.

Like in Sec. 2.3.2.2, to determine the significance of such frequencies we compare the observed light curve to an ensemble of 1000 simulated light curves mimicking the observation. The method outlined in Emmanoulopoulos et al. (2013) is used to simulate a light curve with the same PSD and PDF of the observation. The source exhibits a steep PSD with $\beta \approx 2$. The signal at 5×10^{-5} Hz is consistent with noise according to our simulation (Fig. 3.4).

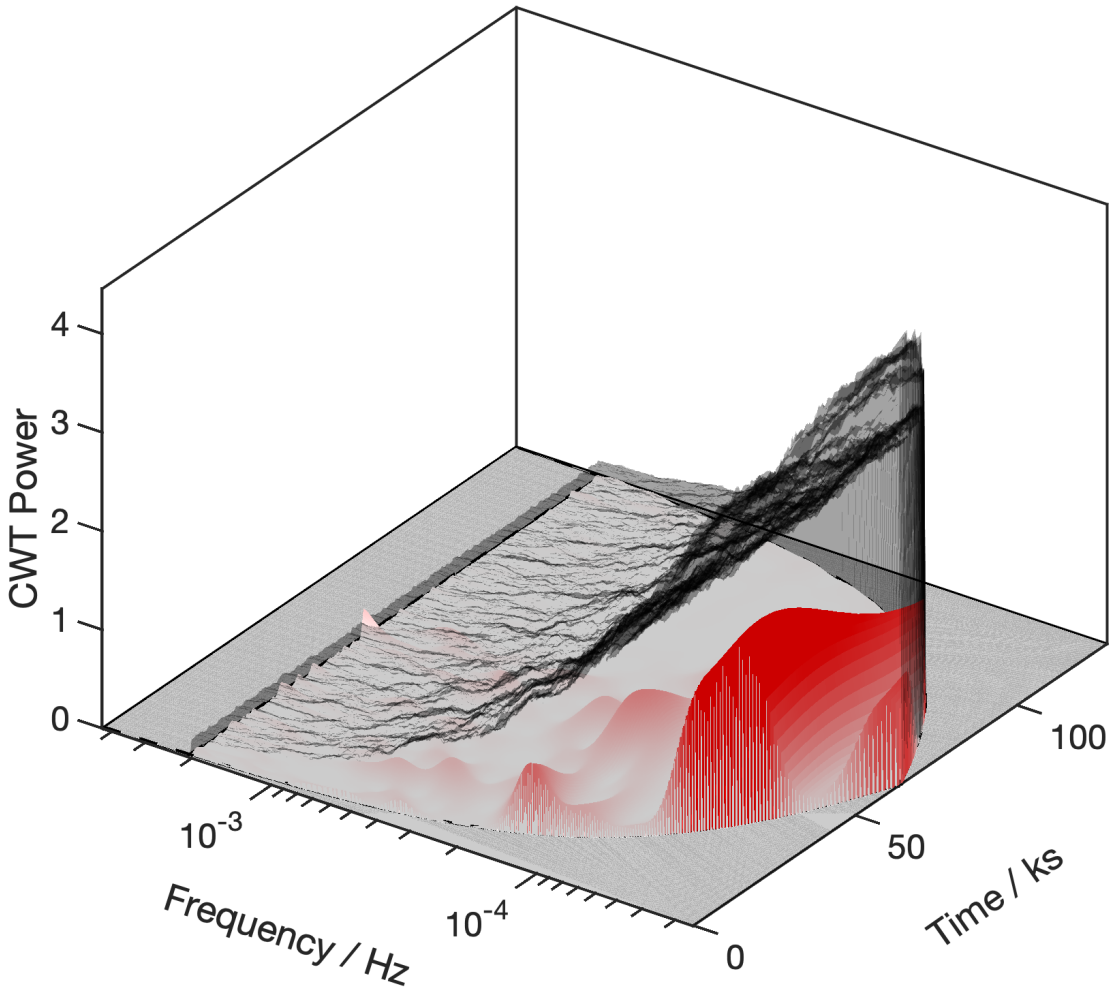

Figure 3.4: The 3-dimensional representation of Fig. 3.2 (2016 observation). The plane of significance is calculated at the 95% significance level.

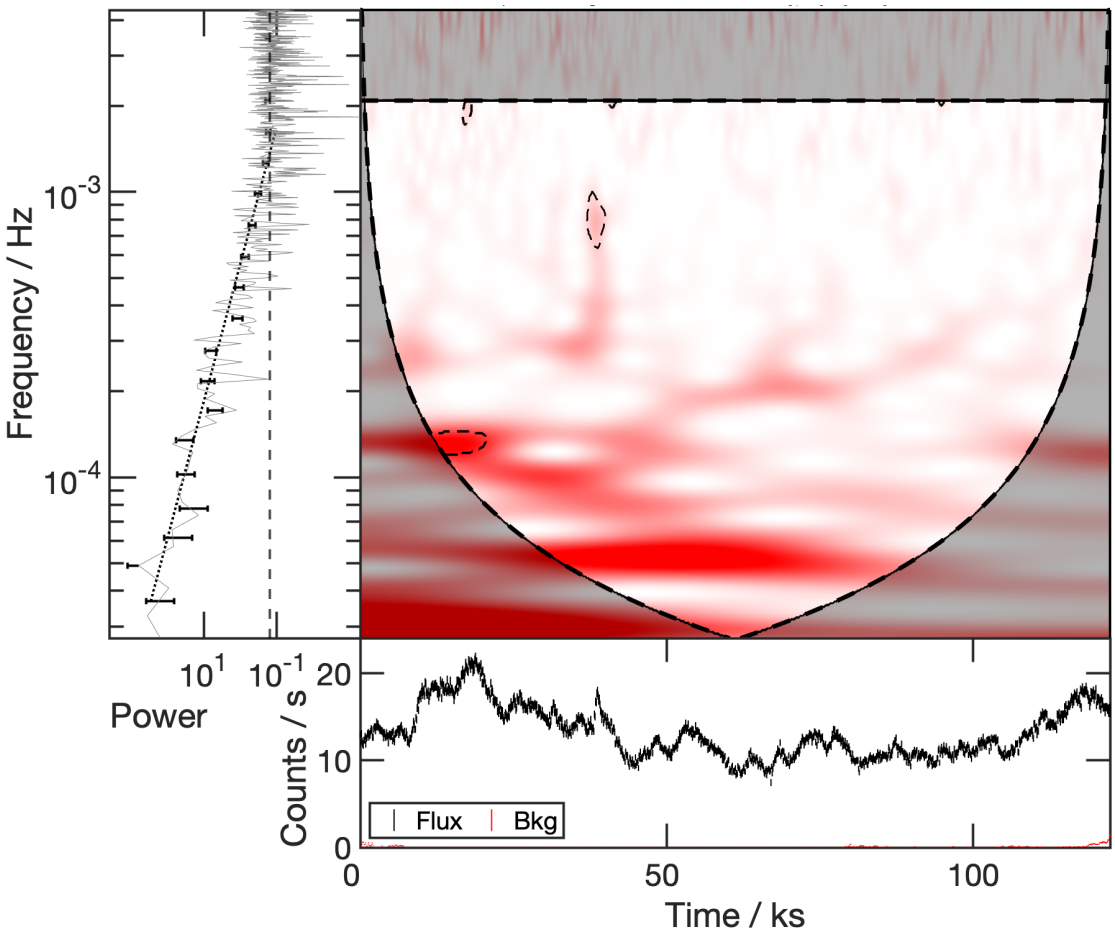

Figure 3.5: The generalized Morse wavelet of NGC 6814, revolution 3995 (Obs ID: 0885090101) in the 0.3 - 10 keV band. There is no eclipse present in this observation.

Similarly, we examined the 2021 *XMM-Newton* observation of NGC 6814, where no eclipse occured. Just as with the 2016 observation, the CWT of the 2021 observation has a visually apparent amplitude peak at $\sim 5 \times 10^{-5}$ Hz. However, it is not significant according to the simulated ensemble of light curves, as it is, once again, consistent with noise. This is also shown in the 3-dimensional representation in Fig. 3.6.

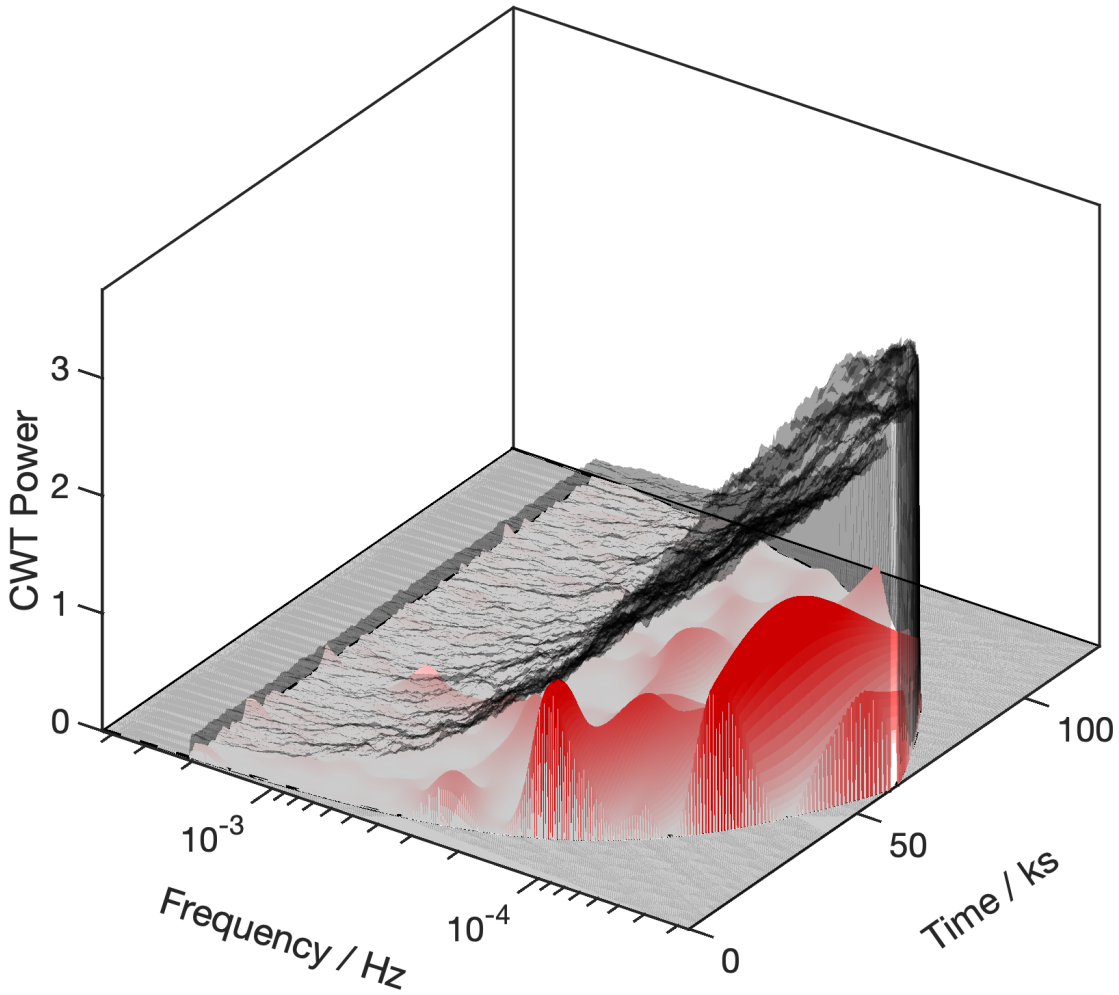

Figure 3.6: The 3-dimensional representation of Fig. 3.5. The plane of significance is calculated at the 95% significance level.

3.3 Discussion and Conclusions

A wavelet analysis of NGC 6814 using data from 2016 and 2021, both reveal an interesting feature at $\sim 5 \times 10^{-5}$ Hz. The period is even noticeable in the light curve by eye during the pre-eclipse state of the 2016 observation. However, the uncertainty analysis indicates that the feature is not significant at either epoch.

Though not significant, the coincidence is interesting. The feature might be similar to the QPO observed in RE J1034+396 (Sec. 2.4.3). The QPO frequency is attributed to an orbital time scale, so the distance from the center of the black hole can be calculated assuming a Keplerian

orbit, using the equation from (Gallo et al. 2018):

$$t_{dyn} = (3.7 \times 10^{-2}) \left(\frac{M}{10^8 M_\odot} \right) \left(\frac{r}{r_g} \right)^{3/2} \text{days} \ . \tag{3.1}$$

Adopting a black hole mass of $1.09 \times 10^7 M_\odot$ (Gallo et al. 2021), this would correspond to emission coming from $14.6 \ r_g$. This is coincident with the size of the corona estimated by Gallo et al. (2021).

It is not clear if the frequency is important and if it is attribute to the eclipse in anyway. Longer observations with *XMM-Newton* can provide long enough light curves to detect the feature more significantly.

Chapter 4

Conclusions

Since AGN X-ray variability is likely non-stationary, it is important to consider using timing analysis tools which reflect this. While the widely used Fourier transforms assume stationarity, the wavelet transform does not make this assumption. Additionally, the wavelet transform provides timing information for the frequency decomposition of a signal, while the Fourier transform returns the frequency distribution over the entire signal. In this work, the wavelet transform was examined and applied to X-ray light curves of various objects to study their timing properties, and to learn more about AGN.

Before applying the wavelet transform to real data, X-ray light curves with various properties were simulated. This was to test the response of the wavelet transform to characteristics that are instrinsic to AGN behaviour and consequences of data treatment. The various properties tested include average count rate, exposure length, PSD slope, the presence of a Lorenztian component in the PSD to mimic a QPO, and more. For the wavelet analysis, the generalized Morse basis wavelet was used, with the time-bandwidth parameter set to 60, and the symmetry parameter set to 3 (most symmetric), for every observation and simulation.

The significance regions were calculated by comparing the wavelet power at each location in the time - frequency space to the distribution of wavelet power spectra from an ensemble of 1000

simulated light curves. Any location where the wavelet power of the observation was greater than the percentile of the desired significance of the ensemble, was deemed to be significant.

Ark 120 showed the least variability in the set of observations, which was expected due to its large black hole mass and low flux variability. The wavelet power spectrum of Ark 120 was consistent with noise. IRAS 13224-3809 was a red noise process with a steep PSD. The only noticeable feature in the wavelet power spectrum was when the count rate flared at ~ 75 ks. This flare did result in a detection of frequencies at the 90% significance level. RE J1034+396 is an AGN which has been reported to exhibit a QPO. This QPO was detected at the 90% confidence level with the wavelet transform. GSN 069 had the most unique light curve in the sample, exhibiting a QPE behaviour where the flux periodically would increase over a near-zero "continuum" level.

In addition to the four previously mentioned sources, we also examined another AGN called NGC 6814. Two observations were studied, one from 2016 and the other from 2021. The 2016 observation exhibited a transient light curve similar to exoplanet systems. The 2021 observation did not contain an eclipse. The wavelet power spectra from both observations revealed an interesting feature at $\sim 5 \times 10^{-5}$ Hz. This periodic feature is visible in the 2016 light curve during the pre-eclipse state. However, this feature was not deemed to be significant in either epoch. Although not significant, it is interesting that this feature occurs in two different data sets. Thus while this detection is not robust, it is marginal. If attributing this frequency to an orbital time scale and assuming a Keplerian orbit, the distance from the central black hole is approximately $15\ r_g$, which is coincident with measurements of the corona extent. Longer observations are necessary to detect this feature with more significance.

Overall, wavelet transforms have shown to be a useful tool for time series analysis, albeit with some caveats. The main advantage of the application of wavelet transforms to AGN X-ray emission, is the lack of any assumption of the stationarity of the time series. Fourier analysis

assumes the time series is stationary, and wavelet transforms do not make this assumption. The literature suggests that AGN X-ray emission is likely non-stationary (see Sec. 1.3 and Sec. 2.1 for more information on the stationarity of AGN X-ray emission). Due to this, wavelet analysis is a useful tool for examining these light curves.

The other key advantage of wavelet transforms is the time localization of each frequency amplitude present within the time series. While the Fourier transform calculates the total frequency distribution over the entire time series, the wavelet transform calculates this frequency distribution as a function of time. This is useful to see how these frequencies change with time. Relating to the difference between stationarity and non-stationarity, a consequence of non-stationarity can be that the frequencies present are not constant in time.

There are however, disadvantages to the wavelet transform. The most basic one is the computational complexity required to calculate a wavelet transform compared to a Fourier transform. This is due to the fact that the wavelet transform algorithms use a series of Fourier transforms to easily calculate the power while “sliding" through the time domain. This is done using the convolution theorem which uses the Fourier transforms of the time series and wavelet basis vector. This difference in computational time is amplified when calculating the significance regions which in this work involved the calculation of 1000 wavelet power spectra, of the simulated versions of the observed time series.

Another apparent drawback, is the choice from many wavelet basis vectors, or “mother wavelets". With each wavelet basis, there are further parameters which can be adjusted, such as the variance and symmetry parameters of generalized Morse wavelet, which was used for this works. However, this is not a major drawback, as the use of Fourier transforms for time series analysis involves the implicit decision to use sine waves as the basis vector.

Generally, interpreting the wavelet power spectrum has an added layer of complexity when compared to the Fourier power spectrum as a result of an added dimension. The wavelet power

spectrum is a 2-dimensional function, as opposed to the Fourier power spectrum being a 1-dimensional function which are more customary in timing analysis.

Also, Fourier transforms have more standardized methods for quantifying uncertainties. This still need to be developed further for wavelet analysis. A method for uncertainties is outlined in Torrence & Compo (1998), but the time series is assumed to be Gaussian distributed, which is typically not the case for X-ray emission. The uncertainties were estimated empirically in our analysis. Finally, it can be a challenge to determine if a signal is intrinsically variable, or if the changes are due to statistical fluctuations, or other effects.

A drawback of the wavelet transform which must be kept in mind for each observation, is the boundary effects. These are quantified by the cone of influence, described in Sec. 1.4.4 and Sec. 2.3.2.1. Due to this, long exposures are vital towards significantly detecting amplitude peaks in the wavelet power spectrum.

In this work, all of the light curves and simulations analyzed were uniformly sampled. Meaning the time spacing between each flux data point were identical. However, this is a very ideal case. The reality is that in astronomy, we are often dealing with non-uniformly sampled data. This is due to various reasons from allocated telescope time to orbital properties for space telescopes. The Fourier transform cannot be applied to data with gaps, but different versions of the wavelet transform can. For example, the weighted wavelet z transform, or WWZ transform (Foster 1996) is made for data with gaps. This analysis can be applied to data from X-ray telescopes such as Swift and Suzaku, which have longer exposure times but the data are non-uniformly sampled. This analysis will be applied to objects such as NGC 6814 to better understand the eclipsing event, and Mrk 335 which has almost 20 years worth of data.

Bibliography

Addison, P. S. 2017, The Illustrated Wavelet Transform Handbook : Introductory theory and applications in science, engineering, medicine and finance (6000 Broken Sound Parkway NW, Suite 300 Boca Raton, FL 33487-2742: CRC Press, Taylor & Francis)

Akansu, A. N., Duhamel, P., Lin, X., & De Courville, M. 1998, IEEE Transactions on signal processing, 46, 979

Alston, W. 2019, Monthly Notices of the Royal Astronomical Society, 485, 260

Alston, W., Fabian, A., Buisson, D., et al. 2019, Monthly Notices of the Royal Astronomical Society, 482, 2088

Alston, W. N., Fabian, A. C., Kara, E., et al. 2020, Nature Astronomy, 4, 597

Anzolin, G., Tamburini, F., De Martino, D., & Bianchini, A. 2010, Astronomy & Astrophysics, 519, A69

Badawy, W., Weeks, M., Zhang, G., Talley, M., & Bayoumi, M. A. 2002, IEEE Engineering in medicine and Biology Magazine, 21, 95

Baig, S., Asif, H. M., Umer, T., et al. 2018, IEEE Access, 6, 52490

Balafas, K., & Kiremidjian, A. S. 2015, Earthquake Engineering & Structural Dynamics, 44, 501

Boller, T., Brandt, W., Fabian, A., & Fink, H. 1997, Monthly Notices of the Royal Astronomical Society, 289, 393

Bostanov, V. 2004, IEEE Transactions on Biomedical engineering, 51, 1057

Bravo, J., Roque, S., Estrela, R., Leão, I., & De Medeiros, J. 2014, Astronomy & Astrophysics, 568, A34

Broughton, S. A. 1998, Rose-Hulman Institute of Technology

Caferra, R., & Vidal-Tomás, D. 2021, Finance Research Letters, 43, 101954

Chang, C.-L., & Girod, B. 2007, IEEE Transactions on Image Processing, 16, 1289

Chen, X., Wang, W., You, B., et al. 2022, Monthly Notices of the Royal Astronomical Society, 513, 4875

Cheng, C., Liu, J., Zhang, C., et al. 2010, Applied Spectroscopy Reviews, 45, 148

Chervyakov, N., Lyakhov, P., & Nagornov, N. 2018, Optoelectronics, Instrumentation and Data Processing, 54, 608

Daubechies, I., Guskov, I., Schröder, P., & Sweldens, W. 1999, Philosophical Transactions of the Royal Society of London. Series A: Mathematical, Physical and Engineering Sciences, 357, 2397

Dewangan, G., Boller, T., Singh, K., & Leighly, K. 2002, Astronomy & Astrophysics, 390, 65

Dominique, M., Zhukov, A., Dolla, L., Inglis, A., & Lapenta, G. 2018, Solar Physics, 293, 1

Emmanoulopoulos, D., McHardy, I., & Papadakis, I. 2013, Monthly Notices of the Royal Astronomical Society, 433, 907

Engstrom, R. W. 1974, JOSA, 64, 1706

ESA. Handbook, XMM-Newton Users Handbook, Issue 2.20, 2022 (ESA: XMM-Newton SOC) (European Space Agency)

Fabian, A., Kara, E., Walton, D., et al. 2013, Monthly Notices of the Royal Astronomical Society, 429, 2917

Fath, E. A. 1909, Publications of the Astronomical Society of the Pacific, 21, 138

Fermi Gamma-Ray Space Telescope, N. 2016, Exploring Active Galactic Nuclei, `https://fermi.gsfc.nasa.gov/science/eteu/agn/`

Foster, G. 1996, Astronomical Journal v. 112, p. 1709-1729, 112, 1709

Frick, P., Baliunas, S., Galyagin, D., Sokoloff, D., & Soon, W. 1997, The Astrophysical Journal, 483, 426

Gallo, L. 2011, Journal of the Royal Astronomical Society of Canada

—. 2018, arXiv preprint arXiv:1807.09838

Gallo, L., Blue, D., Grupe, D., Komossa, S., & Wilkins, D. 2018, Monthly Notices of the Royal Astronomical Society, 478, 2557

Gallo, L., Boller, T., Tanaka, Y., et al. 2004, Monthly Notices of the Royal Astronomical Society, 347, 269

Gallo, L. C., Gonzalez, A. G., & Miller, J. M. 2021, The Astrophysical Journal Letters, 908, L33

Gierliński, M., Middleton, M., Ward, M., & Done, C. 2008, Nature, 455, 369

Gliozzi, M., Papadakis, I., Sambruna, R., & Eracleous, M. 2004a, arXiv preprint astro-ph/0409685

—. 2004b, arXiv preprint astro-ph/0409685

Gonzalez-Martin, O., & Vaughan, S. 2012, Astronomy & Astrophysics, 544, A80

Goodell, J. W., & Goutte, S. 2021, Finance Research Letters, 38, 101625

Gupta, A. C., Srivastava, A., & Wiita, P. J. 2008, The Astrophysical Journal, 690, 216

Gupta, A. C., Tripathi, A., Wiita, P. J., et al. 2018, Astronomy & Astrophysics, 616, L6

Hovatta, T., Lehto, H., & Tornikoski, M. 2008, Astronomy & Astrophysics, 488, 897

Jansen, F., Lumb, D., Altieri, B., et al. 2001, A&A, 365, L1, doi: 10.1051/0004-6361:20000036

Jha, C., & Kolekar, M. 2021, Irbm, 42, 65

Jiang, J., Parker, M., Fabian, A., et al. 2018, Monthly Notices of the Royal Astronomical Society, 477, 3711

Jin, C., Done, C., & Ward, M. 2020, Monthly Notices of the Royal Astronomical Society, 495, 3538

—. 2021, Monthly Notices of the Royal Astronomical Society, 500, 2475

Kara, E., Fabian, A., Cackett, E., Miniutti, G., & Uttley, P. 2013, Monthly Notices of the Royal Astronomical Society, 430, 1408

Karamzadeh, N., Doloei, G. J., & Reza, A. M. 2012, IEEE Transactions on Geoscience and Remote Sensing, 51, 2666

Kolb, U. 2010, Extreme Environment Astrophysics (The Edinburgh Building, Cambridge, CB2 8RU, UK: Cambridge University Press)

Komorowski, D., & Pietraszek, S. 2016, Journal of medical systems, 40, 1

Koratkar, A., & Blaes, O. 1999, Publications of the Astronomical Society of the Pacific, 111, 1

Kretschmar, P. 2018, XMM-Newton Overall Mission Status, `https://www.cosmos.esa.int/documents/332006/1713846/mission_status.pdf`, European Space Agency

Kristoufek, L. 2013, Scientific reports, 3, 2857

Krivova, N., & Solanki, S. 2002, Astronomy & Astrophysics, 394, 701

Leighly, K., Kunieda, H., Tsusaka, Y., Awaki, H., & Tsuruta, S. 1994, The Astrophysical Journal, 421, 69

Levine, E. S., Blitz, L., & Heiles, C. 2006, The Astrophysical Journal, 643, 881

Li, H., Yi, T., Gu, M., & Huo, L. 2009, Progress in Natural Science, 19, 461

Lilly, J. M. 2017, Proceedings of the Royal Society A: Mathematical, Physical and Engineering Sciences, 473, 20160776

Lilly, J. M., & Olhede, S. C. 2008, IEEE Transactions on Signal Processing, 57, 146

Lin, L. C.-C., Hu, C.-P., Kong, A. K., et al. 2015, Monthly Notices of the Royal Astronomical Society, 454, 1644

Lu, W., & Quataert, E. 2022, arXiv preprint arXiv:2210.08023

Lu, Y., & Yu, Q. 2001, Monthly Notices of the Royal Astronomical Society, 324, 653

Markowitz, A., & Edelson, R. 2001, The Astrophysical Journal, 547, 684

Matt, G., Marinucci, A., Guainazzi, M., et al. 2014, Monthly Notices of the Royal Astronomical Society, 439, 3016

McHardy, I. M. 2001, 224, 205

Middleton, M., Done, C., Ward, M., Gierliński, M., & Schurch, N. 2009, Monthly Notices of the Royal Astronomical Society, 394, 250

Miniutti, G., Giustini, M., Arcodia, R., et al. 2023, Astronomy and Astrophysics, 670, A93

Miniutti, G., Saxton, R., Giustini, M., et al. 2019, Nature, 573, 381

Misiti, M., Misiti, Y., Oppenheim, G., Poggi, J.-M., et al. 1996, The Math Works Ins, 2

Morgan. 2002, Distant and Weird Galaxies, https://sites.uni.edu/morgans/astro/course/Notes/section3/new13.html

Mukai, K., Hellier, C., Madejski, G., Patterson, J., & Skillman, D. 2003, The Astrophysical Journal, 597, 479

Mushotzky, R. F., Done, C., & Pounds, K. A. 1993, Annual review of astronomy and astrophysics, 31, 717

Nandi, P., Chatterjee, A., Chakrabarti, S. K., & Dutta, B. G. 2021, Monthly Notices of the Royal Astronomical Society, 506, 3111

Nardini, E., Fabian, A., Reis, R., & Walton, D. 2011, Monthly Notices of the Royal Astronomical Society, 410, 1251

NASA. 2019, How do X-ray telescopes differ from optical telescopes?, https://xrtpub.cfa.harvard.edu/xray_astro/history.html, Chandra X-ray Observatory

Netzer, H. 2013, The Physics and Evolution of Active Galactic Nuclei (32 Avenue of the Americas, New York, NY 10013-2473, USA: Cambridge University Press)

Nobach, H., Tropea, C., Cordier, L., et al. 2007, in Springer Handbooks (Springer), 1337–1398

Oke, J. B., & Sargent, W. L. W. 1968, ApJ, 151, 807, doi: 10.1086/149486

Olayeni, O. R. 2016, Computational Economics, 47, 321

Padovani, P., Alexander, D., Assef, R., et al. 2017, The Astronomy and Astrophysics Review, 25, 1

Pan, X., Li, S.-L., Cao, X., Miniutti, G., & Gu, M. 2022, The Astrophysical Journal Letters, 928, L18

Panagiotou, C., Kara, E., & Dovčiak, M. 2022, The Astrophysical Journal, 941, 57

Paolillo, M., Schreier, E., Giacconi, R., Koekemoer, A., & Grogin, N. 2004, The Astrophysical Journal, 611, 93

Peterson, B. M., Ferrarese, L., Gilbert, K., et al. 2004, The Astrophysical Journal, 613, 682

Press, W., & Rybicki, G. 1997, in Astronomical Time Series (Springer), 61–72

Qu, Y., Adam, B.-l., Thornquist, M., et al. 2003, Biometrics, 59, 143

Remillard, R. A., & McClintock, J. E. 2006, Annu. Rev. Astron. Astrophys., 44, 49

Remillard, R. A., Morgan, E. H., McClintock, J. E., Bailyn, C. D., & Orosz, J. A. 1999, The Astrophysical Journal, 522, 397

Remillard, R. A., Muno, M. P., McClintock, J. E., & Orosz, J. A. 2002, The Astrophysical Journal, 580, 1030

Ren, H. X., Cerruti, M., & Sahakyan, N. 2022, arXiv preprint arXiv:2204.13051

Rosenblatt, E. I., Malkan, M. A., Sargent, W. L., & Readhead, A. 1992, The Astrophysical Journal Supplement Series, 81, 59

Saad, W., El-Fishawy, N., El-Rabaie, S., & Shokair, M. 2010, in Advances in Grid and Pervasive

Computing: 5th International Conference, GPC 2010, Hualien, Taiwan, May 10-13, 2010. Proceedings 5, Springer, 533–541

Seyfert, C. K. 1943, The Astrophysical Journal, 97, 28

Shakura, N. I., & Sunyaev, R. A. 1973, A&A, 24, 337

Strohmayer, T. E. 2001, The Astrophysical Journal, 552, L49

Strüder, L., Briel, U., Dennerl, K., et al. 2001, Astronomy & Astrophysics, 365, L18

Strüder, L., Briel, U., Dennerl, K., et al. 2001, A&A, 365, L18, doi: 10.1051/0004-6361:20000066

Suresh, A., Sharma, R., Oberoi, D., et al. 2017, The Astrophysical Journal, 843, 19

Timmer, J., & Koenig, M. 1995, Astronomy and Astrophysics, 300, 707

Tiwari, A. K., Mutascu, M. I., & Albulescu, C. T. 2016, International Review of Economics & Finance, 42, 237

Torrence, C., & Compo, G. P. 1998, Bulletin of the American Meteorological society, 79, 61

Umar, Z., Gubareva, M., Teplova, T., & Tran, D. K. 2022, Finance Research Letters, 47, 102725

Urry, P. P. 1995, Publications of the Astronomical Society of the Pacific, 107

Uttley, P., Cackett, E., Fabian, A., Kara, E., & Wilkins, D. 2014, The Astronomy and Astrophysics Review, 22, 1

Uttley, P., McHardy, I., & Vaughan, S. 2005, Monthly Notices of the Royal Astronomical Society, 359, 345

Vaughan, S., Edelson, R., Warwick, R., & Uttley, P. 2003, Monthly Notices of the Royal Astronomical Society, 345, 1271

Vaughan, S., Uttley, P., Pounds, K. A., Nandra, K., & Strohmayer, T. 2011a, Monthly Notices of the Royal Astronomical Society, 413, 2489

—. 2011b, Monthly Notices of the Royal Astronomical Society, 413, 2489

Waddell, S. G., & Gallo, L. C. 2020, Monthly Notices of the Royal Astronomical Society, 498, 5207

Walton, D., Zoghbi, A., Cackett, E., et al. 2013, The Astrophysical Journal Letters, 777, L23

Wolfson, M., Hennawi, J. F., Davies, F. B., et al. 2021, Monthly Notices of the Royal Astronomical Society, 508, 5493